

# Modeling Light Curves of Type Ia Supernovae

Dissertation  
zur Erlangung des Doktorgrades  
des Department Physik  
der Universität Hamburg

vorgelegt von  
**Dennis Jack**  
aus Bad Oldesloe

Hamburg  
2009

Gutachter der Dissertation:	Prof. Dr. P. Hauschildt Prof. Dr. E. Baron
Gutachter der Disputation:	Prof. Dr. G. Wiedemann Prof. Dr. J. Schmitt
Datum der Disputation:	13. November 2009
Vorsitzender des Prüfungsausschusses:	Dr. R. Baade
Vorsitzender des Promotionsausschusses:	Prof. Dr. R. Klanner
Dekan der MIN-Fakultät:	Prof. Dr. H. Graener
Leiter des Department Physik:	Prof. Dr. J. Bartels

# Zusammenfassung

Das Hauptanliegen dieser Arbeit ist die Einführung von Zeitabhängigkeiten in PHOENIX. Dieses wurde sowohl für das Strahlungsfeld als auch für die Materie in der SN Ia Modellatmosphäre durchgeführt.

Als erstes wurde die Zeitabhängigkeit in der Strahlungstransportgleichung implementiert. Zwei Diskretisierungsschemata wurden dafür angewendet. Mit Testrechnungen wurde die korrekte Implementation des Zeitderivats überprüft. Die Zeitskala, die mit der neuen Implementation berechnet wurde ist vergleichbar mit der eines einfachen analytischen Ansatzes. Störungen der inneren Randbedingung der Atmosphäre bewegen sich durch die gesamte Modellatmosphäre. Für den Fall einer sinusförmigen Störung im Inneren ergibt sich für die ganze Atmosphäre eine sinusförmig ändernde Leuchtkraft.

Die nächste Erweiterung ist die Zeitabhängigkeit der Materie, für die ein einfacher hydrodynamischer Löser eingebaut wurde. Er berechnet die Energieänderung in einer SN Ia Atmosphäre und betrachtet dabei die homologe Expansion, den Energietransport sowie die zusätzliche Energie, die durch Emission von  $\gamma$ -Strahlung auf Grund des radioaktiven Zerfalls von  $^{56}\text{Ni}$  und  $^{56}\text{Co}$  entsteht. Testrechnungen für jeden einzelnen Teil der Implementation wurden durchgeführt. Der Energiezuwachs führt zur Erwärmung der Atmosphäre und verstärkt die Leuchtkraft, wogegen die adiabatische Expansion die Atmosphäre abkühlt. Der Energietransport verändert die Temperaturstruktur der Atmosphäre in Richtung des Strahlungsgleichgewicht.

Der hydrodynamische Löser wurde zur Berechnung von SN Ia Modelllichtkurven angewendet. Mit der Annahme von LTE in der Atmosphäre wurden Lichtkurven errechnet, die mit den beobachteten von SN 1999ee und SN 2002bo gut übereinstimmen. Einige Abweichungen ergeben sich jedoch für den Nahinfrarot-Bereich. Um die Lichtkurven weiter zu verbessern wurden Berechnungen mit unterschiedlicher Energieeinspeisung durchgeführt. Mit mehr Energieeinspeisung werden die Lichtkurven zu jeder Zeit heller, bei weniger Energieeinspeisung entsprechend dunkler. Eine Verbesserung der Nahinfrarot-Lichtkurven wurde jedoch nicht erreicht. Drei verschiedene Explosionsmodelle wurden für die SN Ia Lichtkurvenberechnungen benutzt. Das Modell der verzögerten Detonation DD 16 kann als richtiges Explosionsmodell ausgeschlossen werden. Die Lichtkurven sind zu dunkel um die beobachteten Lichtkurven zu reproduzieren. Die am besten passende Lichtkurve wurde mit dem W7 Deflagrationsmodell erzielt. Das Modell DD 25 erzielt auch gut passende Lichtkurven.

Es wurde gezeigt, dass Streuung wichtig für die Behandlung des Strahlungstransports bei der Berechnung von Modelllichtkurven von SNe Ia ist. Deshalb wurden komplexere NLTE Modelllichtkurven berechnet. Zuerst wurde dafür die Temperaturstruktur der LTE Berechnungen benutzt. Mit der Annahme von NLTE erhält man Änderungen in den Lichtkurven. Dabei wurden erhebliche Verbesserungen in der Lichtkurve im I Band erzielt. Weitere Modelle wurden berechnet, bei denen sich die Temperaturstruktur den NLTE Bedingungen anpassen könnten. Dies erhöht die Berechnungszeit gewaltig. Es wurden jedoch kaum Verbesserungen im Vergleich zu den Modellen mit LTE Temperaturstruktur erzielt.



# Abstract

The main topic of this work is the introduction of time dependence into PHOENIX. This has been achieved for both the radiation field and the matter in the SN Ia model atmosphere.

First, time dependence in the radiative transfer equation has been implemented. Two discretization schemes have been used for the implementation of the time derivative. Test calculations have been performed to confirm the correctness of the implementations. The radiation time scale computed with the time dependent radiative transfer is comparable to a simple analytic approach. Perturbations of the inner boundary condition of the atmosphere move through the whole atmosphere. For instance, an atmosphere with a sinusoidally varying inner light bulb leads to an atmosphere where the luminosity varies sinusoidally everywhere.

For the next extension of time dependence for the matter, a simple hydrodynamical solver has been implemented. It computes the changes in the energy of an SN Ia atmosphere by considering the homologous expansion, energy transport and the deposition of energy by  $\gamma$ -ray emission due to the radioactive decay of  $^{56}\text{Ni}$  and  $^{56}\text{Co}$ . Test calculations verified that each part of the solver works correctly. The energy deposition heats the atmosphere and increases the observed luminosity, whereas the adiabatic expansion cools the atmosphere. The energy transport always pushes the temperature structure of the atmosphere towards the radiative equilibrium state.

The hydrodynamical solver has been applied to calculate SN Ia model light curves. With the assumption of an LTE atmosphere, the model light curves are already in good agreement with the observed light curves of SN 1999ee and SN 2002bo. Some deviations between model and observed light curves occur in the near-infrared. In order to improve the model light curves, a calculation with different energy input has been performed. If more energy is deposited into the atmosphere the model light curves in all bands become brighter. With less energy input, fainter model light curves are the result. However, this did not improve the model light curves in the near-infrared. Three different explosion models have been used to compute model light curves of SNe Ia. The delayed detonation model DD 16 can be eliminated as the correct explosion model as it is too faint to reproduce the observed light curves. The best fits to the observed light curves have been achieved with the W7 deflagration model, while the DD 25 model also delivers reasonable model light curves.

It has been shown that scattering in the treatment of radiative transfer is important for the calculation of SN Ia model light curves. Thus, more sophisticated NLTE model light curves have been calculated. At first, the LTE temperature structures have been used. The assumption of NLTE changes the model light curves in some bands. Significant improvement for the I band model light curve has been achieved. Further model light curves where the temperature structure can adapt to the NLTE conditions have been computed. This increased the computation time dramatically. But no significant improvements compared to the NLTE light curves with fixed LTE temperature structure have been found.



# Contents

<b>1</b>	<b>Introduction</b>	<b>1</b>
1.1	Motivation . . . . .	1
1.2	Topic of this work . . . . .	2
1.3	Chapter overview . . . . .	2
<b>2</b>	<b>Supernovae</b>	<b>5</b>
2.1	Classification . . . . .	5
2.2	Progenitor . . . . .	6
2.3	Explosion . . . . .	8
2.4	Spectral evolution . . . . .	10
2.5	SN Ia in cosmology . . . . .	13
2.5.1	Light curves . . . . .	13
2.5.2	Dark energy . . . . .	15
<b>3</b>	<b>Modeling atmospheres with PHOENIX</b>	<b>17</b>
3.1	Radiative transfer . . . . .	17
3.1.1	Radiation field . . . . .	17
3.1.2	Source function . . . . .	18
3.1.3	Radiative transfer equation . . . . .	19
3.1.4	$\Lambda$ -operator and OS method . . . . .	21
3.1.5	Line transitions . . . . .	21
3.1.6	Continuum transitions . . . . .	23
3.1.7	Scattering . . . . .	23
3.2	Modeling atmospheres with PHOENIX . . . . .	24
3.2.1	LTE . . . . .	24
3.2.2	NLTE . . . . .	26
3.2.3	Temperature correction . . . . .	26
3.2.4	Iteration scheme . . . . .	27
<b>4</b>	<b>Time dependent radiative transfer</b>	<b>29</b>
4.1	Time dependent radiative transfer . . . . .	29
4.1.1	First discretization of the time derivative . . . . .	30
4.1.2	Second discretization of the time derivative . . . . .	31
4.1.3	Implementation . . . . .	33
4.2	Test Calculations . . . . .	33
<b>5</b>	<b>Hydrodynamical solver</b>	<b>39</b>
5.1	Hydrodynamical solver . . . . .	39

5.1.1	Dynamical models . . . . .	40
5.1.2	Gamma ray deposition . . . . .	40
5.1.3	Absorption and emission . . . . .	43
5.1.4	Expansion . . . . .	44
5.1.5	Overall energy change . . . . .	45
5.1.6	Adaptive time step procedure . . . . .	47
5.1.7	Iteration scheme . . . . .	48
5.1.8	First approach . . . . .	48
5.2	Test calculations . . . . .	48
5.2.1	Energy transport . . . . .	49
5.2.2	Expansion . . . . .	53
5.2.3	Energy deposition . . . . .	54
5.2.4	Realistic test scenario . . . . .	55
5.3	Conclusions . . . . .	56
<b>6</b>	<b>Modeling SN Ia light curves</b>	<b>57</b>
6.1	Observed SN Ia light curves . . . . .	57
6.2	Model light curves of SNe Ia . . . . .	57
6.2.1	Method . . . . .	58
6.3	Light curves of LTE models . . . . .	59
6.3.1	UBVRI light curves . . . . .	60
6.3.2	Dynamical models . . . . .	62
6.3.3	Influence of the energy deposition model . . . . .	66
6.3.4	Near-infrared light curves . . . . .	67
6.3.5	Simple line scattering . . . . .	70
6.4	Light curves of NLTE models . . . . .	73
6.4.1	NLTE light curves with LTE atmosphere structure . . . . .	73
6.4.2	NLTE atmosphere structures . . . . .	77
6.5	Spectral evolution . . . . .	80
6.5.1	LTE spectral evolution . . . . .	80
6.5.2	NLTE spectral evolution . . . . .	80
6.6	Conclusions . . . . .	82
<b>7</b>	<b>Conclusions and outlook</b>	<b>83</b>
<b>A</b>	<b>Alternative hydrodynamical solver</b>	<b>87</b>
A.1	Test calculations . . . . .	89
	<b>Bibliography</b>	<b>92</b>

# Chapter 1

## Introduction

### 1.1 Motivation

This work was funded by the Deutsche Forschungsgemeinschaft (DFG) via the Collaborative Research Center 676 (Sonderforschungsbereich 676), with the title “Particles, Strings and the Early Universe - the Structure of Matter and Space-Time”. This project contains subprojects in the fields of particle physics, string theory and cosmology. One goal of the SFB project among others is to investigate the cosmology of our universe. Today, about 96% of the content of the universe is not understood. Only 4% of the universe consists of the baryonic matter, which is the matter that can be directly observed because it interacts with electromagnetic radiation. About 23% of the universe is believed to consist of dark matter. The effects of dark matter have been observed in galaxy clusters and in rotation curves of spiral galaxies. Further evidence for the existence of dark matter have been found by gravitational lensing and the measurement of anisotropies in the cosmic microwave background. Various candidates for the dark matter have been proposed. This includes new particles beyond the standard model as for instance supersymmetric particles.

The main content of the universe is the dark energy, which is about 73% of the overall energy. This phenomenon has been discovered first by distance measurements obtained with observations of light curves of type Ia supernovae. Observations at high redshift showed a deviation from the assumed deceleration of the universes expansion. This accelerated expansion of universe has been discovered independently by Riess et al. (1998) and Perlmutter et al. (1999). Other confirmations of the existence of dark energy have been achieved. These are the precise measurements of the microwave background fluctuation by the WMAP mission (Spergel et al. 2003). The existence of dark energy was also confirmed by X-ray observations of galaxy clusters (Allen et al. 2004, 2008) and the baryon acoustic oscillation (Percival et al. 2007).

The role of SNe Ia in cosmology is important. One can use type Ia supernovae to determine cosmological parameters. Further improvements of the measurements of the expansion of the universe are urgently needed. This also includes a better understanding of the physics going on in an SN Ia event. Although the observed SN Ia light curves have been used to measure distances, it is not understood what the correct progenitor or explosion mechanism of an SN Ia event is. The frequently used Phillips relation (Phillips 1993), which has been used to correct SNe Ia light curves to adapt them to standard candles, is a purely empirical observational relation. Therefore, it is vital to understand what is going on in an SN Ia explosion and during the following free expansion phase.

## 1.2 Topic of this work

With PHOENIX a lot of work on type Ia supernovae has been performed (Nugent et al. 1995; Hauschildt et al. 1996; Nugent et al. 1997; Lentz et al. 1999b,a, 2000, 2001b,a, 2002; Baron et al. 2003; Bongard et al. 2006; Baron et al. 2006). For instance, detailed studies of spectra around the maximum phase of the optical light curves have been performed. This also includes studies where the SN Ia atmosphere is assumed to be in NLTE. Dynamical models have been used, where model spectra with the atmosphere structure of different explosion model calculations have been computed. The results of different explosion models can be used to compare them to observed spectra to determine the correct explosion model of an SN Ia event.

So far, all investigations with PHOENIX have been performed under the assumption of time independence for both the radiative transfer and the material in the model atmosphere. Model spectra have been obtained under the assumption of a stationary atmosphere structure, which is in radiative equilibrium. In this work, the aim is to introduce time dependence into PHOENIX for both the radiative transfer and the material in the atmosphere.

First the spherical symmetric special relativistic radiative transfer equation will be solved including time dependence. Details of the implementation will be given as two different discretization methods will be used. Test calculations, which confirm that the implementation is working correctly will be presented.

The other major step is the consideration of a time dependent atmosphere structure. In this work I will consider this for the case of a type Ia supernova atmosphere. The main goal is to calculate model light curves of SNe Ia. In order to achieve this, a simple hydrodynamical solver will be implemented into PHOENIX. This hydrodynamical solver will keep track of the evolution of the properties of a SN Ia atmosphere and the influences on it. The homologous expansion, the energy input by  $\gamma$ -ray emission due to radioactive decay of  $^{56}\text{Ni}$  and  $^{56}\text{Co}$  and the energy transport will be implemented in this hydrodynamical solver. Using this hydrodynamical solver, it is then possible to calculate the whole evolution of an SN Ia model atmosphere during the free expansion phase. Model light curves of SNe Ia will be calculated to learn more about them. For instance, investigations to find the correct explosion model will be performed. The influences of different parameters of the hydrodynamical solver will be tested. A first goal is the computation of light curves, where the atmosphere is considered to be in local thermal equilibrium (LTE). The calculated model light curves will be compared to observed light curves of SN 1999ee and SN 2002bo in different photometric bands. A few model light curves will be computed, where the atmosphere is not in LTE. Further, a short outlook on the spectral evolution will be presented.

## 1.3 Chapter overview

Chapter 2 gives an overview about the phenomenon supernova. The focus is on type Ia supernovae. The current status of the search for a progenitor, correct explosion model and the general properties are discussed. The use of SN Ia light curve observations for the distance measurements and determination of cosmological parameters is presented. Chapter 3 is describing the physics of modeling atmospheres with PHOENIX including its approach to

the radiative transfer problem. The following chapter 4 covers the time dependent radiative transfer. The implementation of the time dependence derivative is discussed. Test calculations are presented that confirm the correct operation of the new implementations. In chapter 5, a simple hydrodynamical solver is presented. This approach has been implemented into PHOENIX. Applying the hydrodynamical solver the evolution of an SN Ia atmosphere can be calculated. With a few test calculations, the new hydrodynamical solver is checked for its proper operation. This implemented code is then applied to calculate model light curves of SNe Ia. The results of the model light curve calculations are presented in chapter 6. First, LTE light curves of different photometric bands have been computed. The influence of the energy deposition is checked. Different hydrodynamical explosion models will be used to determine the correct explosion model. Here, the deflagration model and two delayed detonation models will be tested. To obtain more accurate model light curves, NLTE calculations have also been performed. This work closes with a summary and outlook in chapter 7. In the appendix A, a first unsuccessful approach of a hydrodynamical solver to compute SNe Ia model light curves is presented in more detail.



# Chapter 2

## Supernovae

Throughout history, astronomers observed the appearances of new stars. These *stella nova* were luminous events visible to the naked eye. For instance, Chinese astronomers observed a *stella nova* in the year 1054. The remnant of this event is still visible today and is now called the crab nebula. Actually, this observed “supernova” was not the birth of a new star but rather the death of a massive old star.

This chapter gives an overview about the properties of supernovae with focus on the sub-type Ia. The current status of the search for the progenitors is presented. The different possible explosion models of the SN Ia will be discussed. Observational results such as spectra and light curves are discussed as well. The important use of SN Ia events for measuring of cosmological parameters is presented in more detail.

### 2.1 Classification

A *stella nova* was defined as an event, where a new star seems to appear in the sky. A few of these events were considerably brighter than the others. A distinction was made, and the new class “supernova” (SN) was defined (Zwicky 1938, 1940). Later, a diversity in the spectra of supernova observations was found and new subclasses were introduced. The classification of supernovae presented here is hinged on features in the spectrum and the shape of the SN light curves, see Filippenko (1997) for a detailed overview on the classification and the typical optical spectra of the different SN types and subtypes. The classification of SNe arose purely from observations.

Supernovae events are divided into two main classes. These are the types I and II, which were initially introduced by Minkowski (1941). Supernovae of the type I have no hydrogen features in their observed spectra. Therefore, one can identify a type II supernova by hydrogen features in the spectrum. There is a further diversity in the observed spectra and light curves, so that both types are divided into subtypes. One subtype of the type I is the type Ia, which is defined by the broad Si II absorption trough around 6150 Å in the optical spectrum during the maximum phase of the optical light curve. In the optical spectrum of an SN Ia, no helium features are observed. However, the type Ib has moderately strong optical He features in its spectrum, for instance, at around 5800 Å. Silicon features are not observed in type Ib spectra. The spectrum of a SN Ic shows neither these helium features nor the silicon absorption trough. In figure 2.1, this classification by the spectral features is illustrated.

The spectra of type II supernovae are dominated by the strong H $\alpha$  emission line. The subtypes of the SNe II can be distinguished by the shape of their light curves (Barbon et al.

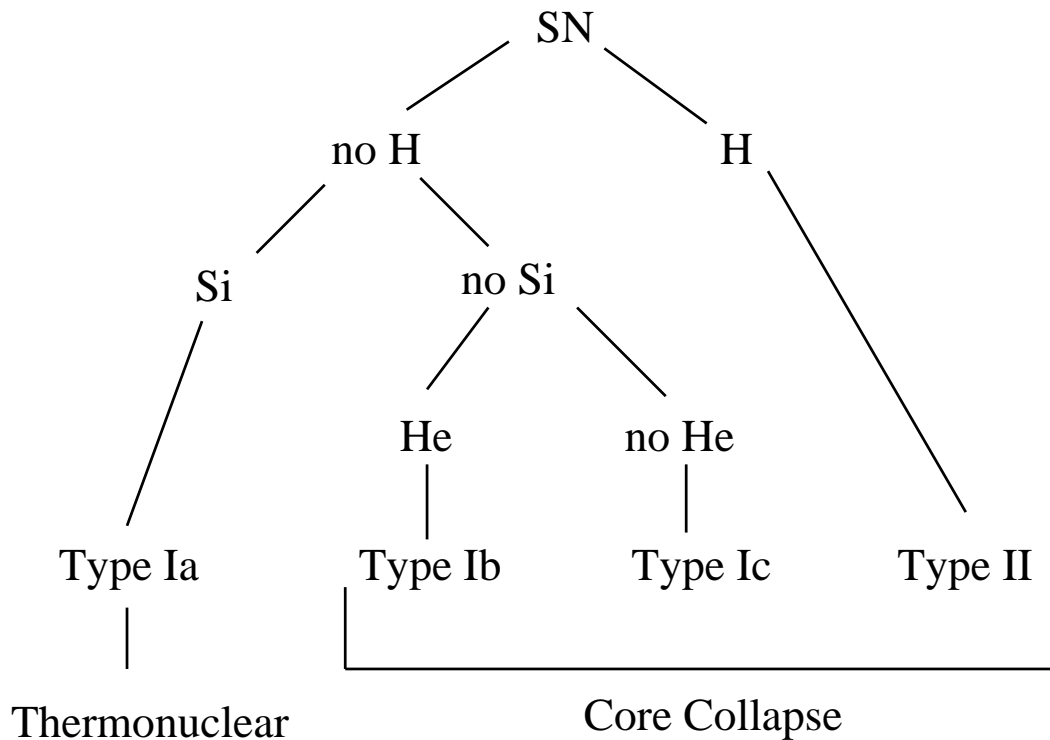


Figure 2.1: The different subtypes of SN events can be distinguished by the presence or absence of spectral features. A SN of the type II has H features, which are not observed in the spectra of supernova of the type I. The subtypes of SN I are divided by the presence of Si or He features.

1979; Doggett & Branch 1985). The light curve of the SN II-P has a plateau after the maximum, while the subtype SN II-L has a linear decline after the maximum. However, there is a discussion going on about other possible classification schemes (Patat et al. 1994).

Although supernovae are defined as one broad class of objects, there is completely different physics going on in the different types or even subtypes. For instance, the type II supernovae event is the death of a massive star. An evolved massive main sequence star that has started silicon burning in its last stage produces an iron core. When this iron core exceeds the Chandrasekhar mass, it collapses, and the star ends in an SN II explosion. The type II supernovae as well as the subtypes Ib and Ic are caused by such a core collapse. However, the type Ia is caused by a thermonuclear explosion. Supernovae of the type Ia are the topic of this work. Therefore, the following discussions about progenitors, explosion models and spectral properties are confined to the type Ia.

## 2.2 Progenitor

An SN Ia explosion is a very luminous event, which releases an enormous amount of energy. The explosion itself releases about  $10^{51}$  erg (Khokhlov et al. 1993). The interesting question is what causes these very bright events. Some progress has been made in the search for the progenitor, but the exact progenitor of a type Ia supernova explosion is still unknown.

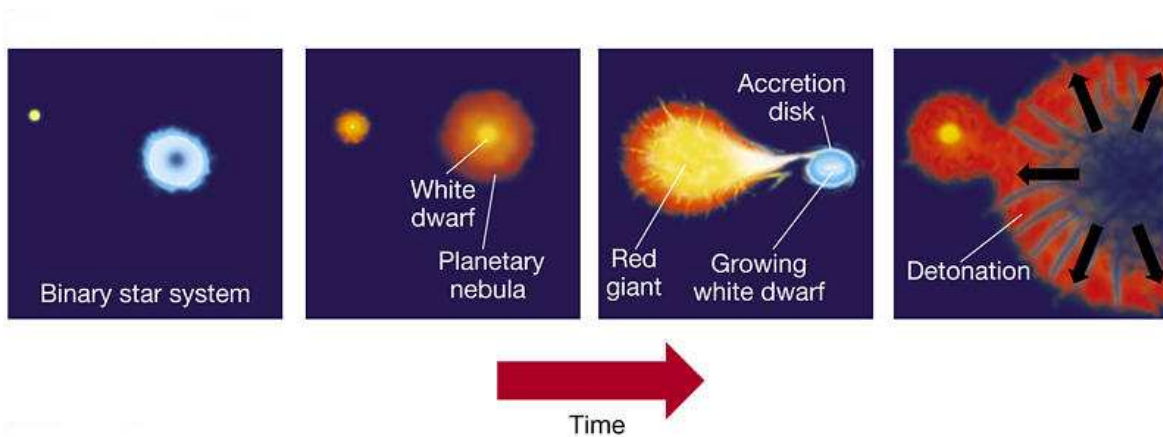


Figure 2.2: The evolution path of a binary star system towards an SN Ia explosion (Brau 2009). The binary system consists of a white dwarf that accretes matter from a companion star. The white dwarf increases its mass and finally disrupts in an SN Ia explosion.

Overviews about the progenitor search and possible candidates can be found in Livio (2000) or Branch et al. (1995).

From observations one can narrow down the candidates for a supernova Ia progenitor. One remarkable property is the homogeneity in the light curves, spectra and peak absolute luminosities among the SN Ia observations. This leads to the conclusion that the conditions at the point of the explosion have to be quite similar in each SN Ia progenitor. Observations reveal more about the progenitor. As the spectra show no features of hydrogen or helium, the progenitor has to consist of other elements. The near maximum optical light observed spectra show features with high velocities (8.000 – 30.000 km/s) of intermediate mass elements, such as Si and Ca. The later spectra show features of iron group elements such as Fe, Co and Ni. Another observational result is that the SN Ia events are not correlated with the type of their host galaxy. So in conclusion, the progenitor cannot be a massive star like the progenitor of a SN II event. SN II are mostly observed in early type galaxies and H II regions.

The widely accepted idea is that the progenitor of a SN Ia is a white dwarf (WD), which disrupts in a thermonuclear explosion. As there are no helium features found in the spectrum, the white dwarf cannot be a He WD. Calculations also show that an exploding He WD would produce just Ni and its decay products and fails to produce the intermediate mass elements, which one can observe in the spectrum (Nomoto & Sugimoto 1977; Woosley et al. 1986). An O-Mg-Ne WD could be the progenitor, but they are not numerous enough (Livio & Truran 1992). A further indication suggesting they are not the progenitor of a SN Ia is shown by evolution calculations, which show that O-Mg-Ne white dwarfs probably will not explode but, instead, form neutron stars (Gutierrez et al. 1996). The last known type of WD, which could be an SN Ia progenitor candidate, is a C-O WD that consists of carbon and oxygen. They are numerous enough to produce SN Ia explosions models. So it is very probable that the progenitor of a type Ia supernova is a C-O WD.

A single star alone cannot be the progenitor of a type Ia supernova. The progenitor has to accrete matter to reach a stadium where it becomes unstable and eventually explodes. If

the WD would be alone, it would just cool down. Another point is that there is no evolution path known, where a single star leads to a SN Ia explosion. So the SN Ia progenitor is believed to be a C-O WD in a binary star system. There currently exist two scenarios for the binary system. In the single degenerate (SD) scenario, a white dwarf has a main sequence star or giant as a companion in a close orbit. This scenario is illustrated in figure 2.2. The white dwarf accretes matter from the companion star. Binary evolution calculations show that these objects can be candidates for a SN Ia progenitor (see Han & Podsiadlowski (2004) and Han & Podsiadlowski (2006)). This single degenerated scenario is also the progenitor of a classical nova (Bode & Evans 1989; Shara 1989). But the classical nova event is a thermonuclear outbreak on the top of the WD, where the accreted hydrogen is burned (Kraft 1964).

In the double degenerated (DD) scenario, the binary system consists of two white dwarfs. The total mass exceeds the Chandrasekhar mass, and they also have a close orbit. Finally, due to gravitational radiation, the two WDs start to merge. Binary star evolution calculations have shown that this scenario is a possible candidate for an SN Ia event (Iben & Tutukov 1984). In this scenario, the absence of H and He features in the spectrum can also be explained. Many double WD systems with close orbits have been found (Saffer et al. 1998). But is not certain, whether these scenario really leads to a supernova Ia explosion. Another possibility is that the WD cools down and forms a neutron star because of accretion-induced collapse (Segretain et al. 1997).

A lot of effort has been put in the search for the progenitor. One could learn more about the progenitor from early observations of SN Ia spectra. The detection of hydrogen in an early spectrum would give a clue about the actual progenitor. In the DD scenario with two C-O WD, there cannot be hydrogen features in the spectrum. So the detection of hydrogen would lead to the SD scenario. In fact, hydrogen has been detected in early spectra of SN 2002ic (Hamuy et al. 2003). The authors point out that this leads to the conclusion that the progenitor is a SD system, where a AGB star is orbiting the WD. On the other hand, Livio & Riess (2003) claim that this detection could also lead to the conclusion that the progenitor is a DD system.

## 2.3 Explosion

Not only is the progenitor still unknown, but there is also a discussion going on about how the actual explosion takes place once the progenitor has reached the conditions for ignition. An overview about the possible explosion mechanisms can be found in Hillebrandt & Niemeyer (2000). Widely accepted is that a thermonuclear explosion takes place in an SN Ia event. The thermonuclear explosion as the explosion mechanism was originally proposed by Hoyle & Fowler (1960). A thermonuclear explosion can explain why SN Ia can be found in all types of galaxies, and the thermonuclear explosion also produces enough  $^{56}\text{Ni}$ , which is consistent with observations.

Only little is known about the way of the white dwarf towards explosion. The evolution towards the ignition of the thermonuclear burning of carbon and oxygen is a complex physical process. The white dwarf is under the influence of the accretion process from the companion star, and the thermal structure of the white dwarf on the way to explosion de-

depends also on the URCA process (Paczynski 1973; Iben 1978, 1982; Barkat & Wheeler 1990; Mochkovitch 1996). This all makes it difficult to perform realistic hydrodynamical evolution simulations. Therefore, the ignition is a free initial parameter in current explosion model calculations. There is also a discussion, whether the flame ignition happens at just one single point (Höflich & Stein 2002) or if there is a multi-spot ignition near the center (Garcia-Senz & Woosley 1995; Woosley et al. 2004; Wunsch & Woosley 2004; Röpke et al. 2006). It turned out that the choice of the initial flame condition leads to different results in the explosion modeling.

There are different ways of how the explosion front moves through the envelope. The detonation is one possible explosion model. The flame front propagates with a velocity higher than the local speed of sound outwards. In this instant detonation, almost all carbon and oxygen is burned to iron-peak elements (Arnett 1969; Arnett et al. 1971). Because of the fact that the flame in the detonation model is moving fast through the WD, it has no time to expand. In a detonation, a huge amount of nickel is produced, but the detonation fails to produce intermediate mass elements like Si, Ca and Mg, which are observed in SN Ia spectra. Hence, the instant detonation alone cannot be the correct explosion model.

Another possible explosion model is the deflagration (Nomoto et al. 1976). The flame ignites at the center and propagates outwards with a velocity lower than the local speed of sound. Numerous 1-D calculations have been performed with this approach to the explosion mechanism (Buchler & Mazurek 1975; Nomoto et al. 1984; Iwamoto et al. 1999; Niemeyer & Woosley 1997). They all agree that the flame speed is  $\approx 30\%$  of the local sound speed. The main difference to the detonation is that in the deflagration case, the WD has time to expand. Therefore, more intermediate mass elements are produced. One model that is in good agreement with the observations is the W7 model of Nomoto et al. (1984). The results of this explosion model have been used to calculate spectra of SN Ia events. Recently, multidimensional modeling of the deflagration model has been performed (Arnett & Livne 1994a; Khokhlov 1995; Niemeyer & Hillebrandt 1995; Reinecke et al. 1999). In some of them the flame front did not reach the necessary velocity to disrupt the star. But this all may be due to problems with the numerical resolution of the models, which is a common problem in multidimensional hydrodynamical calculations.

Another explosion model was presented by Khokhlov (1991a). The delayed detonation model combines the advantages of the detonation and deflagration model (Woosley & Weaver 1994). In the explosion, the flame front starts with a deflagration, which then transits into a detonation. This deflagration to detonation transition (DDT) means that the velocity of the flame is in the beginning lower than the local sound speed. Starting with a slow velocity of  $\approx 1\%$  of the local sound speed, the transition to the detonation occurs at a density of  $\rho \approx 10^7 \text{gcm}^{-3}$  as an estimate of Niemeyer & Kerstein (1997) has shown. The flame then propagates with a higher velocity than the local speed of sound. The advantage is that only a low velocity is needed in the beginning, giving the WD time to expand. The later detonation produces the needed intermediate mass elements before the flame ceases. Numerous of 1-D simulations have shown that this model is a good assumption for the explosion mechanism. Good fits to SN Ia spectra and light curves have been achieved (Höflich & Khokhlov 1996). The calculated nucleosynthesis is also in good agreement with the observations (Khokhlov 1991b; Iwamoto et al. 1999).

A variation of the delayed detonation model is the pulsational delayed detonation model

(Nomoto et al. 1976; Khokhlov 1991b). The explosion starts with a first turbulent deflagration, but the flame eventually dies. Therefore, the released energy is not enough to unbind the star. The star then pulses and triggers a detonation upon recollapse. Studies of this explosion model have been performed (Hoeflich & Khokhlov 1996; Arnett & Livne 1994b). The result is that this explosion mechanism could be a possible explanation for subluminous SN Ia events, because it fails to produce enough amount of  $^{56}\text{Ni}$ . Khokhlov et al. (1997) point out that it is more plausible to obtain a DDT after one or several pulses than during the first expansion phase. The first pulse can preheat the fuel, and turbulence is significantly enhanced during the collapse.

A recently proposed explosion model is the gravitationally confined detonation (GCD) (Plewa et al. 2004; Plewa 2007; Townsley et al. 2007; Meakin et al. 2009). This concept has been developed with 2D hydrodynamical explosion calculations. The general idea is that the explosion starts with an ignition at the center of the white dwarf. The deflagration then moves outwards in form of a hot bubble, which eventually reaches the surface of the white dwarf. At the surface, the material is gravitationally confined and, therefore, flows around the white dwarf towards the opposite pole. Here, the colliding flows initiate a detonation, which disrupts the white dwarf. The GCD can, therefore, be considered as a delayed detonation model that has a special way of undergoing the deflagration to detonation transition. The white dwarf is preexpanding because of the first deflagration phase, which is essential for the production of intermediate mass elements, which are observed in SN Ia spectra.

The actual explosion lasts only a few seconds. After the explosion is over, the ejected material is just freely expanding. This would only lead to adiabatically cooling of the atmosphere. But on the contrary, the observed light curves show a rise after the explosion is long over. The reason for that is the production of a huge amount of radioactive elements. The radioactive decay of nickel and cobalt powers the light curve of an SN Ia (Truran et al. 1967; Colgate & McKee 1969). In the inner part of the atmosphere, about a solar mass of  $^{56}\text{Ni}$  is produced during the explosion.  $^{56}\text{Ni}$  is unstable and decays with an half life of 6.077 days to  $^{56}\text{Co}$ . The  $^{56}\text{Co}$  then decays to  $^{56}\text{Fe}$  with an half life of 77.27 days. The isotope  $^{56}\text{Fe}$  is stable. The decaying isotopes release a vast amount of energy. This energy is emitted as gamma ray emission during the decay. This gamma ray emission is absorbed by the matter in the ejecta, which leads to the heating of the atmosphere and the increasing luminosity.

## 2.4 Spectral evolution

During the evolution of a supernova Ia event the spectrum changes (Filippenko 1997). Early time spectra, observed only a few days after the explosion, show broad spectral features. These are features of neutral or singly ionized intermediate mass elements such as O, Mg, Si, S and Ca. Later, features of Fe, Co and Ni emerge.

In figure 2.3, a typical optical spectrum of an SN Ia near the maximum of the optical light curve is shown. The strongest features are the Si II feature at 6355 Å and the Ca II H&K feature at 3934 Å and 3968 Å. In the near infrared emerges another feature of Ca II at a wavelength of around 9000 Å. More features of intermediate mass elements are observed for Mg II and S II. There are also features of iron group elements such as Fe II and Co II. Throughout the evolution of the spectrum, the contribution of iron elements to the spectrum

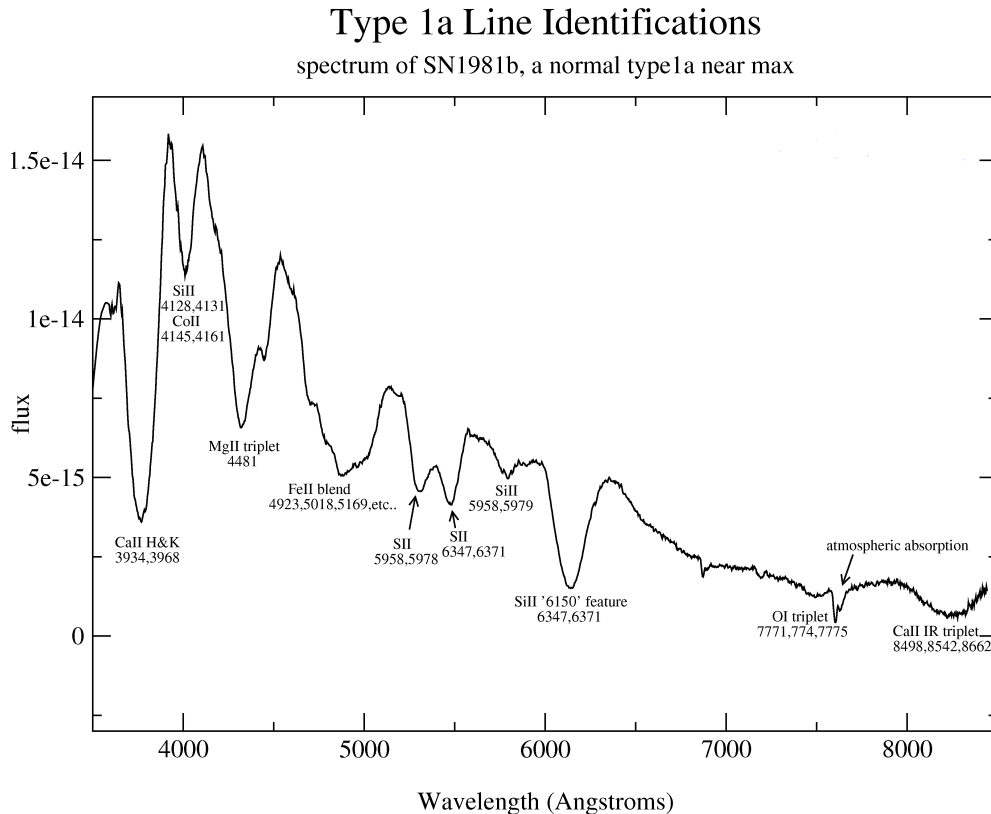


Figure 2.3: Spectrum of an SN Ia near maximum light (Kasen 2009). The broad Si II feature at  $6150 \text{ \AA}$  is used to identify a SN as one of the type Ia. Other features of S, Fe and Mg are also present. The Ca II H&K in the blue as well as the Ca II feature in the near infrared are typical for an SN Ia.

increases. As the atmosphere expands, it becomes optically thinner and the elements present in the deeper parts of the atmosphere contribute to the observed spectrum. After two weeks after the maximum, the spectrum is dominated by Fe II features. The iron is the decay product of the radioactive decay of the nickel and is produced in the inner most parts of the envelope. SN Ia have also been observed in the infrared. A few spectra in the infrared have been obtained (Meikle et al. 1996; Benetti et al. 2004; Pignata et al. 2008). In early spectra, one can observe features of Mg II and Si II, for instance, a Mg II feature can be found at  $\approx 1.1 \mu\text{m}$ . In later spectra, two emission features as a blend of Co II, Fe II and Ni II lines appear at  $\approx 1.5 \mu\text{m}$  and  $\approx 1.7 \mu\text{m}$ . Therefore, the evolution from intermediate mass elements to iron elements is observed in both optical and infrared.

Many observed features show an P Cygni profile. An P Cygni profile occurs in an expanding atmosphere, which is the case for a type Ia supernova. One can roughly assign different features to different expansion velocities. The expansion velocity of the deeper parts of the SN Ia atmosphere is slower than the one of the outer parts. In the figure 2.4 the formation of a P Cygni profile in an expanding atmosphere is illustrated. As the atmosphere is moving

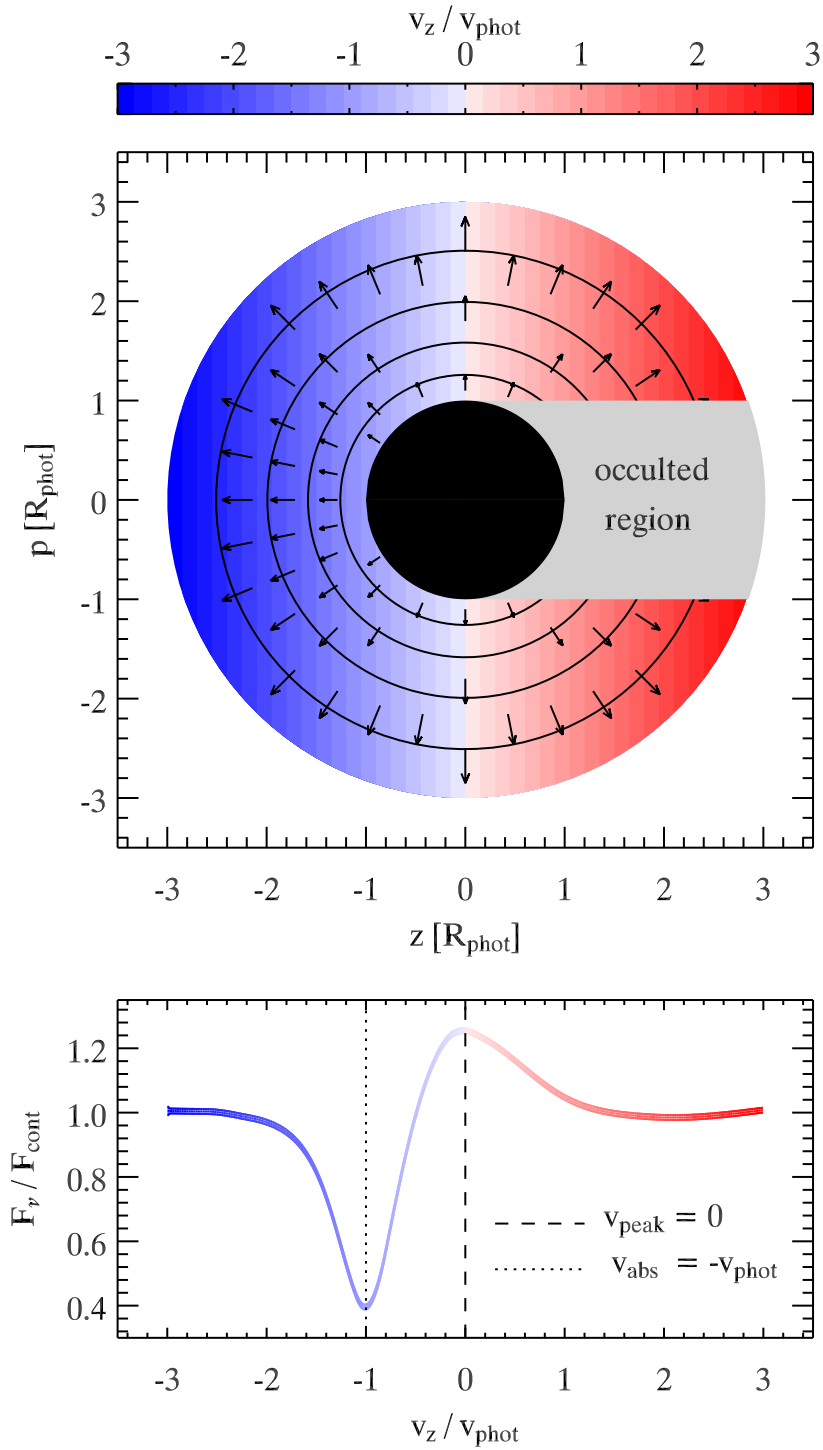


Figure 2.4: Formation of an P Cygni profile (Blondin 2009). The blueshifted absorption trough emerges from the part of the atmosphere that is moving towards the observer. The emission peak at the rest wavelength emerges from the emission lobe at the side of the atmosphere.

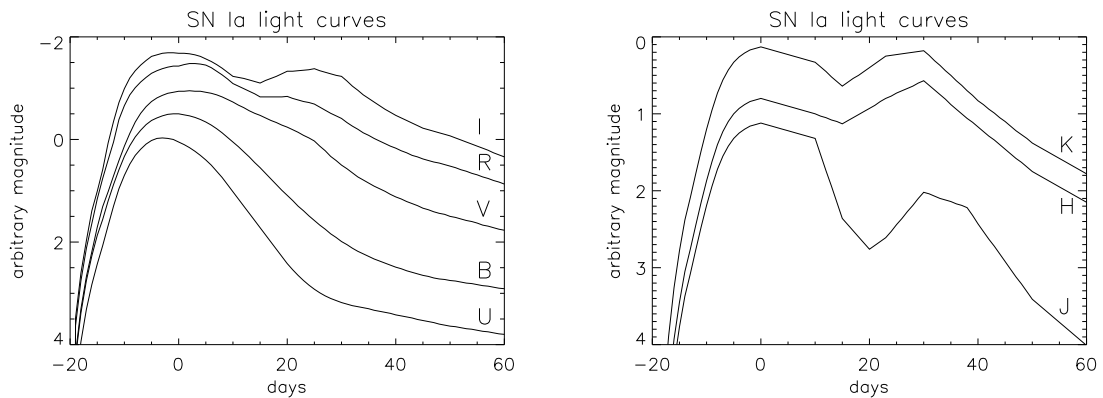


Figure 2.5: SN Ia light curves in different bands based on Branch normal template light curves given in Nugent et al. (2002).

towards the observer, the absorption trough is blue shifted due to the Doppler effect. At the side of the atmosphere an emission feature arises and is visible for the observer at the rest wavelength. The absorption takes place at a different velocity towards the observer than the emission. Therefore, the combined P Cygni feature consists of the blueshifted absorption feature and overlaps with the emission feature at the rest wavelength.

## 2.5 SN Ia in cosmology

The first suggestion to use SN Ia to determine cosmological parameters was expressed by Wilson (1939). Nowadays, type Ia supernovae possess an important role for measurements on cosmological scales. An overview about their use for cosmology is given in Leibundgut (2001) and Branch (1998). The SN Ia events can be used as distance indicators. A Hubble diagram obtained with measurements of distant SN Ia showed first the remarkable result that the expansion of the universe is accelerating instead of decelerating. This phenomenon is now called dark energy, and it is also confirmed by other observations like the measurements of the microwave background by the WMAP mission (Spergel et al. 2003). The existence of dark energy was also confirmed by X-ray observations of galaxy clusters (Allen et al. 2004, 2008) and the baryon acoustic oscillation (Percival et al. 2007). In this section, the use of SNe Ia for cosmological measurements is described in more detail.

### 2.5.1 Light curves

All observations of SN Ia, whether spectra or light curves, show significant similarities. A few of the SN Ia events show variations in the light curve or spectra. Branch et al. (1993) gave a definition for normal and peculiar SN Ia. Applying this classification scheme, about 85% of the SN Ia events still satisfy the definition of a normal SN Ia event.

The light curves of the normal type Ia supernovae are very similar. They all have a very steep rise at the beginning. The maximum luminosity is reached about 20 days after the initial explosion. After the maximum phase, the light curve is declining. Template light

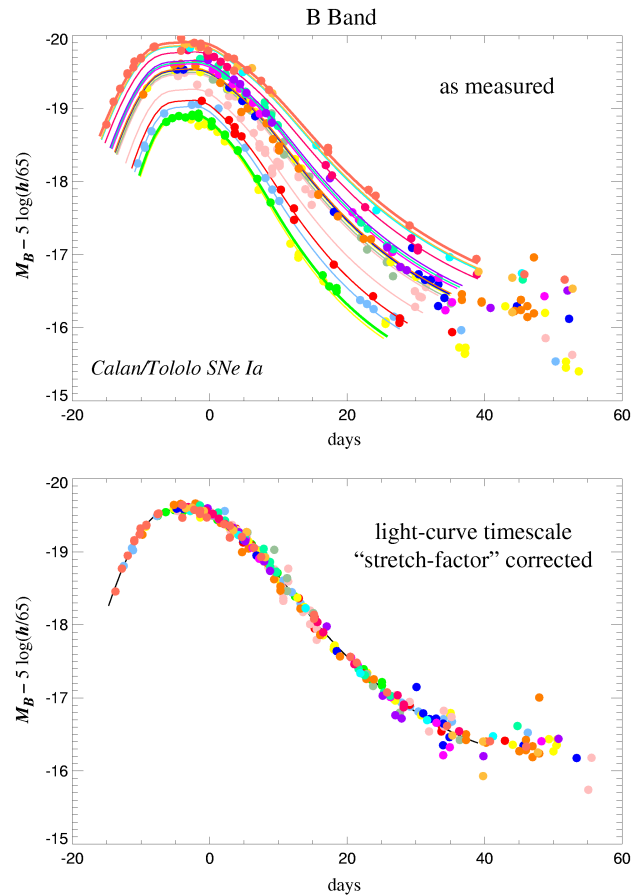


Figure 2.6: The light curves of SN Ia have similar shapes. A time scale stretch factor can correct them to one template light curve. Therefore, the absolute magnitude can be determined and the SN Ia can be used to measure distances on cosmological scale.

curves of different bands are shown in figure 2.5. As one can see, the maximum of the V band light curve is later than the one of the U band light curve. In the I band, there is a second maximum observed between 21 days and 30 days after the B band maximum (Ford et al. 1993; Lira et al. 1998; Meikle 2000). In the J, H and K band, there is also a second maximum observed, as one can see on the right hand side of figure 2.5. It is still unclear, what causes this second maximum in the infrared. Some SN Ia light curve do not show this second maximum (Filippenko et al. 1992; Turatto et al. 1996, 1998).

Despite the fact that there are deviations in the light curves, the question remains, whether one can still use the SN Ia as standard candles to measure distances. In fact, SN Ia are not standard candles, but an empirical result is that the light curves still have a similar shape and can be corrected to standard candles by introducing a correction factor. One approach is the Phillips relation  $\Delta m_{15}$  (Pskovskii 1977; Phillips 1993). It is defined as the decline of the

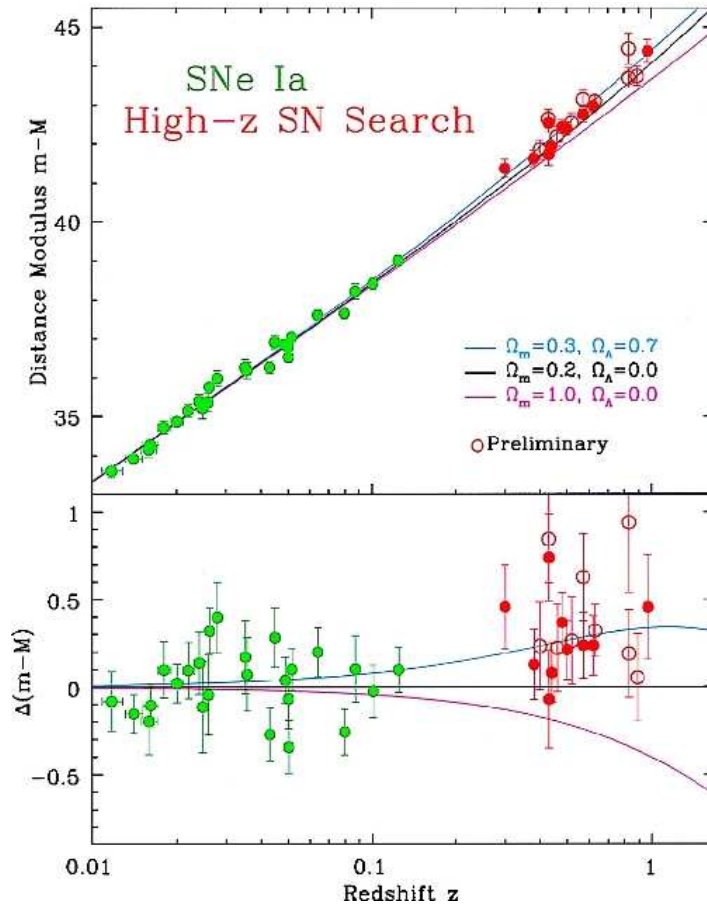


Figure 2.7: Measurements to obtain distances to high  $z$  galaxies have been performed by using SN Ia. The result is that the expansion of the universe is accelerating. This leads in conclusion to the existence of a phenomenon called dark energy (Schmidt et al. 1998).

magnitude in 15 days after the maximum in the B band. SN Ia light curves that show a steep decline have a brighter maximum luminosity, whereas fainter SN Ia have a flatter decline. Applying this relation, one can determine the absolute luminosity. Templates for light curves with different shapes and peak luminosity are presented by Hamuy et al. (1996). Another approach is the stretch factor introduced by Perlmutter et al. (1995, 1997), which normalizes the apparent peak magnitude. Figure 2.6 shows a plot of different SN Ia light curves that are corrected to a template light curve. By using this purely empirical, observational fact, every normal SN Ia light curve can be corrected and used to measure the peak luminosity. With this uniform peak luminosity, one can measure distances on cosmic scale.

## 2.5.2 Dark energy

Although they are not perfect standard candles, SN Ia can still be used to accurately measure distances on cosmological scale. A search for distant SN Ia at higher redshift to determine cosmological parameters was proposed by Goobar & Perlmutter (1995). The Supernova

Cosmology Project (Perlmutter et al. 1999) and the High- $z$  Supernova Search (Schmidt et al. 1998) have worked on that topic. They both found the result that the distant SN Ia are fainter than the local ones. The explanation is that the universe is expanding, and this expansion is accelerating instead of decelerating. A decelerating universe is the standard expectation, because the gravitation should slow down the initial expansion. In figure 2.7, the results of the search for highly redshifted supernovae is presented. The figure shows the observed magnitude of SN Ia plotted against the measured redshift. As one can see, the best fit to the data indicates that the expansion of the universe is accelerating. This phenomenon is called the dark energy. This remarkable result has also been confirmed by the WMAP mission, which measured the cosmic microwave background fluctuations (Spergel et al. 2003, 2007). The cosmological measurements indicate that the universe consists to about 75% of dark energy. Another 20% is the dark matter, whose real nature again is unknown. Therefore, the known and observable matter makes up only 5% of the content of the universe. Future missions need to be launched to find more highly redshifted SN Ia and measure the behavior of the dark energy more accurately. One of these projects is the joint dark energy mission (JDEM) (Crofts et al. 2005). The recently launched Planck mission (The Planck Collaboration 2006) will observe the fluctuations of the cosmic microwave background with higher resolution in order to learn more about the content and origin of the universe.

# Chapter 3

## Modeling atmospheres with PHOENIX

In this chapter, an overview about the modeling of atmospheres in general is presented. The main obstacle is the solution of the radiative transfer problem. The quantities to describe the stellar atmosphere and the radiation field are introduced in this chapter. The approach to solve the radiative transfer equation is presented. The details of the general purpose stellar atmosphere code PHOENIX are described. One application of PHOENIX and the focus of this work is the calculation of SN Ia model atmospheres and their spectra.

### 3.1 Radiative transfer

This section is about the solution of the radiative transfer problem in the modeling of stellar and stellar-like atmospheres. There exist a lot of overviews about the radiative transfer problem. For instance, Rutten (2003) and Mihalas (1970, 1978) give an introduction to radiative transfer used for the modeling of stellar atmospheres. The basic quantities and equations needed to solve the radiative transfer problem are introduced and discussed in this section. The descriptions in this chapter stick closely to the overview of Rutten (2003).

#### 3.1.1 Radiation field

The important quantities to describe the radiation field in a stellar atmosphere are introduced in the following. The specific intensity  $I_\nu$  is the proportionality coefficient in the equation, which is given by

$$dE_\nu = I_\nu(\vec{r}, \vec{l}, t)(\vec{l} \cdot \vec{n})dA dt d\nu d\Omega, \quad (3.1)$$

where  $dE_\nu$  is the amount of energy transported through the area  $dA$ , at the location  $\vec{r}$ , with  $\vec{n}$  the normal to  $dA$ , between times  $t$  and  $t + dt$ , in the frequency band between  $\nu$  and  $\nu + d\nu$ , over the solid angle  $d\Omega$  around the direction  $\vec{l}$ . The same equation can be written for the wavelength dependent specific intensity, where the relation between both the specific intensities is given by  $I_\lambda = I_\nu c / \lambda^2$ . The specific intensity is a monochromatic quantity. To obtain the total specific intensity,  $I_\nu$  has to be integrated over all frequencies  $I = \int I_\nu d\nu$ .

Another quantity of the radiation field is the mean intensity  $J_\nu$ , which is the specific intensity averaged over all directions and given by

$$J_\nu(\vec{r}, t) = \frac{1}{4\pi} \int I_\nu d\Omega. \quad (3.2)$$

This quantity can be used if only the presence of photons is of interest and not their origin. This is the case if the amount of radiative excitations and ionizations needs to be determined.

The monochromatic flux is the net flow of energy per second through an area at location  $\vec{r}$  perpendicular to  $\vec{n}$  and given by

$$F_{\nu}(\vec{r}, \vec{n}, t) = \int I_{\nu} \cos \theta d\Omega. \quad (3.3)$$

The monochromatic flux is a vector and is used to describe the energetics of radiative transfer through stellar atmospheres. In a one-dimensional stellar atmosphere, the flux can be divided into fluxes of inwards and outwards in radial direction

$$F_{\nu}(z) = F_{\nu}^{+}(z) - F_{\nu}^{-}(z), \quad (3.4)$$

with the outward flux  $F_{\nu}^{+}(z)$  and the inward flux  $F_{\nu}^{-}(z)$ .

The radiation pressure  $p_{\nu}$  is given by

$$p_{\nu} = \frac{1}{c} \int I_{\nu} \cos^2 \theta d\Omega, \quad (3.5)$$

which is analogous to gas pressure as it is the pressure of the photon gas.

Introducing  $\mu = \cos \theta$ , the first three moments of the specific intensity are

$$J_{\nu}(z) = \frac{1}{2} \int_{-1}^{+1} I_{\nu} d\mu \quad (3.6)$$

$$H_{\nu}(z) = \frac{1}{2} \int_{-1}^{+1} \mu I_{\nu} d\mu \quad (3.7)$$

$$K_{\nu}(z) = \frac{1}{2} \int_{-1}^{+1} \mu^2 I_{\nu} d\mu \quad (3.8)$$

The mean intensity  $J_{\nu}$  has already been introduced. The second moment of the intensity is called the Eddington flux and is related to the monochromatic flux  $F_{\nu}$  by  $H_{\nu} = F_{\nu}/4\pi$ . The quantity  $K_{\nu}$  is related to the radiation pressure by  $p_{\nu} = (4\pi/c)K_{\nu}$ .  $J_{\nu}$  and  $K_{\nu}$  are always positive.

### 3.1.2 Source function

The material that is present in the stellar atmosphere interacts with the radiation field. Meaning, the local energy of the radiation field or the intensities are changed by this interactions. An excited atom emits energy in form of a photon when it deexcites. Thus, this photon is added to the radiation field. The change of the specific intensity is given by

$$dI_{\nu}(s) = j_{\nu}(s) ds, \quad (3.9)$$

where  $dI_{\nu}(s)$  is the increasing specific intensity along a geometrical path length of  $ds$ . The monochromatic emissivity is represented by  $j_{\nu}(s)$ . All these quantities are depending on the frequency of the radiation.

The intensity can also change due to absorption or scattering of photons by atoms in the material. There are different ways to define a monochromatic extinction coefficient. The monochromatic extinction per particle is defined as

$$dI_\nu = -\sigma_\nu n I_\nu ds, \quad (3.10)$$

where  $\sigma_\nu$  is the monochromatic extinction coefficient or cross-section and  $n$  the absorber density in particles per  $\text{cm}^3$ . The monochromatic extinction per path length  $\chi_\nu$  is defined by

$$dI_\nu = -\chi_\nu I_\nu ds, \quad (3.11)$$

where  $\chi_\nu = \sigma_\nu n$  is the relation between both extinction coefficients. The monochromatic extinction coefficient  $\chi_\nu$  is also called opacity. The extinction coefficient includes absorption and scattering.

A quantity often used for the description of stellar atmospheres is the optical depth  $\tau_\nu$ . It is defined by

$$\tau_\nu(z_0) = \int_{z_0}^{\infty} \chi_\nu dz. \quad (3.12)$$

The optical depth is an indication for the observer from which part of the stellar atmosphere the photons he observes are originating. Again, the optical depth depends on the frequency.

The source function  $S_\nu$  is introduced as the quotient of the emissivity and the extinction coefficient per particle

$$S_\nu = \frac{j_\nu}{\chi_\nu}. \quad (3.13)$$

In fact, the source function is a sum of the emissivity and extinction coefficients at the frequency  $\nu$ , when multiple process contribute to the local emission and extinction. The source function is an important quantity used for the description of radiative transfer.

In case of a two level atom including scattering the source function is given by

$$S_\nu = (1 - \varepsilon_\nu) B_\nu + \varepsilon_\nu J_\nu, \quad (3.14)$$

where  $B_\nu$  is the Planck-function and  $\varepsilon_\nu$  the probability of photon destruction, which is given by

$$\varepsilon_\nu = \frac{\alpha_\nu^a}{\alpha_\nu^a + \alpha_\nu^s}. \quad (3.15)$$

$\varepsilon_\nu$  is the amount of absorption of the overall extinction, which consists of the scattering  $\alpha_\nu^s$  and absorption  $\alpha_\nu^a$  coefficients.

### 3.1.3 Radiative transfer equation

The main equation is the radiation transport equation, which is given by

$$\frac{\partial I_\nu}{\partial s} = j_\nu - \alpha_\nu I_\nu, \quad (3.16)$$

where  $s$  is the geometrical path along a ray. This equation can be rewritten for the use in stellar atmospheres. With the introduced source function and optical depth, it is given by

$$\frac{dI_\nu}{d\tau_\nu} = S_\nu - I_\nu. \quad (3.17)$$

This equations states that photons do not decay spontaneously. The intensity along a ray does not change unless photons are added to the beam or taken from it. Without such processes, the intensity stays constant.

The formal solution of the radiation transport equation is for the inward direction given by

$$I_\nu^-(\tau_\nu, \mu) = - \int_0^{\tau_\nu} S_\nu(t_\nu) e^{-(t_\nu - \tau_\nu)/\mu} dt_\nu / \mu, \quad (3.18)$$

and for the outward direction the formal solution is given by

$$I_\nu^+(\tau_\nu, \mu) = \int_{\tau_\nu}^{\infty} S_\nu(t_\nu) e^{-(t_\nu - \tau_\nu)/\mu} dt_\nu / \mu. \quad (3.19)$$

For expanding atmospheres the radiation transport equation becomes more complex. The spherical symmetric special relativistic radiative transfer equation for expanding atmospheres is given by Mihalas & Mihalas (1984)

$$\begin{aligned} & \gamma(1 + \beta\mu) \frac{\partial I_\nu}{\partial t} + \gamma(\mu + \beta) \frac{\partial I_\nu}{\partial r} \\ & + \frac{\partial}{\partial \mu} \left\{ \gamma(1 - \mu^2) \left[ \frac{1 + \beta\mu}{r} - \gamma^2(\mu + \beta) \frac{\partial \beta}{\partial r} - \gamma^2(1 + \beta\mu) \frac{\partial \beta}{\partial t} \right] I_\nu \right\} \\ & - \frac{\partial}{\partial \nu} \left\{ \gamma\nu \left[ \frac{\beta(1 - \mu^2)}{r} + \gamma^2\mu(\mu + \beta) \frac{\partial \beta}{\partial r} + \gamma^2\mu(1 + \beta\mu) \frac{\partial \beta}{\partial t} \right] I_\nu \right\} \\ & + \gamma \left\{ \frac{2\mu + \beta(3 - \mu^2)}{r} + \gamma^2(1 + \mu^2 + 2\beta\mu) \frac{\partial \beta}{\partial r} + \gamma^2 [2\mu + \beta(1 + \mu^2)] \frac{\partial \beta}{\partial t} \right\} I_\nu \\ & = \eta_\nu - \chi_\nu I_\nu, \end{aligned} \quad (3.20)$$

where  $\beta = v/c$  is the velocity in units of speed of light and  $\gamma = (1 - \beta^2)^{-1/2}$  the usual local Lorentz factor. The emissivity  $\eta_\nu$  is given by

$$\eta_\nu = \kappa_\nu S_\nu + \sigma_\nu J_\nu + \sum_{\text{lines}} \sigma_l(\nu) \int \phi_l J_\nu d\nu, \quad (3.21)$$

where  $\sigma_l$  are the line scattering source coefficients and  $\phi_l$  the line profile function. See Hauschildt & Baron (1999) for more details about radiative transfer in expanding atmospheres. This equation is often solved by using the assumption of time-independence  $\partial I_\nu / \partial t = 0$  and assuming a monotonic velocity field.

### 3.1.4 $\Lambda$ -operator and OS method

The mean intensity  $J_\nu$  is obtained from the source function  $S_\nu$  by the solution of the radiative transfer equation. Introducing the  $\Lambda_\nu$  operator, the radiative transfer equation can be written as

$$J_\lambda = \Lambda_\lambda S_\lambda. \quad (3.22)$$

For the case of a two level atom the equation can be written as

$$\bar{J} = \Lambda S, \quad (3.23)$$

where  $\bar{J} = \int \phi(\lambda) J_\lambda d\lambda$  and  $\Lambda = \int \phi(\lambda) \Lambda_\lambda d\lambda$  with the normalized line profile  $\phi(\lambda)$ . The source function for the simple case of a two-level atom is given by  $S = (1 - \epsilon)\bar{J} + \epsilon B$ .

The following equations are used for an iteration scheme in order to obtain the solution of the radiative transfer:

$$\bar{J}_{\text{new}} = \Lambda S_{\text{old}}, \quad S_{\text{new}} = (1 - \epsilon)\bar{J}_{\text{new}} + \epsilon B. \quad (3.24)$$

For large optical depths and small  $\epsilon$  this iteration scheme converges extremely slowly.

A faster way to obtain a solution for the radiative transfer equation is the operator splitting method. For this operator perturbation method (Cannon 1973), a new approximate  $\Lambda$ -operator  $\Lambda^*$  is introduced, which is similar to the original  $\Lambda$ -operator. Meaning  $\Lambda$  can be written as

$$\Lambda = \Lambda^* + (\Lambda - \Lambda^*). \quad (3.25)$$

Rewriting equation 3.23, the radiative transfer equation is given by

$$\bar{J}_{\text{new}} = \Lambda^* S_{\text{new}} + (\Lambda - \Lambda^*) S_{\text{old}}. \quad (3.26)$$

Basing on the new approach, a new iteration scheme is introduced for the simple case of an two level atom. The following equation for the iteration scheme is then applied:

$$[1 - \Lambda^*(1 - \epsilon)]\bar{J}_{\text{new}} = \bar{J}_{\text{fs}} - \Lambda^*(1 - \epsilon)\bar{J}_{\text{old}}, \quad (3.27)$$

where  $\bar{J}_{\text{fs}} = \Lambda S_{\text{old}}$ . This equation is used to obtain the new value for  $J_{\text{new}}$ . The next step is then to obtain the new source function  $S_{\text{new}}$  and go on with the next iteration cycle. The difference is that  $\Lambda^*$  is used instead of  $\Lambda$ . By using a good choice for the  $\Lambda^*$ -operator computation time can be saved. The OS-method converges faster than the classical  $\Lambda$ -iteration. The choice of a reasonable  $\Lambda^*$ -operator is important. In Hauschildt & Baron (1999), a method to obtain a reasonable  $\Lambda^*$ -matrix is described.

### 3.1.5 Line transitions

Line transitions between two levels in an atom can occur by different processes. Here the bound-bound transitions between a lower  $l$  and upper  $u$  energy level of an atom are discussed.

The first possible line transition is the spontaneous radiative deexcitation. The Einstein coefficient for spontaneous deexcitation is given by

$$A_{ul} = \text{transition probability for spontaneous deexcitation} \\ \text{from state } u \text{ to state } l \text{ per second per particle in state } u. \quad (3.28)$$

In the absence of other transitions, the mean lifetime of particles in state  $u$  is given by  $\Delta t = 1/A_{ul}$ .

Another line transition is the radiative excitation of an atom. The Einstein coefficient for this transition is given by

$$B_{lu}\bar{J}_{\nu_0}^{\phi} = \text{number of radiative excitations from state } l \\ \text{to state } u \text{ per second per particle in state } l, \quad (3.29)$$

where the index  $\nu_0$  is defining a specific spectral line of which the extinction profile  $\phi(\nu - \nu_0)$  is used in the weighting of the angle-averaged exciting radiation field over the spectral extent of the line

$$\bar{J}_{\nu_0}^{\phi} = \int_0^{\infty} J_{\nu} \phi(\nu - \nu_0) d\nu, \quad (3.30)$$

where  $\int \phi(\nu - \nu_0) d\nu = 1$ . The Einstein coefficient is represented by  $B_{lu}$ , which is the number of radiative excitations from state  $l$  to state  $u$  per second per particle in state  $l$ ,

The induced radiative deexcitation is another possible transition. The Einstein coefficient is defined by

$$B_{ul}\bar{J}_{\nu_0}^{\chi} = \text{number of induced radiative deexcitations from state } u \\ \text{to state } l \text{ per second per particle in state } u, \quad (3.31)$$

which is similarly to  $B_{lu}$  but with frequency averaging

$$\bar{J}_{\nu_0}^{\chi} = \frac{1}{2} \int_0^{\infty} \int_{-1}^{+1} I_{\nu} \chi(\nu - \nu_0) d\mu d\nu = \int_0^{\infty} J_{\nu} \chi(\nu - \nu_0) d\nu, \quad (3.32)$$

in which  $\chi(\nu - \nu_0)$  is the area-normalized profile shape for induced emission.

A transition between two bound-bound states can also happen by collisional processes, such as collisional excitation or collisional deexcitation. The Einstein coefficients are given by

$$C_{lu} = \text{number of collisional excitations from state } l \\ \text{to state } u \text{ per second per particle in state } l. \quad (3.33)$$

$$C_{ul} = \text{number of collisional deexcitations from state } u \\ \text{to state } l \text{ per second per particle in state } u. \quad (3.34)$$

The transition rates are given by

$$n_i C_{ij} = n_i N_e \int_{\nu_0}^{\infty} \sigma_{ij}(u) u f(u) du, \quad (3.35)$$

with the electron density  $N_e$ , the electron collision cross-section  $\sigma_{ij}(u)$ , the area-normalized velocity  $f(u)$ , and the threshold velocity  $u_0$  with  $(1/2)mu_0^2 = hv_0$ .

There are relations between the three Einstein coefficients

$$\frac{B_{lu}}{B_{ul}} = \frac{g_u}{g_l}, \quad \frac{A_{ul}}{B_{ul}} = \frac{2h\nu^3}{c^2}, \quad (3.36)$$

and

$$\frac{C_{ul}}{C_{lu}} = \frac{g_l}{g_u} e^{E_{ul}/kT}, \quad (3.37)$$

where  $E_{ul}$  is the transition energy. These relations are valid for thermal equilibrium.

### 3.1.6 Continuum transitions

Line transitions can also occur as bound-free transitions. For hydrogen and hydrogen-like ions the Kramer formula gives the extinction cross-section

$$\sigma_{\nu}^{\text{bf}} = 2,815 \times 10^{29} \frac{Z^4}{n^5 \nu^3} g_{\text{bf}} \quad \text{for } \nu \geq \nu_0, \quad (3.38)$$

with  $n$  the principal quantum number of the level  $i$  from which the atom or ion is ionized,  $Z$  the ion charge,  $\nu$  in Hz and  $g_{\text{bf}}$  the dimensionless Gaunt factor, a quantummechanical correction factor of order of unity. The cross-section below the threshold  $\nu_0$  is zero, because the threshold energy is required minimum.

A last possible transition are the free-free transitions, which have  $S_{\nu} = B_{\nu}$ . The extinction coefficient per particle is given by

$$\sigma_{\nu}^{\text{ff}} = 3.7 \cdot 10^8 N_e \frac{Z^2}{T^{1/2} \nu^3} g_{\text{ff}}, \quad (3.39)$$

with  $g_{\text{ff}}$  a Gaunt factor of order of unity. There is no threshold frequency.

### 3.1.7 Scattering

Atoms and photons can undergo an elastic process, which is called scattering. In the elastic scattering process the energy of the photon is not changed only its direction. This process is an interaction between material and radiation, but it is uncoupled. The radiation field and material can therefore have a different temperature.

Thomson scattering is the scattering of photons by free electrons. The cross-section of the frequency-independent process is given by

$$\sigma_{\nu}^T = \sigma^T = \frac{8\pi}{3} r_e^2 = 6,65 \times 10^{25} \text{ cm}^2. \quad (3.40)$$

For high-energy photons, Thomson scattering is replaced by Compton scattering. Compton scattering is an inelastic scattering process where the energy of the photon is changed.

Rayleigh scattering is the scattering of photons with  $\nu \ll \nu_0$  by bound electrons. The cross-section for this process is given by

$$\sigma_{\nu}^R \approx f_{lu} \sigma^T \left( \frac{\nu}{\nu_0} \right)^4, \quad (3.41)$$

where the oscillator strength  $f_{lu}$  and the frequency  $\nu_0$  characterize the major bound-bound “resonance transitions” of the bound electron.

Another scattering process is the line scattering. Here, a photon is absorbed and emitted by an atom. If this occurs in a short time scale of about  $10^{-9}$ s this process looks like scattering. Thus, this process is called line scattering.

## 3.2 Modeling atmospheres with PHOENIX

The methods to obtain the solution of the radiative transfer equation were given in the previous section. Now the focus lies on the modeling of stellar atmospheres. In the following the properties of the assumption of LTE or NLTE for the stellar atmosphere is discussed. The iteration scheme of PHOENIX is presented.

### 3.2.1 LTE

One assumption for the modeling of stellar atmospheres is that the atmosphere is considered to be in local thermodynamic equilibrium (LTE). This means that a temperature can be assigned to a local part of the atmosphere, where the material is treated as in thermodynamic equilibrium (TE). The collisions control the energy partitioning in the medium more strictly than that they control the energy partitioning of the radiation. With the assumption of LTE, the properties of the matter and radiation can be derived easily.

First, the properties of matter in LTE are discussed. The particles of the gas have a thermal velocity. The distribution of this velocity is described by the Maxwell distribution, which is given by

$$\left[ \frac{n(u)}{N} du \right]_{\text{LTE}} = \left( \frac{m}{2\pi kT} \right)^{3/2} 4\pi u^2 e^{-(1/2)mu^2/kT} du, \quad (3.42)$$

where  $N$  is the total number of particles with mass  $m$  per volume. The number of particles with a velocity  $u$  is represented by  $n(u)$ .  $k$  is the Boltzmann constant and  $T$  the material temperature. The most probable speed is given by  $u_p = \sqrt{2kT/m}$ , and the averaged speed is given by  $\langle u \rangle = \sqrt{3kT/m}$ .

The Boltzmann excitation distribution is given by

$$\left[ \frac{n_{r,s}}{n_{r,t}} \right]_{\text{LTE}} = \frac{g_{r,s}}{g_{r,t}} e^{-(\chi_{r,s} - \chi_{r,t})/kT}, \quad (3.43)$$

where  $n_{r,s}$  is the number of atoms per  $\text{cm}^3$  in level  $s$  of ionization stage  $r$ ,  $\chi_{r,s}$  the excitation energy of level  $s$  in stage  $r$ , measured from the ground level  $(r, 1)$  of stage  $r$ . A radiative

transition has the energy of  $\chi_{r,s} - \chi_{r,t} = h\nu$  between levels  $(r,s)$  and  $(r,t)$ , where level  $s$  is higher than level  $t$ .

The Saha distribution for the population ratio between the ground levels of successive ionization stages is given by

$$\left[ \frac{n_{r+1,1}}{n_{r,1}} \right]_{\text{LTE}} = \frac{1}{N_e} \frac{2g_{r+1,1}}{g_{r,1}} \left( \frac{2\pi m_e kT}{h^2} \right)^{3/2} e^{-\chi_r/kT}, \quad (3.44)$$

where  $N_e$  is the electron density,  $m_e$  the electron mass,  $n_{r+1,1}$  and  $n_{r,1}$  the population densities of the two ground states of the successive ionization stages  $r$  and  $r+1$ ,  $\chi_r$  the ionization energy of stage  $r$  and  $g_{r+1,1}$  and  $g_{r,1}$  the statistical weights of the two ground levels. The Planck constant is  $h$ .

The Saha-Boltzmann distribution combines the Boltzmann and Saha distribution. The population ratio between a particular level  $i$  and the ion state  $c$  to which it ionizes is given by

$$\left[ \frac{n_c}{n_i} \right]_{\text{LTE}} = \frac{1}{N_e} \frac{2g_c}{g_i} \left( \frac{2\pi m_e kT}{h^2} \right)^{3/2} e^{-\chi_{ci}/kT}, \quad (3.45)$$

where  $n_i$  is the occupation number of level  $i$  and  $n_c$  is for state  $c$ . The ionization energy from  $i$  to  $c$  is given by  $\chi_{ci}$ . So the occupation number of each atom level is in LTE determined by the local temperature.

The radiation in LTE can be described by the temperature and the Planck function, which is given by

$$B_\nu(T) = \frac{2h\nu^3}{c^2} \frac{1}{e^{h\nu/kT} - 1} = [S_\nu^l]_{\text{LTE}} \quad (3.46)$$

Hence, for the case of LTE the source function is given by the Planck function if scattering is neglected.

The integral of the Planck function over all frequencies gives the Stefan-Boltzmann law

$$B(T) = \int_0^\infty B_\nu d\nu = \frac{\sigma}{\pi} T^4. \quad (3.47)$$

where  $\sigma$  is the Stefan-Boltzmann constant, which is given by

$$\sigma = \frac{2\pi^5 k^4}{15h^3 c^2} = 6,67 \times 10^{-5} \text{erg cm}^{-2} \text{K}^{-4} \text{s}^{-1}. \quad (3.48)$$

The luminosity is the amount of energy a star radiates per unit time

$$L = 4\pi R^2 \sigma T_{\text{eff}}^4, \quad (3.49)$$

where  $R$  is the radius of the star. The effective temperature  $T_{\text{eff}}$  is introduced here. It is the temperature of a black body that has the same luminosity per surface area as the star.

### 3.2.2 NLTE

In this section the properties of matter, which is not in local thermodynamic equilibrium is discussed. This is also called nonLTE or NLTE. For the material this means that the occupation numbers of the levels of an atom are not determined by the Saha-Boltzmann distribution. But it is assumed that the gas is in statistical equilibrium, which means that the radiation fields and level populations do not vary in time. The statistical equilibrium equations are given by

$$\sum_{j<i} n_j (R_{ji} + C_{ji}) - n_i \left[ \sum_{j<i} \left( \frac{n_j^*}{n_i^*} \right) (R_{ij} + C_{ji}) + \sum_{j>i} (R_{ij} + C_{ij}) \right] + \sum_{j>i} n_j \left( \frac{n_i^*}{n_j^*} \right) (R_{ji} + C_{ij}) = 0, \quad (3.50)$$

with  $n_i$  the actual nonLTE population of a particular level, and  $j$  stepping over all those levels. The rates by radiation are  $R_{ij}$  and  $R_{ji}$ , and the rates by collisions are  $C_{ij}$  and  $C_{ji}$ .  $n_i^*$  denotes the LTE population density of the level  $i$ , which is given by

$$n_i^* = \frac{g_i}{g_k} n_k \frac{3h^3 n_e}{(2\pi m)^{3/2} (kT)^{3/2}} \exp\left(-\frac{E_i - E_k}{kT}\right), \quad (3.51)$$

where  $n_k$  is the actual population density of the ground state of the next higher ionization stage of the same element,  $g_i$  and  $g_k$  are the statistical weights of the levels  $i$  and  $k$ . The excitation energy of level  $i$  is  $E_i$  and the ionization energy from the ground state to the corresponding ground state of the next higher ionization stage is given by  $E_k$ . The absorption radiative rate coefficients are given by

$$R_{ij} = \frac{4\pi}{hc} \int_0^\infty \alpha_{ij}(\lambda) J_\lambda(\lambda) \lambda d\lambda, \quad (3.52)$$

whereas the emission radiative rates are given by

$$R_{ji} = \frac{4\pi}{hc} \int_0^\infty \alpha_{ij}(\lambda) \left( \frac{2hc^2}{\lambda^5} + J_\lambda(\lambda) \right) \exp\left(-\frac{hc}{k\lambda T}\right) \lambda d\lambda. \quad (3.53)$$

$C_{ij}$  and  $C_{ji}$  are describing the rates for collisional processes such as collisions of electrons.

### 3.2.3 Temperature correction

For most stellar atmospheres the assumption of radiative equilibrium is adequate. This means that the luminosity is constant in all layers of a model atmosphere. To obtain a radiative equilibrium state of the model atmosphere PHOENIX has a temperature correction procedure using an Unsöld-Lucy method (Hauschildt et al. 2003). After each radiative transfer step the temperature is corrected to obtain a model atmosphere structure that is in radiative equilibrium. The wavelength-averaged absorption and extinction coefficients are defined as

$$\kappa_P = \left( \int_0^\infty \kappa_\lambda B_\lambda d\lambda \right) / B \quad (3.54)$$

$$\kappa_J = \left( \int_0^\infty \kappa_\lambda J_l d\lambda \right) / J \quad (3.55)$$

$$\chi_J = \left( \int_0^\infty \chi_\lambda F_l d\lambda \right) / F \quad (3.56)$$

The temperature correction  $\delta B$  is given by

$$\delta B(r) = \frac{1}{\kappa_P} \left[ \kappa_J J - \kappa_P B + \dot{S} / (4\pi) \right] - \left[ 2(H(\tau = 0) - H_0(\tau = 0)) - \frac{1}{fqr^2} \int_r^R qr'^2 \chi_F(H(r') - H_0(r')) dr' \right] \quad (3.57)$$

This equation has been taken from Hauschildt & Baron (1999).  $H_0(\tau)$  is the target luminosity at an optical depth  $\tau$ . The observed luminosity  $H_0(0)$  is an input parameter. Here,  $q$  is a sphericity factor, which is given by

$$q = \frac{1}{r^2} \exp \left( \int_{r_{core}}^r \frac{3f-1}{r'f} dr' \right), \quad (3.58)$$

where  $r_{core}$  is the inner radius of the atmosphere,  $R$  is the total radius,  $f(\tau) = K(\tau)/J(\tau)$  the Eddington factor, and  $K$  is the second angular momentum of the mean intensity.  $\dot{S}$  describes all additional energy sources such as mechanical energy supplied by winds or nonthermal ionization due to  $\gamma$ -ray deposition.

### 3.2.4 Iteration scheme

The figure 3.1 illustrates the iteration scheme of PHOENIX. The calculation starts with an initial guess of the temperature, density and pressure structure. The first step is to solve the hydrostatic or hydrodynamic equations. The line selection then selects the needed atomic lines. For the line list selection, the following databases can be chosen: APED (APED 2009), CHIANTI (Dere et al. 1997, 2001) and the Kurucz atomic line data (Kurucz & Bell 1995). The next step is the solution of the radiative transfer equation. This is done for each wavelength point during the wavelength loop. Here the parallel implementation of PHOENIX (Hauschildt et al. 1997; Baron & Hauschildt 1998; Hauschildt et al. 2001) can be used to compute the radiative transfer faster by using the advantages of parallel computers. The operator splitting method is used to obtain the radiative transfer solution. Here the opacities, source functions and then the intensities are calculated. If NLTE is selected, the radiative rates are also calculated. With the assumption of statistical equilibrium, the rate equations are then solved in the next step. As a result, the departure coefficients for all levels of the species in NLTE are updated. In the last step the temperature correction updates the temperatures of all layers to obtain a temperature structure, where the atmosphere is in radiative equilibrium. This iteration process is performed until the correct temperature structure has been obtained. The result is an atmosphere structure in radiative equilibrium. One can then solve the radiation field and obtain the spectrum as seen by an observer.

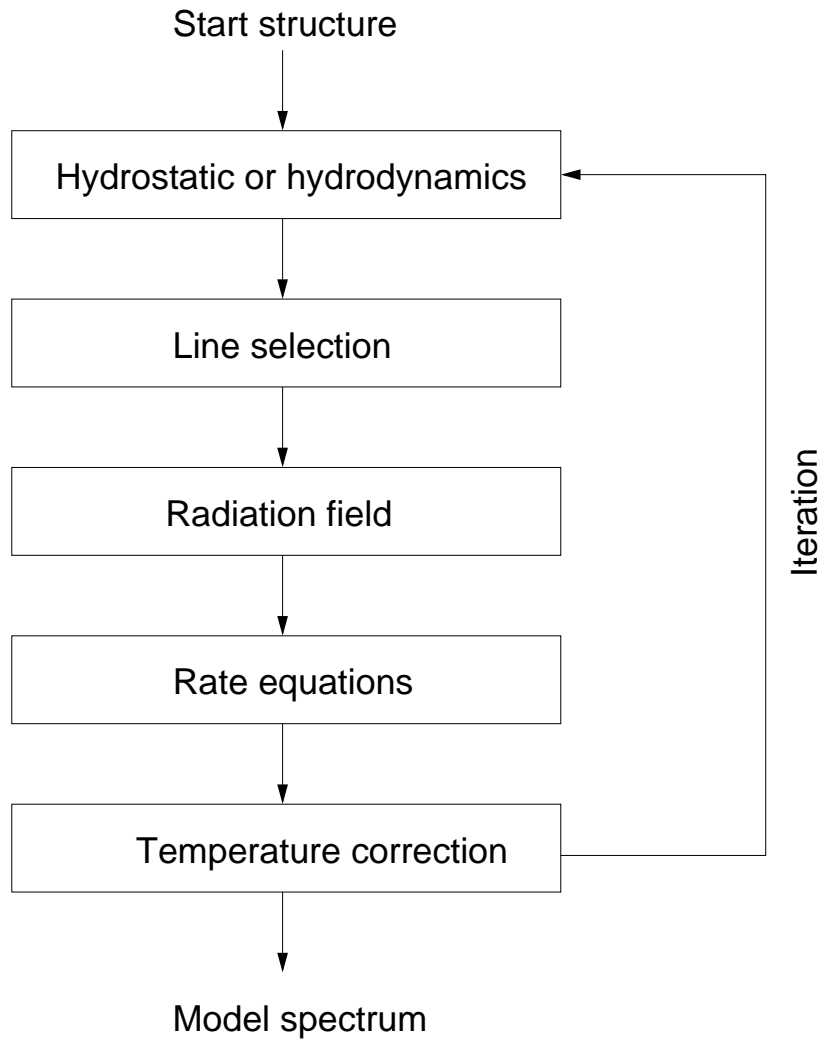


Figure 3.1: Iteration scheme of PHOENIX.

# Chapter 4

## Time dependent radiative transfer

The approach to solve the radiative transfer problem time independently is in most cases adequate. Nevertheless, it is interesting to solve the time dependent radiative transfer equation to actually see influences of time dependence and to test the accuracy of the assumption of time independence. It may also be necessary to solve the radiative transfer time dependently, if one wants to calculate other time dependent problems as, for instance, the hydrodynamical evolution of an SN Ia atmosphere. As one goal of this work is the calculation of SN Ia light curves, the time dependent radiative transfer might be necessary.

In the first section of this chapter, time dependence is introduced into the spherical symmetric radiative transfer equation. To achieve this, the radiative transfer equation is extended and now solved including the time dependent terms. The implementation and the two implemented discretization methods are presented in detail. In the second section, numerous test calculations confirm that the newly implemented time dependence is producing reasonable results.

### 4.1 Time dependent radiative transfer

So far, the radiative transfer is solved by using the time independent radiative transfer equation. The radiative transfer equation is then equation 3.20, which has been taken from Mihalas & Mihalas (1984). For an implementation of the time dependence in the radiative transfer itself, the spherical symmetric special relativistic radiative transfer equation (SSRTE) for expanding atmospheres (Hauschildt & Baron 1999) is extended, so that the additional time dependent term is given by

$$\frac{\gamma}{c} (1 + \beta\mu) \frac{\partial I}{\partial t}, \quad (4.1)$$

where  $\beta = \frac{v}{c}$  is the velocity in units of the speed of light  $c$ , and  $\gamma = (1 - \beta^2)^{-1/2}$  is the usual local Lorentz factor.  $I$  is the intensity,  $\mu$  is the cosine of the angle between the radial direction and the propagation vector of the light. Using the notation of Hauschildt & Baron (2004), the comoving frame SSRTE with the additional time dependent term is given by

$$a_t \frac{\partial I}{\partial t} + a_r \frac{\partial I}{\partial r} + a_\mu \frac{\partial I}{\partial \mu} + a_\lambda \frac{\partial \lambda I}{\partial \lambda} + 4a_\lambda I = \eta - \chi I, \quad (4.2)$$

where  $\eta$  is the emissivity and  $\chi$  is the extinction coefficient. The wavelength is represented by  $\lambda$ . The coefficient are given by

$$a_t = \frac{\gamma}{c}(1 + \beta\mu), \quad (4.3)$$

$$a_r = \gamma(\mu + \beta), \quad (4.4)$$

$$a_\mu = \gamma(1 - \mu^2) \left[ \frac{1 + \beta\mu}{r} - \gamma^2(\mu + \beta) \frac{\partial\beta}{\partial r} \right], \quad (4.5)$$

$$a_\lambda = \gamma \left[ \frac{\beta(1 - \mu^2)}{r} + \gamma^2\mu(\mu + \beta) \frac{\partial\beta}{\partial r} \right]. \quad (4.6)$$

The additional time dependent coefficient is represented by  $a_t$ . The other coefficients have been defined in Hauschildt & Baron (2004), but are given here for convenience. Along the characteristics, the equation 4.2 has the form (Mihalas 1980)

$$\frac{dI_l}{ds} + a_t \frac{\partial I}{\partial t} + a_l \frac{\partial \lambda I}{\partial \lambda} = \eta_l - (\chi_l + 4a_l)I_l, \quad (4.7)$$

where  $ds$  is a line element along a characteristic,  $I_l(s)$  is the specific intensity along the characteristic at point  $s \geq 0$  ( $s = 0$  denotes the beginning of the characteristic). The coefficient  $a_l$  is defined by

$$a_l = \gamma \left[ \frac{\beta(1 - \mu^2)}{r} + \gamma^2\mu(\mu + \beta) \frac{\partial\beta}{\partial r} \right]. \quad (4.8)$$

In Hauschildt & Baron (2004), two methods for the wavelength discretization are presented. For the discretization of the time derivative, both methods are applied in order to solve the time dependent SSRTE.

#### 4.1.1 First discretization of the time derivative

For the first discretization, the method as described in Hauschildt & Baron (2004) and Hauschildt (1992) is used, and the time dependent term has been added to the radiative transfer equation. Thus, the time as well as the wavelength derivative in the SSRTE are discretized with a fully implicit method. Here, the focus lies on the discretizations of the time derivative. All quantities also depend on the wavelength, but for clarity, only the time dependence is written down in the following equations. The discretization of the time dependent term is given by

$$\left. \frac{\partial I}{\partial t} \right|_{t=t_j} = \frac{I_{t_j} - I_{t_{j-1}}}{t_j - t_{j-1}}, \quad (4.9)$$

where  $t_j$  is the new time. Thus, the SSRTE including the time discretization term can be written as

$$\frac{dI}{ds} + a_\lambda \frac{\lambda_l I_{\lambda_l} - \lambda_{l-1} I_{\lambda_{l-1}}}{\lambda_l - \lambda_{l-1}} + a_t \frac{I_{t_j} - I_{t_{j-1}}}{t_j - t_{j-1}} = \eta_{\lambda_l} - (\chi_{\lambda_l} + 4a_\lambda)I, \quad (4.10)$$

where  $I$  is the intensity at wavelength point  $\lambda_l$  and time point  $t_j$ . The optical depth scale along the ray is redefined as

$$d\tau = \left[ \chi + a_\lambda \left( 4 + \frac{\lambda_l}{\lambda_l - \lambda_{l-1}} \right) + \frac{a_t}{\Delta t} \right] ds = \hat{\chi} ds, \quad (4.11)$$

where  $\Delta t = t_j - t_{j-1}$  is the time step. Introducing the source function  $S = \eta/\chi$ , the radiative transfer equation assumes the form

$$\frac{dI}{d\tau} = \frac{\chi}{\hat{\chi}} \left( S + \frac{a_\lambda}{\chi} \frac{\lambda_{l-1}}{\lambda_l - \lambda_{l-1}} I_{\lambda_{l-1}} + \frac{a_t}{\chi} \frac{1}{\Delta t} I_{t_{j-1}} \right) - I \equiv \hat{S} - I, \quad (4.12)$$

where  $\hat{S}$  is the modified source function. Because of the additional time derivative, a modification of the source function and a new definition of the optical depth scale along a ray is used. With this redefinition of the optical depth and the source function, one can now proceed with the formal solution as described in Hauschildt & Baron (2004).

#### 4.1.2 Second discretization of the time derivative

The time derivative has also been implemented into the SSRTE by using the second discretization method described in Hauschildt & Baron (2004). Thus, equation (4.7) of the SSRTE in characteristics form, now including the time dependence, is rewritten to

$$\frac{dI_l}{d\tau} + \frac{a_l}{\hat{\chi}_l} \frac{\partial \lambda I}{\partial \lambda} + \frac{a_t}{\hat{\chi}_l} \frac{\partial I}{\partial t} = \frac{\eta_l}{\hat{\chi}_l} - I, \quad (4.13)$$

with

$$\hat{\chi}_l = \chi_l + 4a_l \quad (4.14)$$

and the definition of the comoving frame (CMF) optical depth along a characteristic

$$d\tau = \hat{\chi}_l ds. \quad (4.15)$$

The equation 4.13 is rewritten to obtain an expression for the formal solution

$$\frac{dI}{d\tau} = \hat{S} + \tilde{S} + \check{S} - I, \quad (4.16)$$

with the newly introduced time dependence source coefficient

$$\check{S} = -\frac{a_t}{\hat{\chi}_l} \frac{\partial I}{\partial t}. \quad (4.17)$$

As defined in Hauschildt & Baron (2004), the other source coefficients are

$$\hat{S} = \frac{\chi}{\hat{\chi}_l} S = \frac{\eta_l}{\hat{\chi}_l} \quad (4.18)$$

and

$$\tilde{S} = -\frac{a_l}{\hat{\chi}} \frac{\partial \lambda I}{\partial \lambda}. \quad (4.19)$$

Including the new time dependence, the following expression for the formal solution is obtained

$$I_{i,l} = I_{i-1,l} \exp(-\Delta\tau_{i-1}) + \delta\hat{I}_{i,l} + \delta\check{I}_{i,l} + \delta\breve{I}_{i,l}, \quad (4.20)$$

where the definition of the time derivative is given by

$$\delta\breve{I}_{i,l} = \check{\alpha}_{i,l}\check{S}_{i-1,l} + \check{\beta}_{i,l}\check{S}_{i,l}. \quad (4.21)$$

As all quantities of the source function are known, the discretizations of the time derivative source functions are given by

$$\check{S}_{i-1,t} = -\frac{a_{i-1,t}}{\hat{\chi}_{i-1,t}} \left( \frac{I_{i-1,t}}{\Delta t} - \frac{I_{i-1,t-1}}{\Delta t} \right) \quad (4.22)$$

and

$$\check{S}_{i,t} = -\frac{a_{i,t}}{\hat{\chi}_{i,t}} \left( \frac{I_{i,t}}{\Delta t} - \frac{I_{i,t-1}}{\Delta t} \right). \quad (4.23)$$

With the new equations (4.16) and (4.17), the formal solution  $\delta\breve{I}_{i,l}$  can be written in the form

$$\delta\breve{I}_{i,t} = \check{\alpha}_{i,t}(p_{i-1,t}I_{i-1,t} - p_{i-1,t-1}I_{i-1,t-1}) + \check{\beta}_{i,t}(p_{i,t}I_{i,t} - p_{i,t-1}I_{i,t-1}), \quad (4.24)$$

where the new coefficients are given by

$$p_{i-1,t} = -\frac{a_{i-1,t}}{\hat{\chi}_{i-1,t}} \frac{1}{\Delta t} = p_{i-1,t-1} \quad (4.25)$$

and

$$p_{i,t} = -\frac{a_{i,t}}{\hat{\chi}_{i,t}} \frac{1}{\Delta t} = p_{i,t-1}. \quad (4.26)$$

The formal solution then assumes the form

$$\begin{aligned} (1 - \check{\beta}_{i,l}p_{i,l} - \check{\beta}_{i,t}p_{i,t})I_{i,l,t} = & (\check{\alpha}p_{i-1,l} + \check{\alpha}p_{i-1,t} + \exp(-\Delta\tau_{i-1}))I_{i-1,l,t} \\ & - \check{\alpha}p_{i-1,l-1}I_{i-1,l-1} - \check{\alpha}p_{i-1,t-1}I_{i-1,t-1} \\ & - \check{\beta}p_{i,l-1}I_{i,l-1} - \check{\beta}p_{i,t-1}I_{i,t-1} + \delta\breve{I}. \end{aligned} \quad (4.27)$$

### 4.1.3 Implementation

Both discretization methods have been implemented into the radiative transfer part of PHOENIX. Like in Hauschildt & Baron (2004), a factor  $\xi = [0, 1]$  has been introduced. To solve the time dependent SSRTE with the first discretization method, this factor has to be  $\xi = 1$ , for the second discretization method, this factor has to be set to  $\xi = 0$ . It is also possible to use a mixed discretization method by varying  $\xi$  over the interval  $[0, 1]$ .

To compute time dependent radiative transfer, all the intensities of the time step before have to be known and, therefore, stored in the memory. Depending on the number of used wavelength points, this requires a few GB. For instance, a calculation of the time dependent SSRTE for 25,000 wavelength points needs 4 GB of memory for the storage of the intensities. But thanks to the parallel implementation of PHOENIX (Hauschildt et al. 1997; Baron & Hauschildt 1998), one can reduce the amount of memory required by each process. By using domain decomposition for the parallelization, the set of all wavelength points is divided into wavelength clusters. Each process works on a particular wavelength cluster. Thus, each process only needs to know the intensities of the previous time step of the wavelength points assigned to its wavelength cluster. This reduces the needed memory per process by a factor equal to the number of used wavelength clusters. Therefore, by using parallel calculations, even high resolution radiative transfer problems can now be computed time dependently.

## 4.2 Test Calculations

For the test of the time dependent SSRTE, a static atmosphere structure is used to see the direct effects of the time dependence of the radiative transfer. That means that the temperatures, radii and densities are all constant in time. As this work is about SNe Ia, a typical SN Ia atmosphere structure was used. The used atmosphere structure is in radiative equilibrium and was obtained with the PHOENIX temperature correction procedure.

In a first test calculation, the results of the two different discretization methods are compared. As a time independent atmosphere structure is used, the results of the time dependent radiative transfer equation should be constant in time and should not differ from the results of the solution of the time independent SSRTE. In a first try, the size of the time step is set to  $10^{-5}$ s. The time dependent SSRTE is solved with the time independent atmosphere structure. With this small time step, the results of the time dependent and time independent SSRTE are the same. The size of the time step is smaller than the radiation time scale. Therefore a huge number of time steps is needed to see an effect of the time dependent radiative transfer. With a larger time step of  $10^5$ s, unexpected fluctuations of the results appear, which are due to the fact that this used time step is bigger than the radiation time scale of the atmosphere. But after a few time steps, the flux result goes back to being constant again. This fluctuations are due to starting the calculation and are nothing physical. The deviation of the resulting flux from the time independent result is less than 0.5%. By changing the value of the time step, one can determine the radiation time scale and, therefore, the optimal time step for a calculation with the time dependent radiative transfer. The result is an optimal time step of  $5 \cdot 10^3$ s. An analytical estimate of the radiation time scale is given below. This value of the time step is used for the other test calculations, where the inner boundary condition

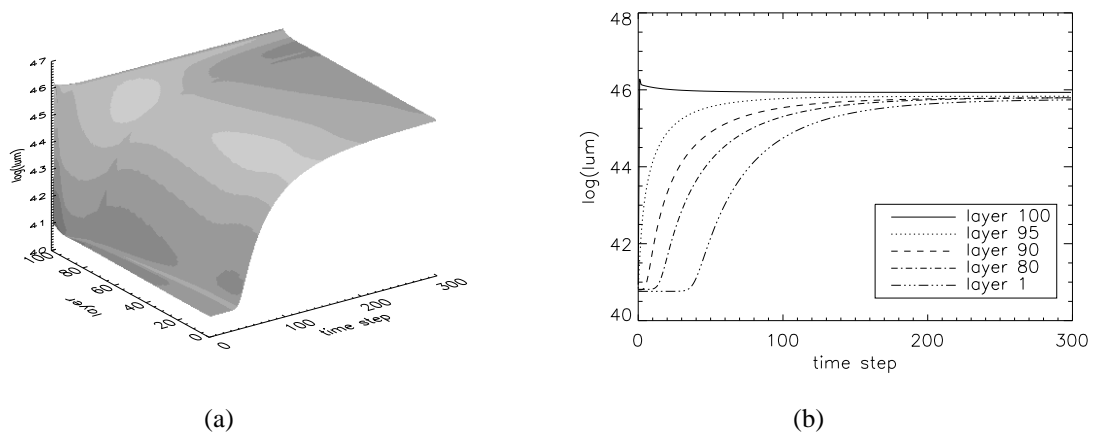


Figure 4.1: Results of a test calculation, where the atmosphere has an additional light source inside, which has been switched on. (a) A surface plot of the luminosity over layer and time step illustrates that the information of the inner boundary condition change needs time to move outwards. (b) A plot of the luminosity in different layers. As one can see, the information is moving through the atmosphere.

is changing. There are also differences between the two discretization methods, which are about in the same range. That means, the solution of the time dependent radiative transfer equation for an atmosphere with a constant structure is the same as for the time independent calculation within an accuracy of 0.5% for long times.

For the next tests, time dependent effects of changes in the radiation field are investigated. To do that, the inner boundary condition for the radiation (the “light bulb”) is changed to initiate a perturbation of the radiation field, which then moves through the atmosphere via the time dependent radiation transport. These tests will be performed for some different perturbations of the inner boundary condition. Note that the atmosphere structure again stays constant.

For the first of these test calculations, an additional light source inside of the atmosphere is switched on. This inner light bulb has a luminosity, which is  $10^5$  times larger than the original value of the inner boundary condition. The time step size used for the calculation is  $5 \cdot 10^3$ s. In figure 4.1(a), the results of the time dependent radiative transfer calculation is shown in a surface plot of the luminosity over layer during the calculated time range. As one can see, the additional luminosity is moving through the atmosphere, and the luminosity is increased everywhere in the atmosphere. This process needs some time. In figure 4.1(b), a plot of the luminosity change in time of a few layers shows this effect clearly. It takes time before the information about the change of the inner boundary condition arrives at the outermost layer. The propagation of the radiation through the atmosphere can also be observed in figure 4.2, where the luminosity of the atmosphere is shown at different points in time. While in the first few time steps the additional radiation is only in the deeper layers, later the whole atmosphere has relaxed to the new inner boundary condition. In figure 4.3, the luminosity of the atmosphere after the last computed time step is shown. In this plot, the results of the two discretization methods are compared. One can see that there are small differences in the

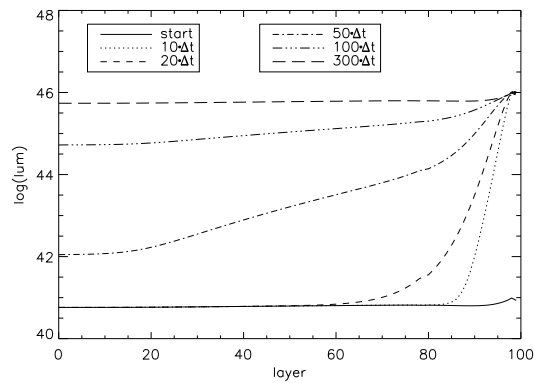


Figure 4.2: Results of an atmosphere, which has an additional light source inside, which is switching on. The luminosity over layer of a few time steps with  $\Delta t = 5 \cdot 10^3$  s is shown here. The information needs time to get to the outer layers.

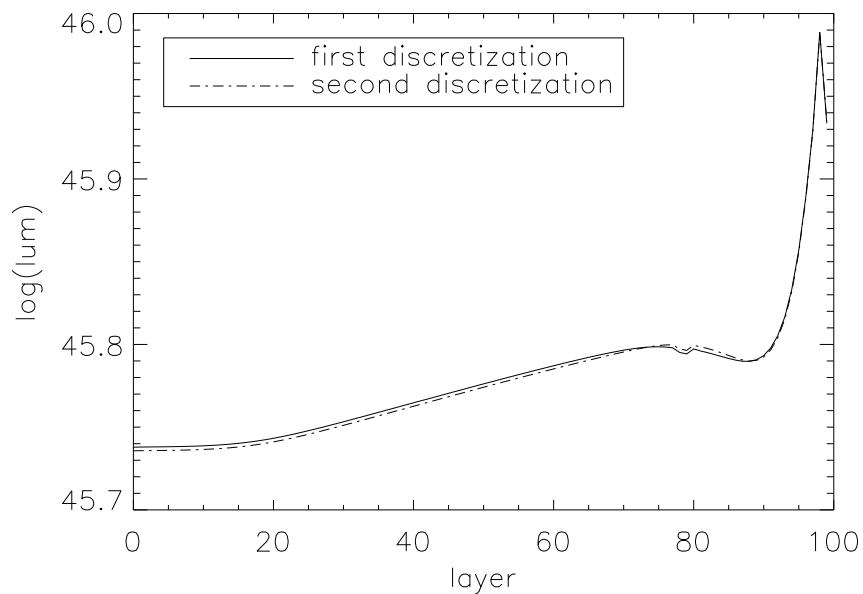


Figure 4.3: The luminosity over layer of the last computed time step. Here the two discretization methods are compared and there is almost no difference in the resulting luminosities between both methods.

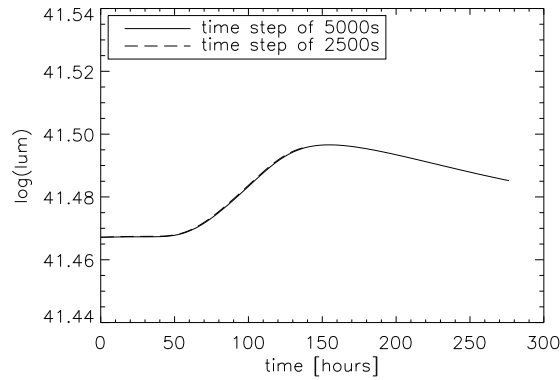


Figure 4.4: Light curve of an atmosphere, where a small perturbation moves through. The two plotted light curves of layer 90 were calculated with different time step sizes. As one can see, the result does not depend on the size of the time step.

luminosities between the two discretization methods. The results of the two discretization methods are the same within 0.5%.

To check the correctness of the resulting time scale, the time scale of the test calculation is compared to the radiation diffusion time scale. Assuming a random-walk process, the mean free path for a photon is given by  $\lambda_p = \frac{1}{\bar{\chi}}$ , where  $\bar{\chi}$  is the mean opacity. For a travel distance  $l$ , the time  $t_p$  a photon needs is given by

$$t_p \approx \frac{1}{3} \frac{l^2}{c \lambda_p} = \frac{1}{3} \frac{l^2}{c} \bar{\chi}, \quad (4.28)$$

where  $c$  is the speed of light (Mihalas & Mihalas 1984). For the mean opacity  $\bar{\chi}$ , the Rosseland mean is used. The mean opacity  $\bar{\chi}$  ranges from  $2 \cdot 10^{-21} \text{cm}^{-1}$  in the outer parts to  $5 \cdot 10^{-13} \text{cm}^{-1}$  in the inner parts of the atmosphere. The distance  $l$  is the thickness of each layer and ranges between  $10^{12} \text{cm}$  and  $6 \cdot 10^{13} \text{cm}$ . The overall travel time is the sum of the travel times of all layer. The result of this calculation is that the diffusion time for a photon through the whole model atmosphere is about  $7 \cdot 10^4 \text{s}$ . As one can see in figure 4.1(b), the time scale of the radiative transfer calculation is approximately 40 time steps, which is in time  $2 \cdot 10^5 \text{s}$ . The assumption of a diffusion through the atmosphere is only valid for optically thick regions. Another problem is the choice of the correct mean opacity. Considering this, the estimate of the time scale is adequate.

Another important test is also to check if the results of the time dependent radiative transfer calculation depends on the size of the time step. This was tested with a model atmosphere that has a small perturbation of the inner light bulb, which is then moving outwards. This setup was calculated with two different time steps. In figure 4.4, the results of the calculation with two different time steps are shown. As one can see, the result does not depend on the size of the time step. The resulting luminosities of both calculations are the same within an accuracy of  $10^{-5}$ .

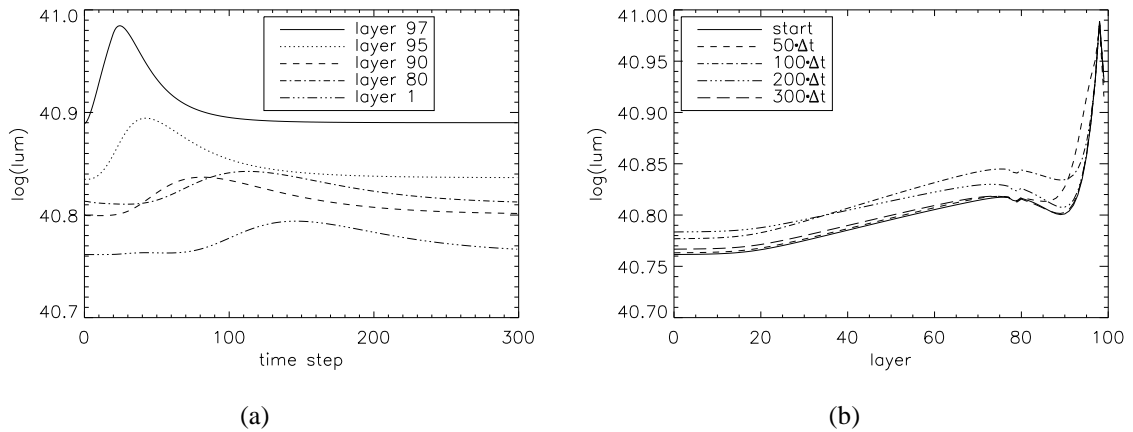


Figure 4.5: Luminosity of different layers for the case of a rectangular shape perturbation originating at the inner boundary and moving through the atmosphere. (a) Luminosity of a few layers over time. As one can see it takes time for the perturbation to move outwards. The shape of the perturbation is also flattening. (b) Luminosity of the atmosphere at a few time points with  $\Delta t = 5 \cdot 10^3 \text{s}$ .

In a further test, the luminosity of the inner light bulb has been increased for a few time steps. The time dependent radiative transfer has been solved to see how this perturbation moves through the model atmosphere. In figure 4.5(a), a plot of the luminosity of a few different layers is shown. One can see that it needs time as the perturbation moves outwards. The shape of the perturbation is changing during that process. It becomes flatter and broadens. In figure 4.5(b), a plot of the luminosity of the atmosphere at different time steps is shown, where one can also see how the perturbation is moving outwards through the model atmosphere.

In a last test, a sinusoidally varying light bulb is put inside of the test model atmosphere. The period of one sine is 100 time steps. In figure 4.6, a surface plot of the luminosity of the atmosphere over layer and time step is shown. After a while, the luminosity of the whole atmosphere varies sinusoidally and steady state is reached. The luminosities in a few different layers are shown in figure 4.7(a). As one can see, the whole atmosphere is varying as a sine. One can also see a phase shift of the sine because of the time required for the radiation field to propagate through the model atmosphere. The phase shift is almost a whole period. The atmosphere has a radius of  $5.1 \cdot 10^{15} \text{cm}$ , and the information of the change of the inner boundary condition needs 100 time steps, which is  $5 \cdot 10^5 \text{s}$ , to get to the outermost layer. Hence, the information of the inner boundary condition change travels with a velocity of 34% of the light speed through the atmosphere. As one can also see, the amplitude of the sine is decreasing as the radiation propagates to the outer parts of the atmosphere. In figure 4.7(b), a plot of the luminosities of the atmosphere at different time steps is shown. Here, one can see that a certain part of the atmosphere has a lower luminosity than the original one, as a different part has a higher luminosity at the same time.

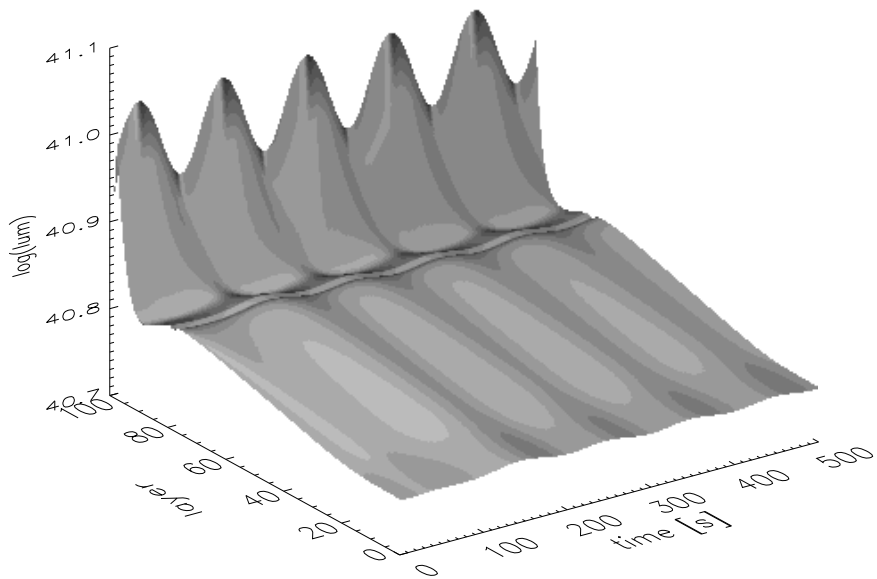


Figure 4.6: This is a surface plot of the luminosity over layer and time step. The light source inside the atmosphere is varying sinusoidally. As one can see, the luminosity of the whole atmosphere is sinusoidally varying. There is a phase shift between the inner light bulb and the emergent flux at the outer layer because the information needs time to move outwards.

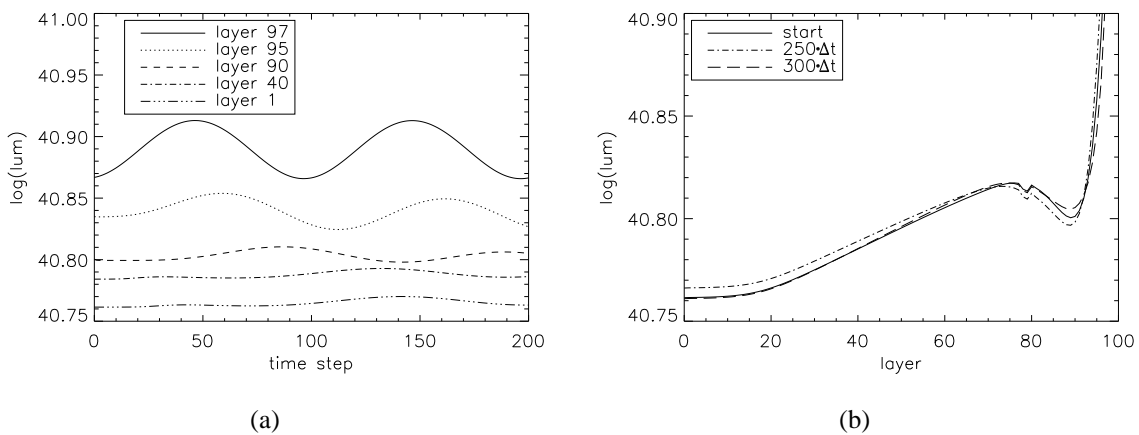


Figure 4.7: Atmosphere with a sinusoidally varying inner boundary condition. (a) Luminosity of a few layers over time. It takes time for the information to move outwards. One can see the phase shift from inner to outer radii, which is about a whole sine. (b) Luminosity over layer at different time steps, and, therefore, different phases of the sine with  $\Delta t = 5 \cdot 10^3$  s

# Chapter 5

## Hydrodynamical solver

In this chapter, the approach to calculate SN Ia light curves is presented. A simple hydrodynamical solver is implemented into the general purpose stellar atmosphere code PHOENIX to keep track of the evolution of an SN Ia atmosphere structure during the free expansion phase. In the hydrodynamical solver, the energy change of the atmosphere per time step is computed. There are three main aspects that have an influence on the energy density of the SN Ia atmosphere. The free expansion changes the densities and radii of the envelope, and the energy deposition by the gamma ray emission of radioactively decaying elements such as  $^{56}\text{Ni}$  powers the light curve. The radiative transfer describes the transport of the deposited energy to other parts of the atmosphere. The temperature structure always changes towards radiative equilibrium.

In the first section, the implementation of the hydrodynamical solver is presented. All contributions to an energy density change of the atmosphere are discussed in detail. The method to compute a new temperature structure of the SN Ia atmosphere is presented. This newly implemented hydrodynamical solver is tested with test calculations, which are presented in the second section. All components of the new hydrodynamical solver are tested for their own to check if each part is working correctly. A more realistic test case, where all contributions to the energy density change are considered, is also discussed.

### 5.1 Hydrodynamical solver

The details of the hydrodynamical solver implementation are presented in this section. The main idea is to compute the energy change of the SN Ia model atmosphere during the free expansion phase. The energy change of the atmosphere is given by equation (96.7) in Mihalas & Mihalas (1984), which is

$$\rho \left[ \frac{de}{dt} + p \frac{d}{dt} \left( \frac{1}{\rho} \right) \right] = \int (c\chi E - 4\pi\eta) + \rho\varepsilon, \quad (5.1)$$

where  $\rho$  is the density and  $p$  the pressure of the material,  $e$  is the internal energy density of the material. The quantities relevant for the radiation field are  $\chi$ , which is the absorption coefficient,  $\eta$  is the emission coefficient, and  $E$  the radiation energy density. All additional energy sources are put in  $\varepsilon$ , such as the energy deposition by gamma ray emission.

Influencing the atmosphere are the free expansion, the energy deposition by gamma ray emission due to the radioactive decay of  $^{56}\text{Ni}$  and  $^{56}\text{Co}$  and the transport of energy by radiation through the atmosphere. All these effects are described in particular in the following

subsections. The main idea of the hydrodynamical solver is to keep track of the energy changes and, therefore, calculate the temperature structure evolution of the atmosphere. In order to save computation time, an adaptive time step scheme, which determines the optimal time step size, is also implemented.

### 5.1.1 Dynamical models

The basis of the approach are the dynamical models, which are already implemented in PHOENIX. In the dynamical model mode, PHOENIX solves the radiative transfer for a given fixed atmosphere structure. This includes a complex density structure as well as non-homogeneous abundances for each layer of the model atmosphere. The temperature structure is computed by an iteration process with a temperature correction procedure to obtain a model atmosphere which is in radiative equilibrium. In case of an SN Ia atmosphere calculation, it is possible to compare synthetic spectra of different explosion models to observed spectra. For instance, spectra obtained with the deflagration or a delayed detonation explosion model structure can be compared, and it might be possible to determine the correct explosion model. Numerous spectra modeling calculations have already been performed by using the dynamical model mode of PHOENIX (Nugent et al. 1997; Lentz et al. 2001b; Baron et al. 2006).

For the new implementation of the hydrodynamical solver, the dynamical model mode is used as the basis. Using this dynamical model mode, the radiative transfer is solved for the fixed SN Ia atmosphere structure of the explosion model used. The hydrodynamical solver then calculates the changes of the atmosphere structure for a certain time step. This includes new radii, densities and the new temperature structure. The radiative transfer can then be calculated with this new atmosphere structure to obtain the resulting radiation field after the next time step. Thus, the hydrodynamical solver changes the atmosphere structure of the dynamical model mode time step by time step. Applying this approach, a whole evolution of an SN Ia atmosphere structure can be calculated. For the atmosphere structure change, all important influences on the atmosphere structure have to be taken into account. These are discussed in the following sections.

### 5.1.2 Gamma ray deposition

The actual thermonuclear burning process of an SN Ia progenitor lasts only a few seconds. After the explosion is over, the atmosphere is in the free expansion phase, during which the atmosphere would just cool down. But observations indicate that something has to cause the rise of the light curve during the free expansion phase. The maximum in the light curve is observed around 20 days after the explosion is already over. Indeed, the light curve of an SN Ia event is powered by an energy release into the atmosphere caused by the radioactive decay of  $^{56}\text{Ni}$  and its also radioactive decay product  $^{56}\text{Co}$ . Therefore, this energy deposition has a strong influence on the energy change of the SN Ia atmosphere structure thus the energy deposition because of the radioactive decay has to be taken into account for the calculation of the SN Ia atmosphere evolution.

The dynamical model mode of PHOENIX already includes the abundances of elements present in an SN Ia atmosphere for each layer, but it so far does not supply the abundances

of particular isotopes. The results of the explosion model calculation already provide the abundances of the isotopes that are present in an SN Ia atmosphere. Due to the radioactive decay, the abundances of  $^{56}\text{Ni}$ ,  $^{56}\text{Co}$  and  $^{56}\text{Fe}$  change during the evolution of the SN Ia atmosphere. Therefore, the abundances of the isotopes of nickel, cobalt and iron have been newly implemented into PHOENIX. It is now possible to keep track of the abundance changes and the resulting energy deposition by gamma ray emission due to the radioactive decay. The abundances of the other elements are assumed to do not change during the free expansion phase of an SN Ia event.

In the beginning the SN Ia atmosphere consists, as a result of the explosion, of a huge amount of  $^{56}\text{Ni}$ , which decays to  $^{56}\text{Co}$  by electron capture with an half life of 6.077 days. The  $^{56}\text{Co}$  then decays by electron capture to  $^{56}\text{Fe}$  with an half life of 77.27 days. The produced  $^{56}\text{Fe}$  is stable and the atmosphere is, therefore, enriched with iron during the evolution of an SN Ia atmosphere. The abundances of the radioactive isotopes change with an exponential law of radioactive decay in time, which is in case of the  $^{56}\text{Ni}$  given by

$$\text{Ni}(t) = \text{Ni}(t = 0\text{s}) \cdot e^{-\frac{t}{\tau_{\text{Ni}}}}, \quad (5.2)$$

where  $\text{Ni}(t)$  is the amount of  $^{56}\text{Ni}$  at a point in time  $t$  after the explosion, and  $\text{Ni}(t = 0\text{s})$  is the initial amount of the nickel isotope 56. The half life is represented by  $\tau_{\text{Ni}}$ . This exponential law is the same for the decay of cobalt. But it also has to be taken into account that new cobalt is produced because of the decay of nickel. Including both effects, the abundance of  $^{56}\text{Co}$  is given by

$$\text{Co}(t) = \text{Ni}(t = 0\text{s}) \cdot \frac{\tau_{\text{Co}}}{\tau_{\text{Ni}} - \tau_{\text{Co}}} \left( e^{-\frac{t}{\tau_{\text{Ni}}}} - e^{-\frac{t}{\tau_{\text{Co}}}} \right) + \text{Co}(t = 0\text{s}) \cdot e^{-\frac{t}{\tau_{\text{Co}}}}, \quad (5.3)$$

where  $\text{Co}(t)$  is the amount of  $^{56}\text{Co}$  at a point in time  $t$ ,  $\tau_{\text{Co}}$  is the half life and  $\text{Co}(t = 0\text{s})$  the initial amount of the cobalt isotope 56. The abundance of the stable  $^{56}\text{Fe}$  increases due to decay of  $^{56}\text{Co}$ , but it also has to be taken into account the changing abundance of  $^{56}\text{Co}$ , because new  $^{56}\text{Co}$  is produced because of the decay of  $^{56}\text{Ni}$ . The amount of  $^{56}\text{Fe}$  is given by

$$\begin{aligned} \text{Fe}(t) = \text{Ni}(t = 0\text{s}) \cdot \left( 1 + \frac{\tau_{\text{Co}}}{\tau_{\text{Ni}} - \tau_{\text{Co}}} e^{-\frac{t}{\tau_{\text{Co}}}} - \frac{\tau_{\text{Ni}}}{\tau_{\text{Ni}} - \tau_{\text{Co}}} e^{-\frac{t}{\tau_{\text{Ni}}}} \right) \\ + \text{Co}(t = 0\text{s}) \cdot \left( 1 - e^{-\frac{t}{\tau_{\text{Co}}}} \right) + \text{Fe}(t = 0\text{s}), \end{aligned} \quad (5.4)$$

where  $\text{Fe}(t)$  the amount of  $^{56}\text{Fe}$  at the point in time  $t$ , and  $\text{Fe}(t = 0\text{s})$  is the initial amount. Applying the equations 5.2, 5.3 and 5.4, all abundances of the SN Ia atmosphere can be determined for each point in time.

To illustrate the changing abundances, figure 5.1 shows the abundance changes in time of  $^{56}\text{Ni}$ ,  $^{56}\text{Co}$  and  $^{56}\text{Fe}$ . At  $t = 0\text{s}$ , the initial abundances for this test case are that only  $^{56}\text{Co}$  is present. There exist neither iron nor cobalt in this test scenario. The nickel is then decaying in time to cobalt, leading to a decreasing nickel abundance. Hence, the cobalt abundance increases and has its peak at around 25 days, because the produced cobalt eventually decays to iron. The production of iron takes longer because the half life of cobalt is higher than the one of nickel.

The energy deposition due to the gamma ray emission of these isotopes needs to be computed by a radiative transfer solver for the  $\gamma$ -rays. In this work, the gamma ray deposition

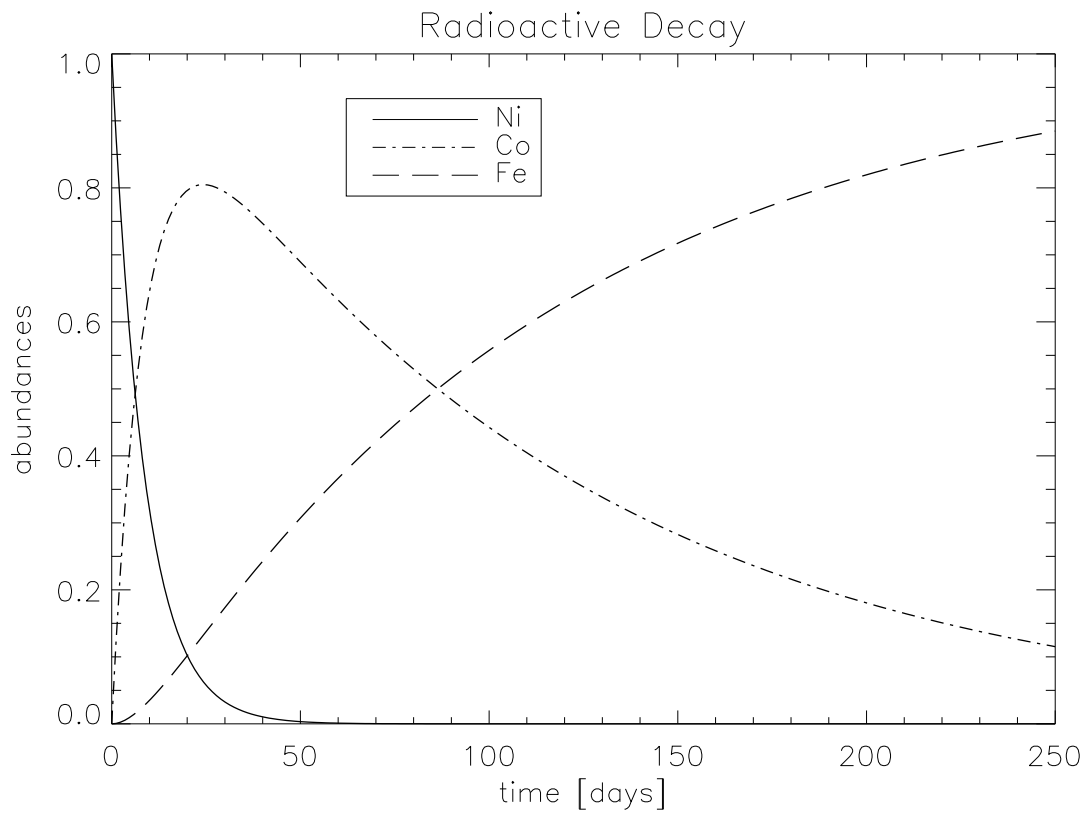


Figure 5.1: Time dependent abundances of  $^{56}\text{Ni}$ ,  $^{56}\text{Co}$  and  $^{56}\text{Fe}$ . The decay of  $^{56}\text{Ni}$  causes the abundance of  $^{56}\text{Co}$  to rise to a peak at around 25 days. The  $^{56}\text{Co}$  decays to  $^{56}\text{Fe}$ , which abundances increases.

is solved with the assumption of a gray atmosphere for the  $\gamma$ -rays. Jeffery (1998) did a detailed study of the  $\gamma$ -ray deposition and pointed out that this is an adequate approach to calculate  $\gamma$ -ray deposition in SN Ia atmospheres. In the decay of a  $^{56}\text{Ni}$  nucleus, a gamma photon is emitted with an energy of 2.136 MeV. The  $^{56}\text{Co}$  nucleus decays to an  $^{56}\text{Fe}$  nucleus and emits a gamma photon, which has an energy of 4.566 MeV. In the decay of  $^{56}\text{Co}$  about 19% of the energy is released by positrons. The positrons are assumed to be locally trapped. They annihilate by emitting two photons with an energy of 512 keV, which has to be taken into account for the energy deposition calculation. The opacity is considered to be constant and a pure absorption opacity, meaning that no scattering is assumed. As in Jeffery (1998),  $\kappa_\gamma = 0.06\text{cm}^2\text{g}^{-1}$  was chosen as the opacity. The energy deposition into the atmosphere per time is given by

$$\varepsilon = 4\pi \frac{\chi}{\rho} J, \quad (5.5)$$

where  $J$  is the mean intensity, which has been obtained by solving the gray radiative transfer for the  $\gamma$ -rays. Therefore, with help of the gray radiative transfer part of PHOENIX, an energy input for every layer of the SN Ia atmosphere is obtained. This obtained energy deposition has to be taken into account for the calculation of the overall energy change.

### 5.1.3 Absorption and emission

The last aspect of the SN Ia atmosphere evolution calculation with the hydrodynamical solver is the determination of the transport of energy by radiation through the atmosphere. One has to solve the complex radiative transfer problem as accurately as possible to obtain the radiation energy change of the atmosphere. For the time evolution calculation, this term is important, because it lets the energy move through the atmosphere, distributing the deposited energy of the gamma ray emission everywhere in the atmosphere. The energy change due to radiation is part of equation 5.1. The term of the change of the energy density of the material by the absorption and emission of radiation is given by

$$Q = \int (c\chi E - 4\pi\eta), \quad (5.6)$$

where  $E$  is the energy of the radiation field,  $\chi$  is the extinction coefficient and  $\eta$  the emissivity. This equation can be rewritten to

$$Q = \int \chi_\lambda (J_\lambda - S_\lambda) d\lambda, \quad (5.7)$$

with  $S_\lambda = \eta_\lambda / \chi_\lambda$  being the source function,  $J_\lambda$  the mean intensity and  $\lambda$  the wavelength. One has now to solve the radiative transfer equation to obtain these quantities. This energy change can be obtained by using the complex radiative transfer part of PHOENIX. The solution of the detailed radiative transfer solver delivers also the interaction of the radiation with the material and, therefore, gives the net amount of energy that is absorbed or emitted by the gas. The radiative transfer solver is also the time consuming part of the calculation of a whole SN Ia light curve, as the SSRTE has to be solved for each point in time. The radiative

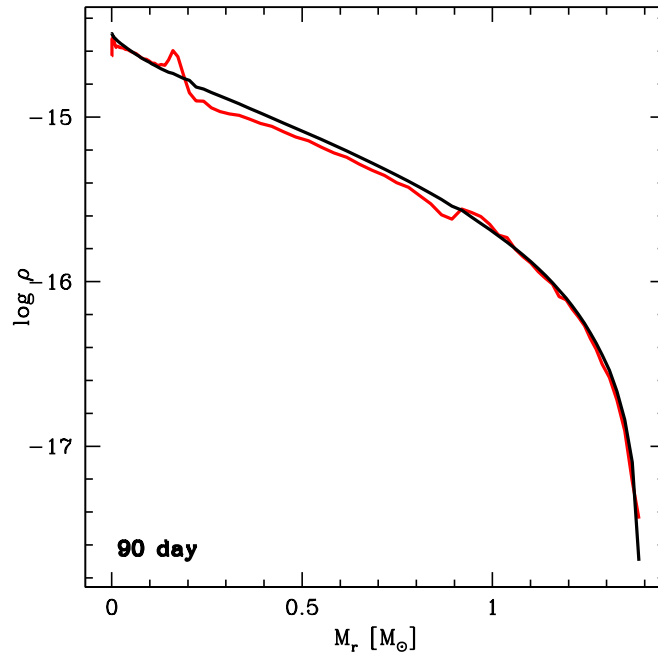


Figure 5.2: Density profile of a more complex model (gray line) and one with assuming homologous expansion (black line) at day 90 (Woosley et al. 2007).

transfer is solved by assuming a non-gray atmosphere with numerous wavelength points. As the opacity is strongly depending on the wavelength the non-gray approach is essential for the radiative transfer. About a few thousand wavelength points are used in a typical SN Ia model atmosphere calculation. By reducing the number of wavelength points, the light curve calculation can be made faster, but this certainly comes at cost of the accuracy. In case of an SN Ia atmosphere, the line opacity is very important and has to be taken into account. Therefore, the atomic lines database of Kurucz & Bell (1995, 2006) is used. Even more computation time for the radiative transfer is needed if an atmosphere in NLTE is assumed.

#### 5.1.4 Expansion

After the explosion is over, the envelope of the SN Ia is expanding. The expansion is assumed to be a homologous expansion, meaning that the expansion velocities of each part of the atmosphere do not vary in time. However, the energy release by the decay of  $^{56}\text{Ni}$  can influence the dynamics of the expansion (Pinto & Eastman 2000). Woosley et al. (2007) compared a study following this energy release to the results from assuming homologous expansion. Figure 5.2, which is Figure 2 in their paper, shows the deviation and density variations can be as large as 10%. However, this is probably an upper limit due to the simple burning parametrization used in that study. Ultimately, when the deflagration to detonation transition is understood it will be important to revisit this issue, and replace 1-D calculations with full 3-D hydrodynamical calculations, that include the effects of clumps as well as nickel bubble expansion. For now the accuracy of homologous expansion should be adequate, given the other uncertainties in the problem.

In the dynamical models, each layer has a constant expansion velocity to simulate a freely expanding envelope. During the hydrodynamical evolution calculation, the expansion velocity assigned to a layer stays constant. Therefore, the new radii and density for a new point in time can be computed quite simply. The new radius  $r_{new}$  of a layer is determined by

$$r_{new} = u \cdot \Delta t + r_{old}, \quad (5.8)$$

for a time step size of  $\Delta t$ , while the layer is expanding with the velocity  $u$ . The radius before the new time step is  $r_{old}$ . With the same assumption of homologous expansion, the new density  $\rho_{new}$  of a layer after the new time step is determined by

$$\rho_{new} = \rho_{old} \cdot \left( \frac{r_{old}}{r_{new}} \right)^3, \quad (5.9)$$

where  $\rho_{old}$  is the density of the previous point in time. With the new radii and densities, it is now possible to calculate the energy change due to the free expansion of the atmosphere. The expansion of the supernova envelope is assumed to be an adiabatic process. Therefore, the work  $W$  done by this process is given by

$$W = -p \frac{d}{dt} \left( \frac{1}{\rho} \right), \quad (5.10)$$

where  $p$  is the pressure of the material. For a discrete time step, the internal energy density change of the atmosphere is given by

$$W = -p \left( \frac{1}{\rho_{new}} - \frac{1}{\rho_{old}} \right). \quad (5.11)$$

This result represents the change of the internal energy density because of the adiabatic expansion. As can be seen, the adiabatic expansion decreases the energy density of the atmosphere. Therefore, the SN Ia envelope cools down.

### 5.1.5 Overall energy change

The energy changes because of the free adiabatic expansion, the gamma ray emission and the energy transport have been discussed in detail, and now all the required quantities to calculate the overall energy density change of the SN Ia atmosphere during a certain time step are available. The direct change of the energy density of the material considering the expansion, the absorption and emission of radiation and energy deposition by gamma ray emission is given by equation (96.7) in Mihalas & Mihalas (1984), which is

$$\rho \left[ \frac{de}{dt} + p \frac{d}{dt} \left( \frac{1}{\rho} \right) \right] = \int (c\chi E - 4\pi\eta) + \rho\epsilon, \quad (5.12)$$

where  $\rho$  is the density and  $p$  the pressure of the material,  $e$  is the internal energy density of the material. The quantities relevant for the radiation field are  $\chi$ , which is the absorption coefficient,  $\eta$  is the emission coefficient, and  $E$  the radiation energy density. All additional

energy sources are put in  $\varepsilon$ , such as the energy deposition by gamma ray emission. The energy change in time is given by

$$\frac{de}{dt} = -p \frac{d}{dt} \left( \frac{1}{\rho} \right) + \frac{4\pi}{\rho} \int \chi(J - S) d\lambda + \varepsilon. \quad (5.13)$$

Rewriting this equation, the new energy density  $e_2$  after a discrete time step  $\Delta t$  can be computed by

$$e_2 = e_1 - p \left( \frac{1}{\rho_2} - \frac{1}{\rho_1} \right) + \frac{4\pi}{\rho} \Delta t \int \chi(J - S) d\lambda + \varepsilon \Delta t, \quad (5.14)$$

where  $e_1$  is the energy density of the material at the time step before. Thus, the new energy density is calculated with an explicit method. All the details of these contributing terms have been discussed in detail in the previous sections. With the new energy density of the material being known, it has now to be determined what the new temperature of each layer at the next time step is.

The internal energy density of the material  $e_{trans}$ , which is the energy of the translating particles without ionization and excitation, is given by

$$e_{trans} = \frac{3}{2} \frac{p}{\rho} = \frac{3}{2} \frac{R}{m_u} T, \quad (5.15)$$

with the mean molecular weight  $m_u$  and the universal gas constant  $R$ .  $T$  stands for the temperature of the material. This equation of the energy density could now be used to determine the new temperature at the next time step point.

During the first phase of the SN Ia atmosphere evolution, the material of the atmosphere is hot and, therefore, highly ionized. The energy change due to ionization and excitation changes of the atoms present in the SN Ia atmosphere cannot be neglected. PHOENIX already solves the equation of state (EOS), where all the excitation and ionization stages of the present atoms and molecules are included. Using the EOS, the overall energy density of the material can be obtained by the sum of the ionization energy  $e_{ions}$  and the translational energy  $e_{trans}$

$$e = e_{trans} + e_{ions}. \quad (5.16)$$

Hence, the energy density change of the material goes into a change of the translational energy and the ionizational energy, which both depend on the temperature. Therefore, the new temperature has to be obtained by an iteration scheme, which is described in the following. The matter density at the next point in time is determined by homologous expansion. A first temperature guess is used, and the EOS is solved to obtain the ionizational energy density. Combined with the translational energy density, the overall energy density is computed. This is checked against the target energy density, which has been obtained by equation 5.14. If the obtained energy density is not correct, a new temperature guess is made. This new temperature guess is obtained by assuming a linear dependence of the energy density and temperature. The current temperature guess is iterated to the target energy density. It takes just 5 to 10 iteration steps to determine the new temperature. If the EOS delivers the correct target energy density, the new temperature of the next time step has been found. The accuracy of the energy density iterations is set to  $10^{-5}$ .

This determination of the new temperature has to be done for every layer. As the calculation of the new temperature of one layer is independent from the other layers, this calculation can be easily parallelized. The calculations of the new temperatures of the layers are distributed among all processes. The EOS has to be solved a few times for each temperature determination per layer, which can cost a few seconds without using the parallelization. For the calculation of a whole SN Ia light curve, a few thousand time steps are needed. Therefore, the parallelized calculation of the new temperatures saves computation time. For instance, the calculation of all new temperatures for all layers needs about 10s to 15s, if only one process is used. With a parallel calculation by using 32 processes, the calculation time can be reduced to under one second.

### 5.1.6 Adaptive time step procedure

The typical time scale for the hydrodynamical changes in the SN Ia atmosphere will change during the evolution of the light curve. In order to save computation time, the light curves have to be calculated with the optimal time step size for each phase of the light curve evolution. Therefore, an adaptive time step routine has been implemented to determine the optimal time step size for the current time step.

The energy change  $\Delta e$  of the energy of the material  $e$  may be approximated by

$$\Delta e = x \cdot e = \Delta t \cdot (Q + \varepsilon), \quad (5.17)$$

where  $Q$  is the energy change of the interaction with the radiation, and  $\varepsilon$  is the energy deposition by the gamma ray emission. The energy change due to the expansion is ignored in this case. On the one hand, this energy change depends on the new matter density after the time step, which is unknown because it depends on the size of the time step itself. Furthermore, the energy change because of the expansion is small compared to the changes caused by the energy transport and the energy deposition by gamma rays. The idea of the adaptive time step procedure is to limit the energy change to a prescribed amount of the energy of the material. Thus, rewriting equation 5.17, the time step size  $\Delta t$  for the current time step for each layer can be obtained by

$$\Delta t = \frac{e}{Q + \varepsilon} \cdot x, \quad (5.18)$$

where  $x$  is the introduced limiting energy change factor. The factor  $x$  ranges between  $x_{min}$  and  $x_{max}$ , which mark the largest and smallest allowed energy change. These are input parameters for the adaptive time step procedure. The time step size is calculated for every layer, and the minimum time step size of all layers is used for the hydrodynamical solver.

Each time the adaptive time step procedure is called, it checks if the energy changes of the time step before were too big or could have been bigger. If the minimum time step size is in a different layer, the same value of  $x$  is kept for the next time step. If the minimum is in the same layer and the sign of the energy change does not change, the previous time step might have been too small. Thus, the factor  $x$  is increased for the following time step. If the sign changes, the last time step might have been too large, therefore, the factor  $x$  is decreased. This means that for each time step, the allowed energy change is adapted and the factor  $x$  is updated to get the optimal time step during the whole evolution of the SN Ia atmosphere.

### 5.1.7 Iteration scheme

All parts of the hydrodynamical solver have been presented and discussed in detail. The following scheme is applied in order to calculate a new time step for the evolution of an SN Ia atmosphere. For the first time step, a initial structure has to be assumed. The densities, radii and expansion velocities are given by the used explosion model. For the start, a temperature structure obtained with the PHOENIX temperature correction procedure can be used. The first step of each time step calculation is to obtain the solution of the radiative transfer equation for the given structure to obtain the quantities for the calculation of the energy change due to absorption or emission of radiation. In the next step, the energy deposition due to gamma ray emission from radioactive decay is calculated. This also involves an update of the abundances of the nickel, cobalt and iron isotope 56. The adaptive time step procedure then determines the size of the current time step and updates the factor  $x$ . With this determined time step, the homologous expansion is calculated, which leads to a new density and radius for each layer for the next point in time. All these new quantities are then used to calculate the new energy density of the material by using the equation 5.14. The energy density change leads to a new temperature structure of the SN Ia atmosphere. With this new atmosphere structure with new radii, densities and temperatures, the next time step can be calculated, and a whole evolution of an SN Ia atmosphere structure can be obtained.

### 5.1.8 First approach

Here, a first unsuccessful approach to the calculation of SN Ia light curves is discussed briefly. See the appendix A for a more detailed description of the alternative hydrodynamical solver. The main idea was to check the overall energy conservation of the SN Ia model atmosphere. An overall energy change of the atmosphere is given by equation (96.15) in Mihalas & Mihalas (1984), which is

$$\frac{D}{Dt}E = -\frac{\partial}{\partial M_r} \{4\pi r^2 [u(p + P_0) + F_0]\} + \varepsilon, \quad (5.19)$$

where  $F_0$  is the radiative flux,  $P_0$  the radiation pressure and  $M_r$  the mass inside of a radius  $r$  of a layer. This energy density change includes a change of the material energy density and the radiation energy density. The main problem of this approach was that only a total change of the energy density can be determined. This total energy change includes a change in both material and radiation energy density. This means, a temperature iteration has to be performed in order to obtain the new temperature structure of the material for the next time step. This required more computation time than the alternative approach presented in this work. Test calculations showed that the first approach for the hydrodynamical solver did work, however the approach presented so far turned out to be more successfully and faster. Therefore, this first approach was not pursued further.

## 5.2 Test calculations

All new implemented processes of the simple hydrodynamical solver have to be tested. For the test atmosphere, the atmosphere structure and abundances of the W7 deflagration model

are used. The atmosphere structure is expanded to a point in time of 10 days after the explosion. The densities and radii are determined by the free homologous expansion and can be computed easily. To perform the test calculations, an initial temperature structure is obtained with the PHOENIX temperature correction procedure. With this initial atmosphere structure, the hydrodynamical solver is applied for different test cases. All contributions to the energy change are tested separately. In the following, all test calculations and the results obtained are presented.

### 5.2.1 Energy transport

In this section, the energy transport through the atmosphere is tested. The hydrodynamical solver is only considering an energy change caused by emission and absorption of radiation, where to the result of the radiative transfer equation is needed. All other influences are neglected. As a first test, the initial temperature structure changes if the hydrodynamical solver is working on the SN Ia atmosphere. As the initial atmosphere structure is already in radiative equilibrium, the hydrodynamical solver should not change the temperature structure significantly, because it also pushes the atmosphere towards a radiative equilibrium state.

In figure 5.3, a comparison of the temperature structure of the hydrodynamical solver to the result of the temperature correction procedure is shown. The differences in the temperature structure are for most layers less than 1%. But as can be seen in figure 5.3, the temperature differences of the inner layers are clearly higher. These differences arise in the temperature correction result as it shows a spike in the temperature structure. This may have been emerged due to the boundary condition in the temperature correction. Hence, the resulting temperature structure obtained with the hydrodynamical solver is more accurate. Here, the temperature structure is smooth. In order to obtain an atmosphere in radiative equilibrium, the energy transport part of the hydrodynamical solver can be used instead of the temperature correction procedure. The main problem is that about a few hundred time steps are needed to obtain the resulting atmosphere structure in radiative equilibrium, while the temperature correction needs fewer iteration steps and is, therefore, significantly faster.

For the next tests, the temperature of the innermost layer is changed in order to get an energy perturbation, which moves through the atmosphere via the energy transport. Numerous different perturbations can be put into the inner part of the atmosphere to test the energy transport part of the hydrodynamical solver. Whatever the perturbation of the inner boundary condition is, the temperature structure is always expected to relax to the new conditions and move back to be in radiative equilibrium. A few test cases with perturbations of the inner boundary condition are presented in the following.

For the first of these test calculations, the temperature of the innermost layer is increased. The expectation is that this additional radiation energy is moving through the atmosphere. The temperature should increase everywhere, and the atmosphere adapts to the new inner boundary condition, until it is again in the radiative equilibrium state. In figure 5.4, the results of this test calculation are presented. A plot of the observed luminosity is shown in figure 5.4(a). The luminosity is increasing, as the temperature of the atmosphere increases because of the hotter inner boundary condition. One can also see that it takes some time, un-

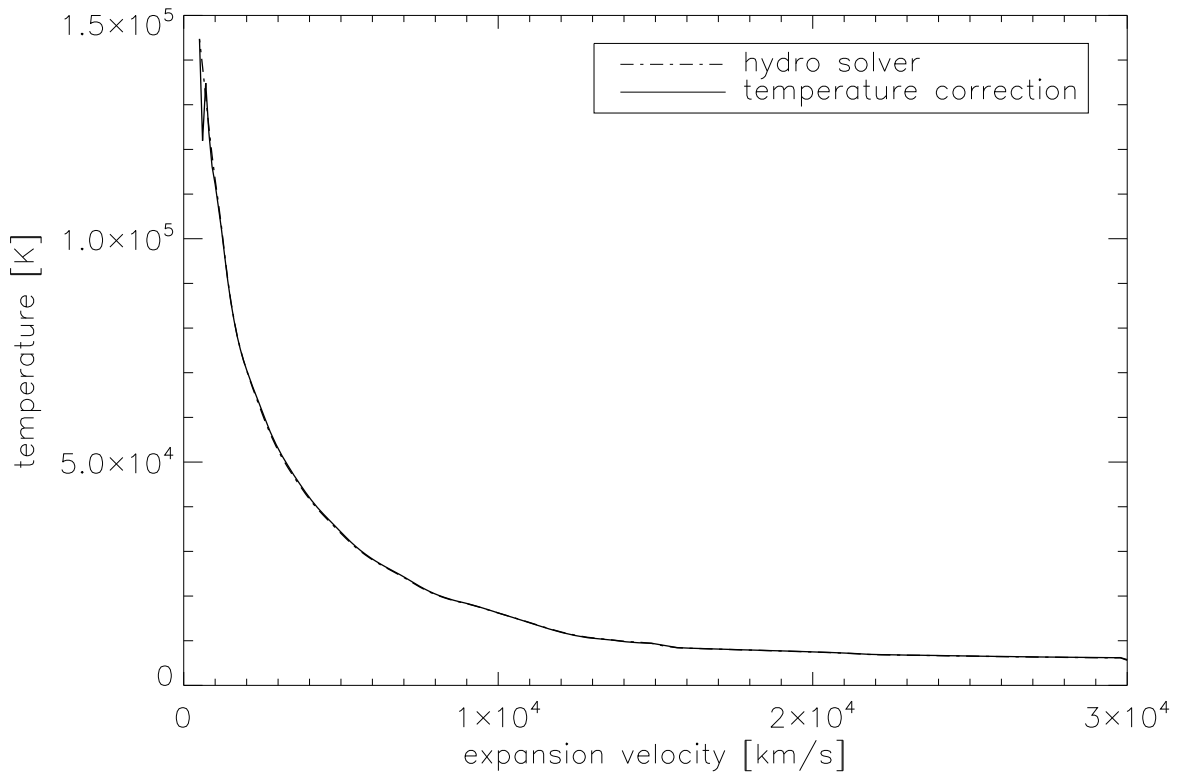


Figure 5.3: The temperature structures obtained with the hydrodynamical solver and the PHOENIX temperature correction are compared in this plot. Both atmospheres are in radiative equilibrium, and therefore the resulting temperature structures should be the same. The differences in the temperature are less than 1%, except for some inner layers.

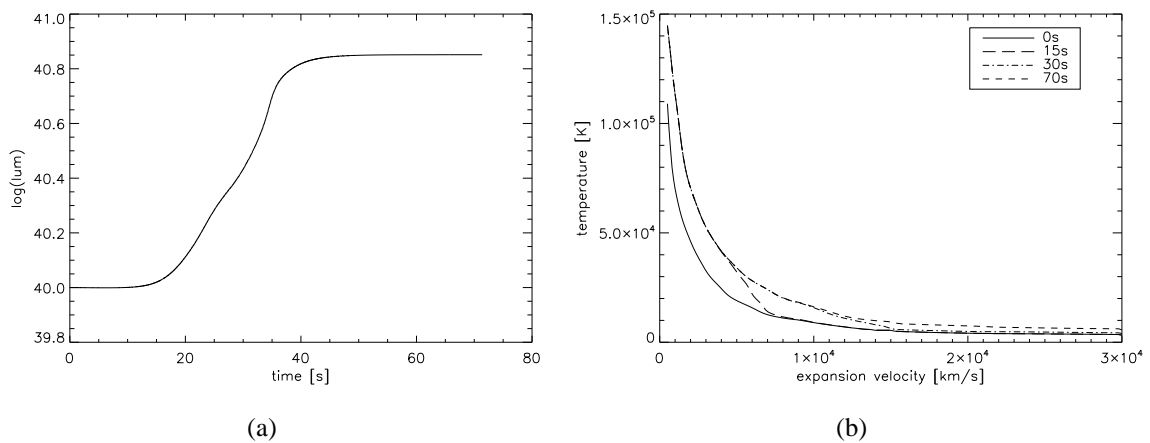


Figure 5.4: Result of a test calculation with an atmosphere, where the inner layer is heated. This additional energy moves through the atmosphere. (a) The increasing observed luminosity of the outer layer is shown. (b) The temperature structure at different points in time.

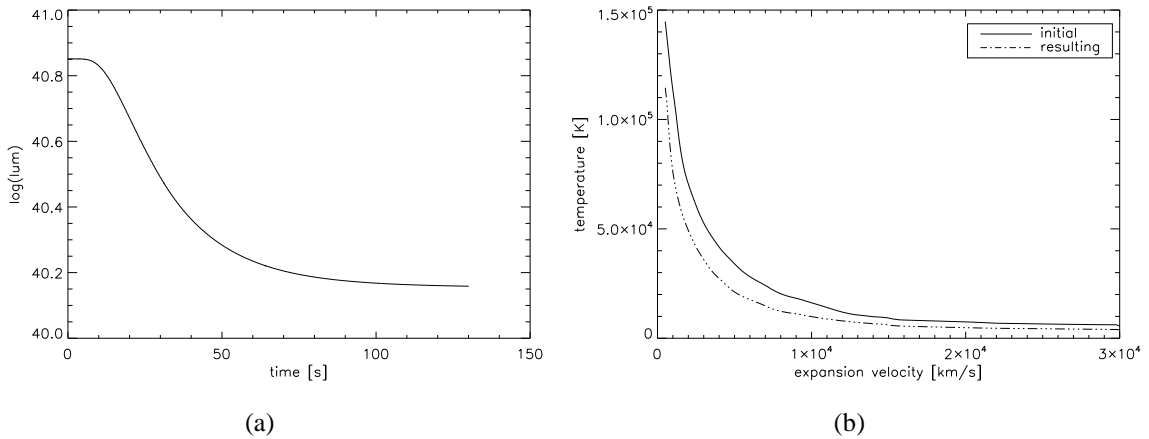


Figure 5.5: Test calculation with an atmosphere, where the innermost layer is set to a lower temperature. (a) The decreasing observed luminosity is shown. The cooled inner part of the atmosphere moves through the atmosphere. (b) The temperature structure on its way to radiative equilibrium is shown here.

til the additional energy gets to the outer part of the atmosphere and is seen by the observer. The temperature of the atmosphere is increasing everywhere, until the atmosphere is again in radiative equilibrium. The initial and final temperature structure are presented in figure 5.4(b), where the increased temperature structure of the atmosphere that has an increased temperature as inner boundary condition are compared.

For the next test, the temperature of the innermost layer is set to a significantly lower temperature. This cooler inner condition leads to a cooling of the whole atmosphere, as it moves back to the radiative equilibrium state. The results of this calculation are presented in figure 5.5. The decreasing observed luminosity is shown in figure 5.5(a). Again, it can be seen that it needs some time before the energy reaches the outer layers of the model atmosphere, and the atmosphere structure has adapted to the new inner boundary condition. The resulting cooler atmosphere structure is shown in figure 5.5(b). The atmosphere relaxes to the changed inner condition and assumes a radiative equilibrium temperature structure.

As the hydrodynamical solver works for changed but then fixed inner condition, now a time dependent temperature of the innermost layer is considered. Thus, for a last test of the energy transport, the temperature of the innermost layer is varying as a sine in time. The time step size is set to a constant value of  $2 \cdot 10^{-2}$ s to have a high time resolution for a whole period of the sine, which takes 400 time steps. Hence, a whole period of the sine needs 8s. The amplitude of the sine of the inner layer is set to 20% of its initial temperature. This perturbation moves through the whole atmosphere and is expected to make the temperature of the whole atmosphere varying as a sine. A surface plot of the temperature is shown in figure 5.6. As can be seen, the temperature of the whole atmosphere is varying periodically. It again takes time before the information about the sinusoidally varying inner temperature reaches the outer layers of the model atmosphere. This becomes apparent as a phase shift in the sine. A plot of the temperature structure at different points in time is shown in figure

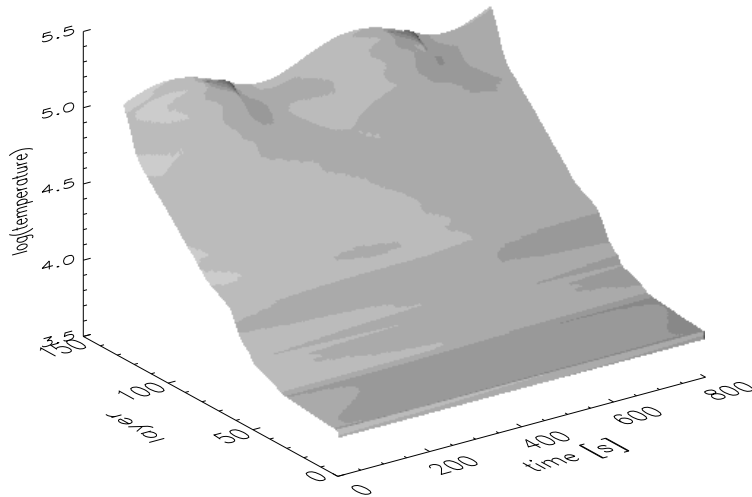


Figure 5.6: The temperature of the innermost layer is varying with a sine in time. This surface plot shows that the whole atmosphere is after some time varying as a sine. This propagation through the atmosphere needs also some time, which leads to a phase shift of the sine.

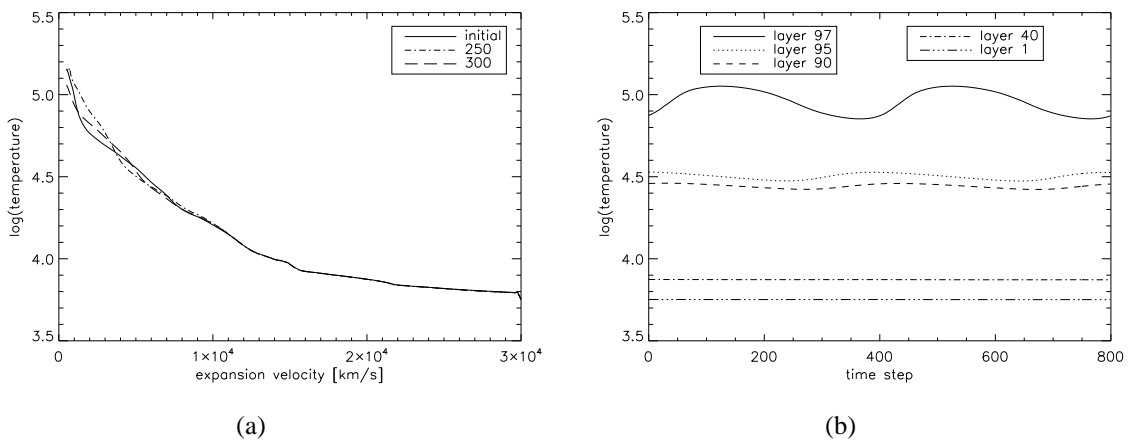


Figure 5.7: Atmosphere with a sinusoidally varying inner temperature. (a) Temperature structure of a few points in time. This perturbation moves through the whole atmosphere, making it varying as sine everywhere. (b) The temperature of a few layers vary in time and have a sinusoidally shape.

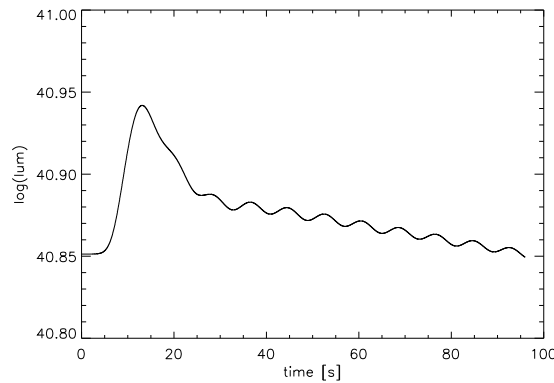


Figure 5.8: Luminosity of the sinusoidally varying atmosphere seen by an observer. After an initial rise, the luminosity is varying with a sine that reflects the sinusoidally varying temperature structure.

5.7(a). One can see the varying temperatures in time. The temperature of a few layers over time is plotted in figure 5.7(b). As it can be seen, the temperature of every layer is varying periodically. The shape is not a sine, but it looks similar. The rising occurs faster than the decline. The deviation may be due to the radiative transfer. It takes time, until the temperature change has moved through the atmosphere. The phase shift is about 200 time steps. The varying luminosity is plotted in figure 5.8. As can be seen, the observed luminosity is varying as a sine, after some initial disturbance.

All the tests indicate that the energy transport part of the hydrodynamical solver works properly. It moves the temperature structure of an atmosphere towards radiative equilibrium. If disturbed, the temperature structure also adapts to the changed inner boundary conditions of the innermost layer. A radiative equilibrium temperature structure obtained with the hydrodynamical solver is almost the same as one obtained with the temperature correction procedure.

### 5.2.2 Expansion

In a next test calculation, the expansion part of the hydrodynamical solver is checked. Thus, the only energy change considered is the adiabatic cooling because of the free expansion of the SN Ia atmosphere. The energy deposition by gamma rays or an energy change because of the energy transport is disabled. For this test case, the expectation is that the atmosphere should just cool down, so the temperature of the atmosphere and the observed luminosity should be decreasing.

In figure 5.9, the results of the free expansion test calculation are presented. The observed luminosity is plotted in figure 5.9(a). As can be seen, the observed luminosity of the SN Ia atmosphere is decreasing. The temperature structure of the first and the last time step is plotted in figure 5.9(b). The adiabatic expansion has cooled the atmosphere everywhere, and the new temperature is now significantly lower.

Another way to test if the adiabatic expansion is computed correctly in the hydrodynamical solver is to calculate the entropy change of the atmosphere. As no energy is moving

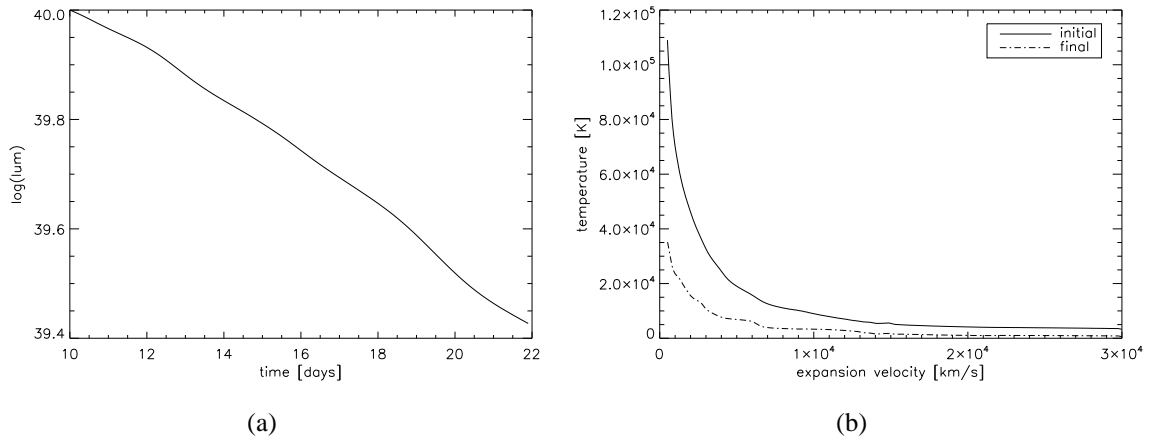


Figure 5.9: Test atmosphere, which is just expanding. (a) The observed luminosity of the atmosphere. As can be seen, the luminosity is continuously decreasing. (b) The whole atmosphere is cooling down, as the plot of the temperature structure shows.

through the atmosphere, the entropy of each layer should be conserved. To be consistent with the hydrodynamics equations, the entropy is deduced from the first law of thermodynamics. A change of the entropy during a time step is therefore given by

$$\frac{\Delta S}{mR} = \frac{3}{2} \frac{1}{m_u} \ln \left( \frac{T_2}{T_1} \right) + \frac{3}{2} \left( \frac{1}{m_{u2}} - \frac{1}{m_{u1}} \right) - \frac{1}{m_u} \ln \left( \frac{\rho_2}{\rho_1} \right), \quad (5.20)$$

where 2 is the index of quantities at the new time and 1 is the one of the old. For the integration of the temperature and the density term,  $m_u$  is kept fixed. This is a good approximation, as it is simpler to solve, and the resulting differences for the entropy are small. With the setup of a just freely expanding SN Ia atmosphere, the entropy has been computed. Even for a long time step of 1000s the entropy stays almost constant, the relative change of the entropy was  $\approx 10^{-6}$  at most.

### 5.2.3 Energy deposition

To test the energy deposition by the radioactive decay of nickel and cobalt into the atmosphere, a test case is considered, where only this gamma ray emission of the radioactive decay is calculated with the hydrodynamical solver. The energy change due to free expansion and energy transport is neglected to see the direct effect of the additional energy put into the atmosphere.

The results of the gamma ray emission calculation with the hydrodynamical solver is presented in figure 5.10. The observed luminosity over time is shown in figure 5.10(a). Caused by the energy added to the atmosphere, the luminosity seen by an observer increased. The figure 5.10(b) shows the temperature structure of the initial and the final atmosphere. As can be seen, a few layers located in the inner part of the atmosphere have an increased temperature. In these layers the radioactive isotopes of nickel and cobalt are located. Thus, the energy is deposited into these layers. Because the energy transport is turned off, this

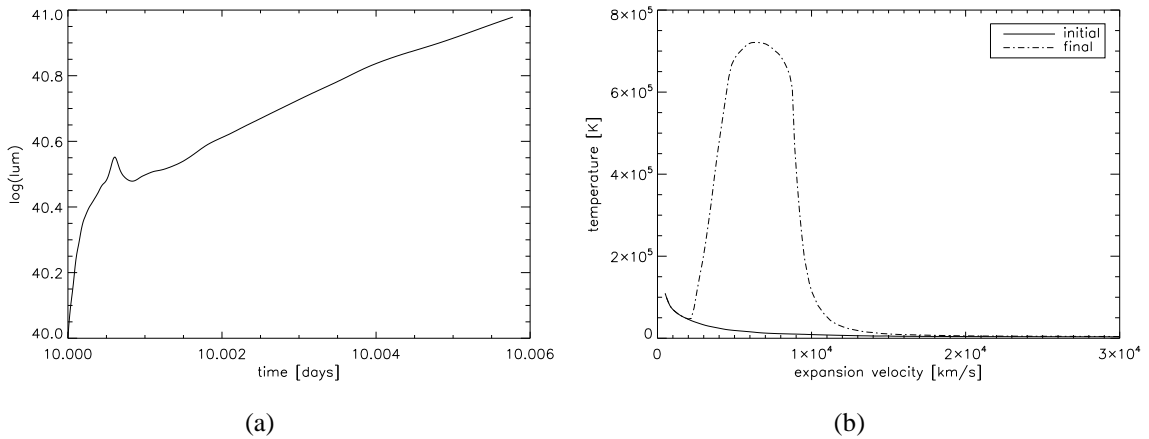


Figure 5.10: For this test calculation an additional energy input from gamma ray emission is considered. (a) The observed luminosity over time. Because of the additional energy, the luminosity increases. (b) The initial and resulting temperature structure. The temperature of some inner layers has been increased significantly.

energy stays in this part of the SN Ia atmosphere. Hence, for the modeling of a realistic SN Ia atmosphere, the energy transport is needed to distribute the additional energy into the whole atmosphere.

#### 5.2.4 Realistic test scenario

After all single effects have been tested, now an atmosphere, where all effects are considered for the hydrodynamical solver is calculated. Again the same initial temperature structure is used. So, the free expansion as well as the energy deposition and energy transport are active for this computation.

The results of the test calculation are presented in figure 5.11. The observed luminosity is plotted in figure 5.11(a). The luminosity increases because of the energy input from  $\gamma$ -ray emission due to radioactive decay. It takes some time, until the whole atmosphere has relaxed to this new condition. The atmosphere is then in radiative equilibrium state, and the luminosity stays constant. The initial and final temperature structure are plotted in figure 5.11(b). The energy input caused by the radioactive decay has increased the temperature of the whole atmosphere. The atmosphere is heated by the  $\gamma$ -ray emission in the inner part of the atmosphere. Due to this increasing energy the luminosity of these layers increases and the heat is radiated away and absorbed by the surrounding layers. This energy transport takes care that the deposited energy is moving through the whole atmosphere so that the temperature increases everywhere and the additional energy from the radioactive decay is radiated away towards the observer. The atmosphere is then in radiative equilibrium.

This has been an actual SN Ia atmosphere calculation. The hydrodynamical solver covers all the effects that influence the atmosphere of the SN Ia event. It moves the temperature structure towards radiative equilibrium. The hydrodynamical solver can now be applied to calculate an SN Ia light curve.

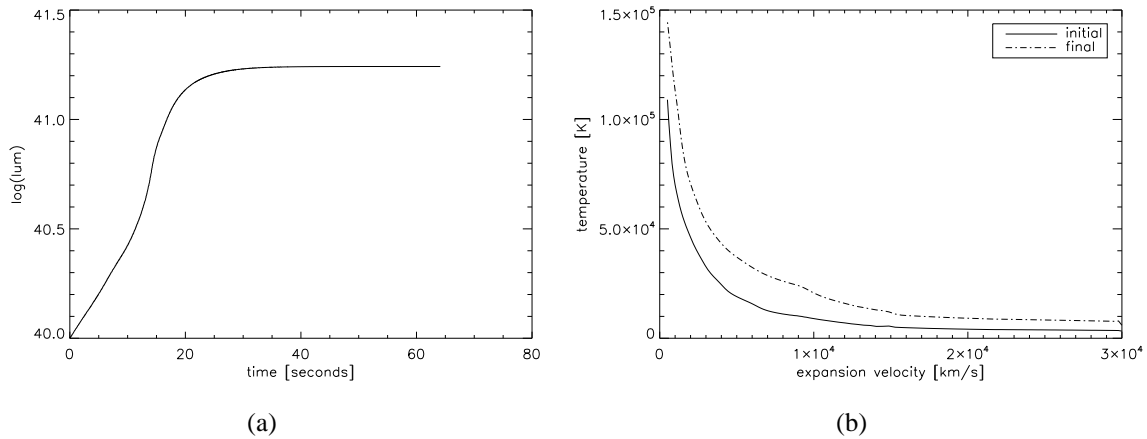


Figure 5.11: Result of a realistic test scenario. All influences on the atmosphere are considered. (a) The luminosity increases due to the energy deposition by radioactive decay. (b) The final and initial temperature structure.

### 5.3 Conclusions

A hydrodynamical solver has been implemented into the general purpose stellar atmosphere code PHOENIX. It calculates the energy change in the atmosphere by taking into account the homologous expansion, the energy deposition by  $\gamma$ -ray emission and the energy transport through the atmosphere. An adaptive time step procedure has been implemented to always obtain the optimal time step size for an atmosphere evolution calculation. Applying this hydrodynamical solver to an SN Ia atmosphere numerous test calculations have been performed. All the results confirm that each part of the hydrodynamical code is working as expected. The energy transport changes the temperature structure to get the SN Ia atmosphere to radiative equilibrium. A resulting temperature structure is almost the same as one obtained with the PHOENIX temperature correction procedure. Due to the energy transport, the temperature structure is always pushed to radiative equilibrium. Therefore, perturbations of the innermost layer can move through the atmosphere and the temperature structure of the whole atmosphere always relaxes to the new condition and moves back to radiative equilibrium. For the case of the freely expanding atmosphere, the temperature structure is cooling down for the whole atmosphere. This can be observed by a decreasing luminosity. The energy input by radioactive decay increases the energy of the atmosphere, and, therefore, the temperature structure changes in those layers, where the radioactive isotopes of nickel and cobalt are present. The observed luminosity is increasing. This all indicates that the hydrodynamical solver is working correctly, and it can now be applied to realistic scenarios, where the calculation of an SN Ia light curve is the main goal.

# Chapter 6

## Modeling SN Ia light curves

In this chapter, the hydrodynamical solver that has been implemented into the general purpose atmosphere code `PHOENIX` is used to calculate theoretical light curves of SN Ia events. The first section presents the approach to generate an SN Ia model light curve in different spectral bands that can be used to compare to observed light curves. In the second section, the model light curves have been computed with the assumption of an atmosphere in LTE. The atmosphere structures of different explosion models are used to calculate SN Ia light curves. These are compared to determine which one may be the best explosion model. To achieve further improvements of the model light curves, some investigation with the assumption of an atmosphere in NLTE have been performed and are presented in section 3. A short look on the spectral evolution of SN Ia is presented in section 4. This chapter closes with a conclusion.

### 6.1 Observed SN Ia light curves

To understand the physics of type Ia supernovae, observations are the key to learn more about them. Numerous spectra as well as light curves have been obtained, while a few hundred supernovae are discovered each year. In this work, the focus lies on the modeling of light curves of type Ia supernovae. Observations provide the facts that have to be reproduced by theoretical approaches to SN Ia simulations. The simulations will give the understanding of the physics that is going on in an SN Ia explosion.

The online supernova spectrum archive (`SUSPECT`) (Richardson et al. 2001, 2002) provides numerous of observations of different types of supernovae. For this work, the observed light curves of SN 2002bo and SN 1999ee are used to compare them to the calculations of model light curves performed in the following. Both SNe Ia have been observed in a few photometric bands. SN 2002bo has been discovered on March 9 in the galaxy NGC 3190. Optical and near-infrared spectra have been obtained. It also have been obtained photometric observations of SN 2002bo in different photometric bands (Benetti et al. 2004). SN 1999ee has also been observed to take spectra (Hamuy et al. 2002) and light curves in different photometric bands (Stritzinger et al. 2002).

### 6.2 Model light curves of SNe Ia

The new hydrodynamical solver is now applied to SN Ia model atmospheres in order to obtain model light curves for the whole evolution of an SN Ia envelope during the free

expansion phase. In this section, the actual scheme to obtain a full light curve evolution of an SN Ia in different photometric bands is presented. The observed light curves of two SNe Ia events are presented as well, because they are used to check the model light curves for accuracy.

### 6.2.1 Method

The hydrodynamical solver was presented in detail in the previous chapter. It is now applied to calculate synthetic light curves of SNe Ia. The SN Ia light curve evolution is calculated during the free expansion phase. The actual explosion process is not simulated. Therefore, for the starting model structure, the results of the explosion calculation of other groups are used as the input structure. Each layer has a certain expansion velocity, which does not change during the evolution, because homologous expansion is assumed. The model light curve calculation starts at a few days after the explosion. In the first few days the SN Ia envelope is optically thick and compact. Another point is that in the first few days the observed SN Ia light curves are quite faint and almost no observations of this early phase have been obtained. Therefore, for the model light curve calculation, it is adequate to start the light curve calculation a few days after the explosion. The starting structure is given by the result of the explosion model simulation. The results of the explosion model give the expansion velocities, density structure and the non-homogeneous abundances of all chemical elements present in the SN Ia envelope. The atmosphere expands for the first few days by assuming homologous expansion. The radii are determined by the expansion velocities and time of expansion. For the first temperature structure guess, the PHOENIX temperature correction procedure is used to obtain a start temperature structure in radiative equilibrium.

For the computation of an SN Ia model light curve, the hydrodynamical solver works on the start model atmosphere structure. The atmosphere structure then adapts to the new conditions caused by  $\gamma$ -ray emission and other hydrodynamical effects. After some time, the atmosphere eventually reaches the radiative equilibrium state. A typical time step of a hydrodynamical change in the model atmosphere is about 0.1s. This is a very small time step, but with an explicit method it is not possible to obtain bigger time steps. It takes about 500 time steps to reach radiative equilibrium depending in which evolution phase the SN Ia is. For the later phase after the maximum of the SN Ia light curve, fewer time steps are needed. This first radiative equilibrium atmosphere structure is now used to calculate a more detailed spectrum, where more wavelength points are used. This model spectrum is then used to obtain the first point of the model light curve for each band by using the filter functions described below. It certainly would need too much computation time to calculate a whole light curve evolution by using the typical time steps of about 0.1s. Therefore, to obtain the next point of the light curve, big time steps are computed. For these big time steps, the atmosphere is only expanding. This means that neither energy deposition by  $\gamma$ -ray emission nor energy transport through the atmosphere is considered for the solution of the hydrodynamical solver. After half a day computed with big time steps, the whole hydrodynamical solver works on the atmosphere again and the next point in the light curve is achieved after the atmosphere structure moved back to radiative equilibrium. Even with the use of these big time steps, about 10,000 time steps have to be calculated for a light curve of 50 days. For the normal model atmosphere calculation in PHOENIX with the temperature

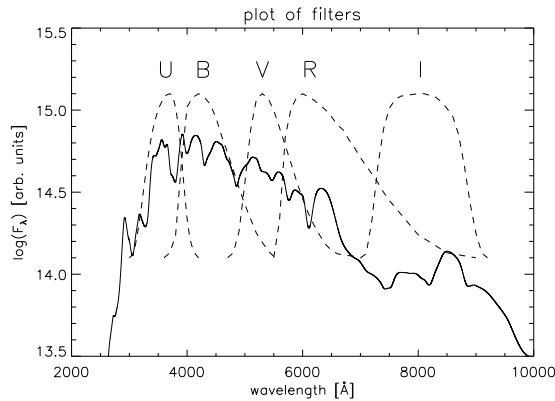


Figure 6.1: A typical model spectrum of an SN Ia together with the filter functions for the U, B, V, R and I band. These are used to determine the brightness in each band for the model light curves.

correction procedure, the radiative transfer equation has to be solved about 100 times at most. Therefore, the computation of a whole SN Ia model light curve is very expensive concerning the computation time, because the solution of the radiative transfer equation has to be obtained too many times. It takes a huge amount of computation time to calculate even simple SN Ia model light curves, even when using only a few wavelength points. Basically, the SN Ia model light curve is a curve consisting of half day points, where the atmosphere is in radiative equilibrium. During the later phase after maximum of the light curve, the big time steps have been performed for one or even two days, as the hydrodynamical changes in the SN Ia atmosphere become smaller.

As described above, a model spectrum is calculated with the obtained atmosphere structure, which is in radiative equilibrium at each half day point of the light curve. To obtain a model light curve for different photometric bands, filter functions were used to calculate the brightness in different bands. In figure 6.1, an SN Ia model spectrum and the used filter functions of the U, B, V, R and I band are shown. These filter functions are described in Hamuy et al. (1992). With these filter functions, SNe Ia model light curves can now be obtained for these five different photometric bands.

### 6.3 Light curves of LTE models

For the first calculations of theoretical light curves, the model atmosphere of the SN Ia is considered to be in LTE. For a first approach to obtain model light curves this is adequate. Another reason for the assumption of LTE is that model light curve calculations with an atmosphere treated in NLTE use much more computation time. In order to obtain an SN Ia model light curve in a reasonable computation time, a model atmosphere in LTE is a necessary assumption. The method applied to obtain a SN Ia model light curve is described in the section above. For the model light curve calculations presented in this section the following parameters were chosen. The model atmosphere is divided into 128 layers. The radiative transfer is solved including atomic lines of the Kurucz atomic data line list. The number of wavelength points used for the solution of the radiative transfer is about 2400.

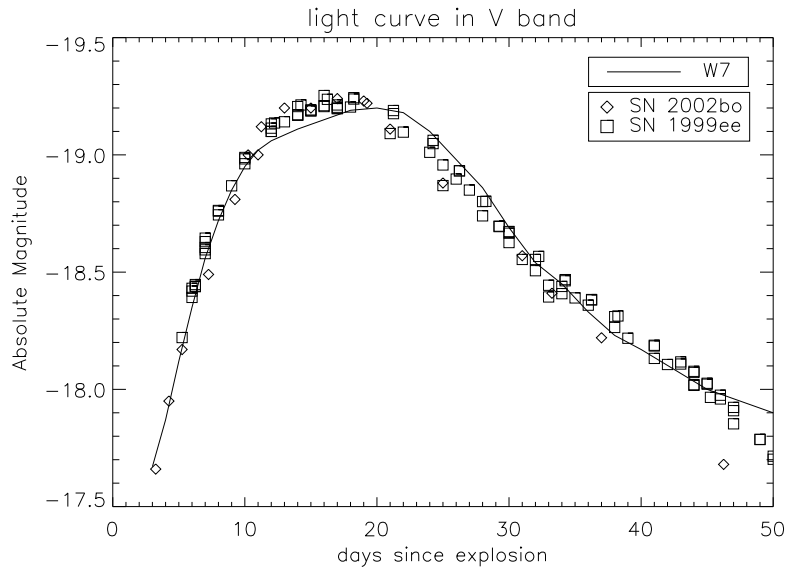


Figure 6.2: LTE model light curve of the W7 explosion model in the V band compared to two observed SN Ia light curves of SN 1999ee and SN 2002bo.

### 6.3.1 UVRI light curves

For the first light curve calculation, the W7 deflagration explosion model is used to obtain model light curves of SNe Ia in different photometric bands. The first point of the light curve was calculated at three days after the explosion. The method to obtain the theoretical light curves is described in section 6.2.1.

Figure 6.2 shows the LTE SN Ia model light curve of the W7-based explosion model in the optical V band. The theoretical light curve represents the observed light curves of two SNe Ia events very accurately. The steep rise of the model light curve beginning at three days after the explosion is in agreement with the observed light curves. The maximum of the W7-based model light curve seems to be later than the one of the observed light curves. At 20 days after the explosion, the model light curve has its maximum, while the maximum of the observed light curves is around 17 days after the explosion. After the maximum, the decline of the light curve of the W7-based model represents the observed light curve quite well. Even up to the later phase at 50 days after the explosion, where the atmosphere gets significantly thinner, the fit to the observed light curves is quite accurate.

For the other photometric bands, the computed model light curves are also compared to the observed SN Ia light curves. The theoretical light curve in the ultraviolet U band is shown in figure 6.3(a). Only an observed light curve of SN 1999ee is available. As can be seen from this figure, the observational data are scattered. The rise in the beginning as well as the maximum phase is well represented by the model light curve. However, the decline of the theoretical light curve seems to be too steep. This same effect is present in the model light curve of the B band, which is shown in figure 6.3(b). Here, the first days of the model light curve are too bright compared to both observed SN Ia light curves. The maximum phase of the model light curve is in good agreement with the observed ones. At day 50, the model light curve becomes brighter than the observed light curves.

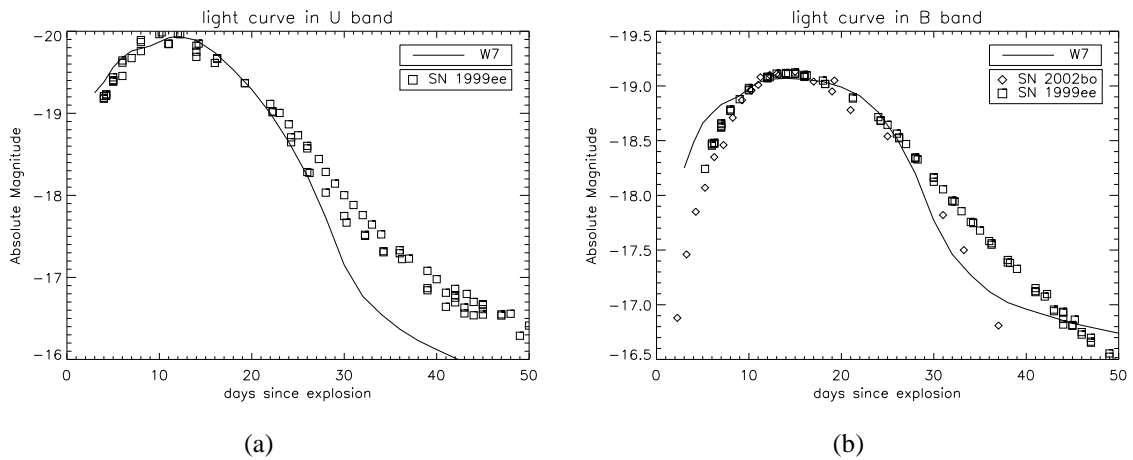


Figure 6.3: LTE light curves of the W7 explosion model. (a) In the U band the theoretical light curve has a steeper decline than the observed light curve. (b) The B band model light curve is too bright during the first few days.

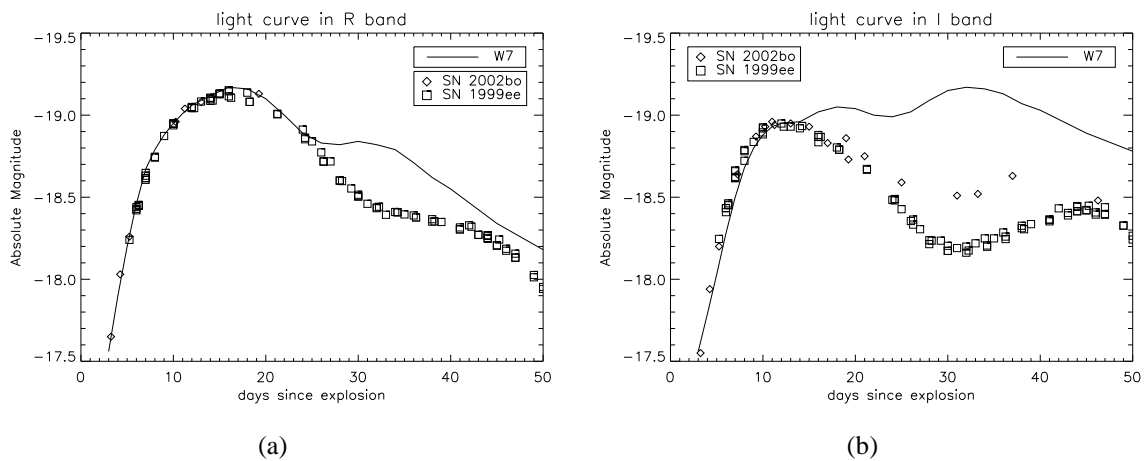


Figure 6.4: LTE light curves of the W7 explosion model. (a) The theoretical light curve in the R band seems to rise after a first decline after the maximum phase. (b) For the I band the model light curve has no distinctive maximum. At 30 days after the explosion the model light curve is way too bright in comparison to the observed ones.

In figure 6.4(a), a plot of the model light curve of the R band is shown. The steep rise in the beginning and the maximum phase of the observed SN Ia light curves is well represented by the computed model light curve. However, as can be seen from the figure, the theoretical light curve fit gets worse for the later phase after the maximum. The brightness of the model light curve seems to rise again at around day 25 after the explosion. Up to day 45, the model light curve has a second bump, which is not observed in the light curves of SN 1999ee and SN 2002bo. In the infrared I band, the decline after the maximum phase is missing, as can be seen from figure 6.4(b). Like in the R band, the rise in the beginning and the maximum are well represented in the model light curve. However, at the maximum phase, the brightness of the SN Ia model light curve rises further, which is not seen in the observed light curves of SN 2002bo and 1999ee. Around day 30, the difference between model and observed light curve in the I band are about 1 mag. To day 50, the model light curve declines, while the observed light curves show their second maximum around 40 days after the explosion.

To conclude, in the V band the model light curve represents the observed light curve quite accurately. For the B band and the U band, this is also the case, despite some deviations during the later declining phase, where the model light curves seem to be too faint. Significant differences between observed and model light curves arise in the R band and definitely in the infrared I band. Here, the decline after the maximum phase observed in the SNe Ia light curves is not present in the simulated light curve. In the following, further investigations on the infrared problem will be performed to find the cause of the differences.

### 6.3.2 Dynamical models

The W7 deflagration explosion model is only one of the possible explosion models which are considered for an SN Ia event. Other explosion models need to be calculated and compared to the W7 deflagration model and the observed light curves to determine the best explosion model. Therefore, results of hydrodynamical explosion calculations of other groups are used to calculate model light curves. One possible explosion model is the deflagration model W7 (Nomoto et al. 1984), which has already been used to compute SN Ia model light curves. Other possible explosion models are the delayed detonation models. Two results for these explosion model calculations are used here to compute SN Ia model light curves. These are the models DD 16 and DD 25 presented in Höflich et al. (2002). The density structures of the three used explosion models are shown in figure 6.5(a). At the inner part of the atmosphere, the densities are almost the same for all three explosion models. At the outer part of the atmosphere, the density of the W7 deflagration model is significantly lower than the density of the two delayed detonation models. The density structures of the two delayed detonation models are quite similar. Between the three explosion models, there are also differences in the abundances of the elements produced during the explosion. In particular, the amount of  $^{56}\text{Ni}$ , which was produced during the explosion, is different. In figure 6.5(b) the amount of  $^{56}\text{Ni}$  that has been produced during the explosion is shown for all three models. In the explosion model DD 16 less  $^{56}\text{Ni}$  is produced than in the models DD 25 and W7. The  $^{56}\text{Ni}$  produced in the two delayed detonation models is also present in different layers than in the deflagration model. The amount of produced  $^{56}\text{Ni}$  is known to have a strong influence on the light curves of SNe Ia, because the more  $^{56}\text{Ni}$  is present the more energy is put into the SN Ia atmosphere due to radioactive decay of the  $^{56}\text{Ni}$  and its decay product  $^{56}\text{Co}$ .

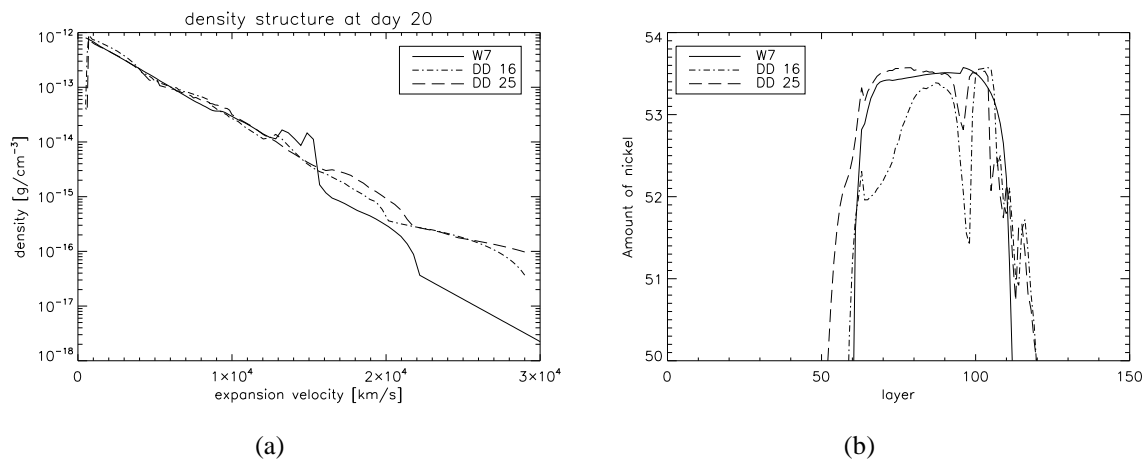


Figure 6.5: The atmosphere structure of the three used explosion models. The W7 deflagration and two delayed detonation models are used for the light curve calculations. (a) Density structure at 20 days after the explosion. (b) Amount of  $^{56}\text{Ni}$  present at the beginning.

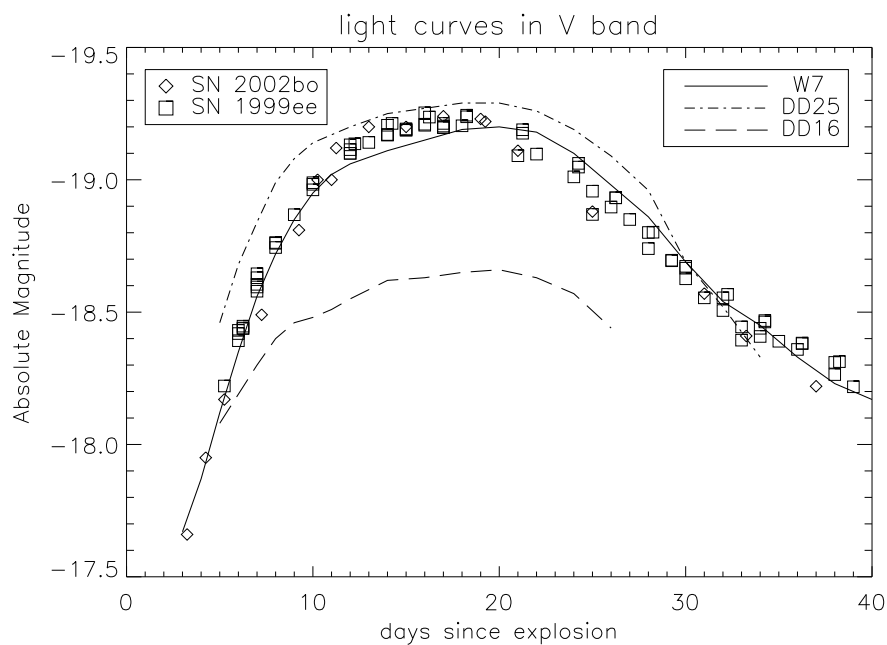


Figure 6.6: LTE model light curves of SNe Ia for three different explosion models in the V band.

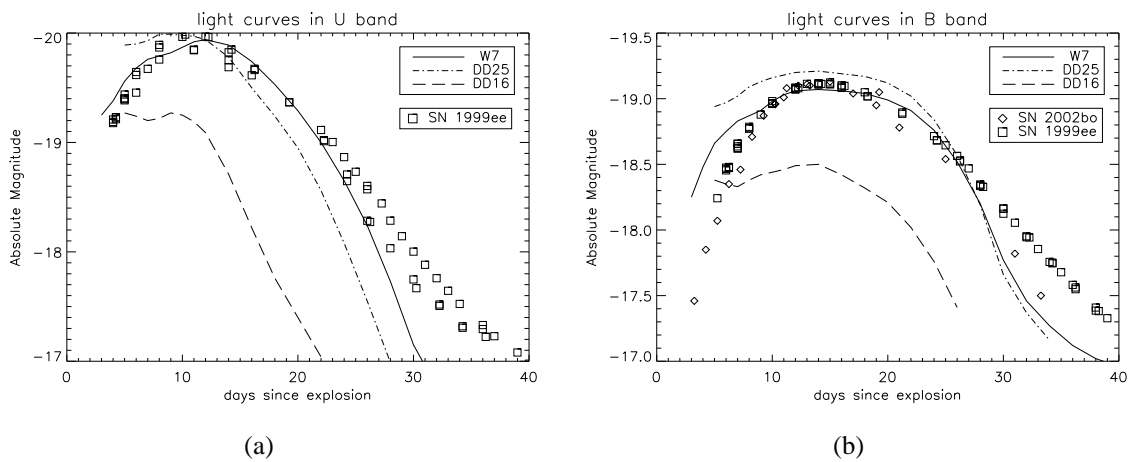


Figure 6.7: LTE light curves of the three explosion models. (a) In the U band, the DD 16 light curve is too faint. (b) In the B band, the model light curves at the later phase are too bright.

Using these three explosion models, LTE model light curves were computed with the hydrodynamical solver. In figure 6.6, the three explosion model light curves in the V band are presented. The most obvious difference between the model light curves is the peak absolute magnitude. The DD 16 model is the faintest of the three explosion models. The DD 25 model is the brightest and the W7 deflagration model is almost as bright as the DD 25 model. The physical reason behind this is the heating of the atmosphere caused by the  $\gamma$ -ray deposition due to radioactive decay of  $^{56}\text{Ni}$  and its decay product  $^{56}\text{Co}$ . The more  $^{56}\text{Ni}$  is produced during the explosion the more radioactive decay energy is present during the evolution of the SN Ia atmosphere, and the model light curve is brighter at the peak of the light curve. The DD 16 model atmosphere indeed has only 0.3 solar masses of  $^{56}\text{Ni}$ , while the DD 25 and W7 model atmosphere have about 0.6 solar masses of  $^{56}\text{Ni}$ . This is also shown in figure 6.5(b), where the amount of  $^{56}\text{Ni}$  is plotted. Therefore, from the theoretical light curve computation point of view, the DD 16 explosion model can be ruled out as the correct explosion model causing these events. It also shows that the hydrodynamical solver reproduces the expected behavior considering the energy change caused by the radioactive decay.

The model light curves of other bands have also been computed. In figure 6.7(a), the model light curves of the three explosion models in the U band are presented. The light curve of the explosion model DD 16 is too faint to reproduce the observed light curve of SN 1999ee. In the model light curve no distinctive maximum is produced. For the first days, the model light curve of the DD 25 model is brighter than the W7 deflagration model light curve. The decline of the light curve of the DD 25 model after maximum is steeper, and in the later phase the DD 25 model light curve is too faint compared to the observed light curve of SN 1999ee. The W7 model light curve is the best fit to the observed light curve. In figure 6.7(b), the model light curves of the three explosion models in the B band are shown. Again, the model light curve of the DD 16 model has no distinctive maximum, and it is also too faint to reproduce the observed light curves. The DD 25 model is a bit brighter than the W7 deflagration model, and they both have similar light curve shapes. During the first phase, the

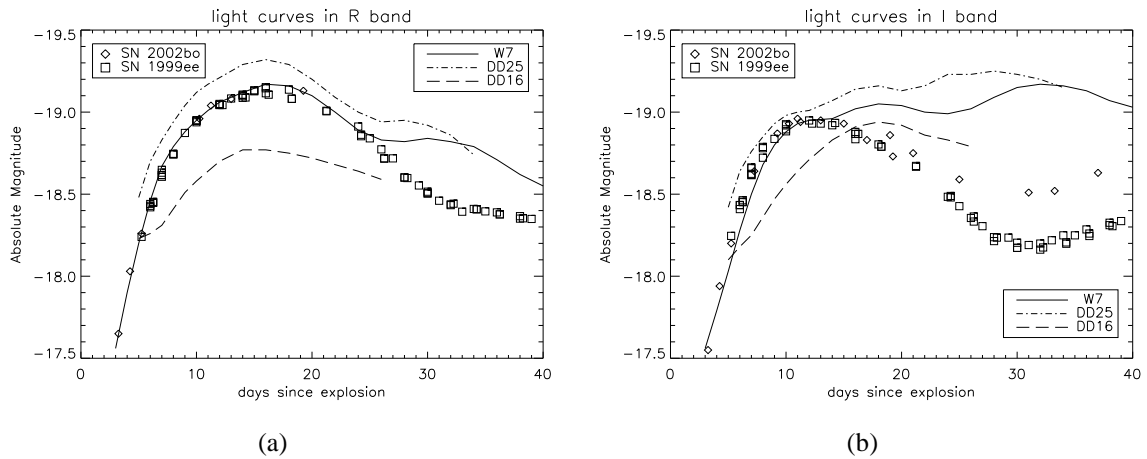


Figure 6.8: LTE light curves of the three explosion models. (a) In the R band, the DD 16 light curve is too faint. (b) In the I band, the model light curves at the later phase are too bright.

model light curve of the DD 25 explosion model is too bright. It does not show the steep rise in the beginning, which is observed in the two light curves of the SN Ia events. After the maximum, the light curves of the DD 25 and the W7 model have the same luminosities. Again, the W7 model light curve seems to be the best fit to the observed light curves.

The model light curves of the three explosion models in the R band are shown in figure 6.8(a). The light curve of the DD 16 explosion model again is too faint. However, the differences to the observed light curves are not as huge as in the other bands presented before. The model light curve of the DD 25 model shows a similar shape like the W7 deflagration model. Both light curves have their maximum around 17 days, which is when the observed light curves have their maximum. During the declining phase, the model light curve of the DD 25 model shows a deviation from the observed light curves at around 30 days after the explosion. This is also seen in the W7 deflagration model. In figure 6.8(b), the infrared light curves in the I band of the three explosion models are shown. All three model light curves do not reproduce the observed light curves well. The DD 25 and the W7 model reproduce at least the steep rise during the first phase of the observed light curves. However, after the maximum phase, all theoretical light curves show a rise in the brightness, while instead the observed SN Ia light curves are declining. Even in the V band too faint DD 16 model rises to a brightness brighter than the one in the observed light curves. Thus, the use of a different dynamical model does not improve the fit to the observed light curves in the I band. Summarized, the DD 16 does not seem to be the correct explosion model of the SN Ia events. The W7 deflagration model seems to be the best fit to the observed SN Ia light curves. However, the DD 25 model is also in reasonable agreement with the observed light curve. In the infrared I band, all explosion models show significant deviations from the observed light curves in the phase after the maximum.

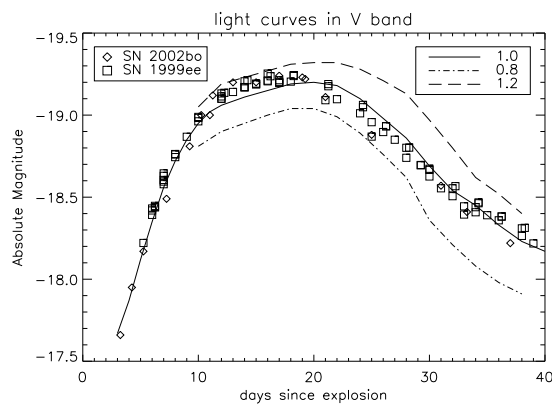


Figure 6.9: LTE light curve of the W7 model calculated with different energy deposition. In the V band there arise differences in peak absolute magnitude.

### 6.3.3 Influence of the energy deposition model

Tests about the influences of the many parameters of the hydrodynamical models are needed to check whether the effects are reasonable considering the physics of the SN Ia atmosphere. Here, an investigation is performed that checks how a different amount of energy input into the model atmosphere leads to differences in the resulting model light curves. Furthermore, the changes in the energy deposition may improve the theoretical light curves especially for the I band. For this energy deposition test, the W7 deflagration model is used for the calculation of the model light curves. The amount of the energy deposition is obtained by the implemented procedure. This obtained deposition of energy, which is put into the total energy change, is then changed by an arbitrary test factor. The abundances of  $^{56}\text{Ni}$ ,  $^{56}\text{Co}$  and  $^{56}\text{Fe}$  are not changed.

In figure 6.9, a plot of SNe Ia model light curves with different energy depositions are shown. Here, the model light curves in the V band are under investigation. One light curve is the original model light curve of the W7 model, where the energy deposition has not been changed. Two light curves one with 80 % and one 120% of the original energy deposition have been calculated. As can be seen in the figure, the difference in the amount of the deposited energy has a direct influence on the maximum brightness of the computed model light curves. As expected, an SN Ia model light curve, where more energy is put into the atmosphere, shows a brighter maximum. The model light curve, where less energy is deposited into the atmosphere has a fainter maximum. It can also be seen that the overall shape of the model light curves does not change if a different amount of energy is put into the atmosphere.

The model light curves of the U band are presented in figure 6.10(a). Again, the different amount of energy deposition changes the brightness of the model light curves everywhere. Even the light curve with 120% of the original energy deposition is in the later phase too faint, as can be seen in comparison to the observed light curves. In figure 6.10(b), the model light curves of the B band are presented. The model light curve with more energy deposited into the atmosphere is brighter than the one with less energy deposition. However, the shape of the model light curves are quite similar. Like in the U band, the light curves at the later

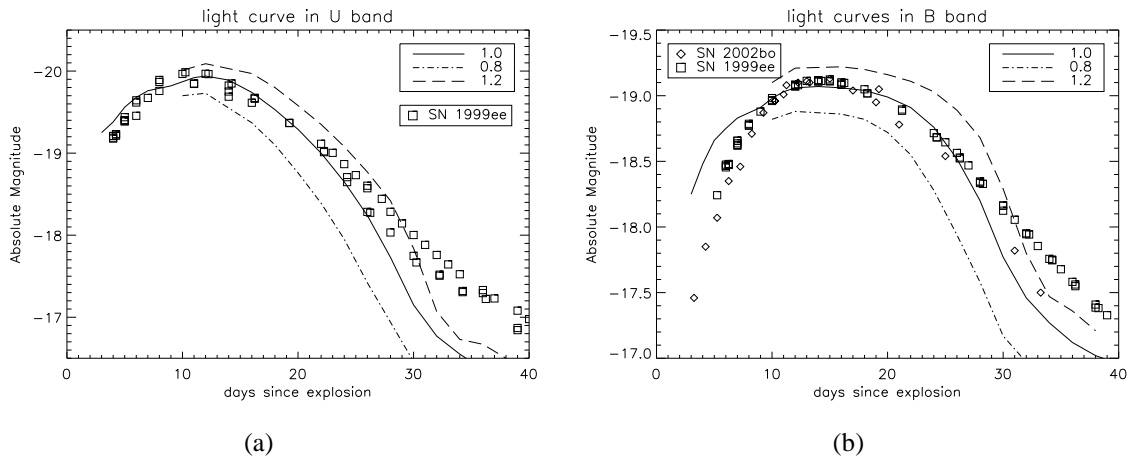


Figure 6.10: LTE light curve of the W7 model calculated with different energy deposition. (a) In the U band there arise differences in peak brightness. (b) In the B band there are small differences. The fit at the later phase has not improved.

phase are too faint even the one, which has more energy input into the atmosphere.

The model light curves with different energy depositions in the R band are shown in figure 6.11(a). Here, the differences between the light curves for different energy depositions are smaller than for the U, B or V band model light curves. The maximum phase is quite similar for all three light curves with different energy input. The light curve with more energy input is brighter than the light curves with less energy input. At the later phases all model light curves are too bright. However, the light curve with only 80% of the original energy deposition is at around 40 days as bright as the observed light curves. In the infrared I band, the model light curves, which are shown in figure 6.11(b), show almost no significant differences in the brightness with a different factor of energy deposition. All three model light curves rise after the maximum to a higher brightness than in the observed SN Ia light curves. Thus, a different energy deposition does not have an influence on the I band model light curves. Therefore, the fit to the observed light curves in the I band cannot be improved by using a different amount of energy deposition into the model atmosphere.

To summarize, the energy deposition has an influence on the model light curves. The model light curve, where more energy is put into the atmosphere, shows a brighter light curve than one with less energy input. It can also be said that the influences for the U, B and V band are significant, where for the R and the I band the differences become smaller. This change of energy deposition simulated that a different amount of  $^{56}\text{Ni}$  may have been produced during the explosion. It can also mean that the procedure to obtain the deposited energy needs improvements. For instances, the assumption of gray radiative transfer for the  $\gamma$ -rays is not a good approximation.

### 6.3.4 Near-infrared light curves

As presented in the previous sections, all model light curves in the I band do not represent the observed SN Ia light curves correctly. During the later phase beginning at 25 days after the explosion, the deviations between model and observed light curves are quite huge. In this

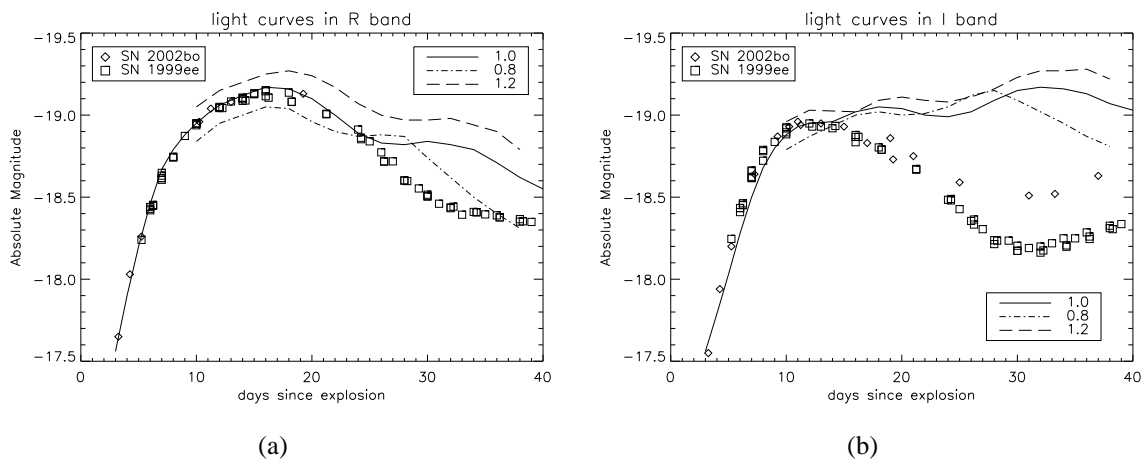


Figure 6.11: LTE light curve of the W7 model calculated with different energy deposition. (a) In the R band there arise differences in peak brightness. (b) In the I band there are small differences. The fit at the later phase has not improved.

section, the focus lies on the modeling of SNe Ia light curves in the near-infrared beyond the I band. Light curve observations in the J, H and K band of the two SNe Ia have been obtained. Photometric observations in the J and H band of SN 1999ee are presented in Krisciunas et al. (2004a). For SN 2002bo photometric observations in J, H and K band have been obtained (Krisciunas et al. 2004b). The procedure to obtain the model light curves for the near-infrared J, H and K band is the same as for the other bands. The W7 deflagration model has been used to calculate the model light curves under the assumption of an model atmosphere being in LTE. Filter functions are applied on the computed model spectra to obtain the model light curves for the infrared bands. A spectrum of an SN Ia model atmosphere is shown in figure 6.12. The used filter function of the J, H and K band are shown as well. The J band filter is located between a wavelength of  $1.1\mu\text{m}$  and  $1.35\mu\text{m}$ . As can be seen in the figure, between  $1.5\mu\text{m}$  and  $1.8\mu\text{m}$  is the wavelength range for the H band filter. The K band filter is between  $2\mu\text{m}$  and  $2.3\mu\text{m}$  wavelength.

The model light curve in the J band is shown in figure 6.13(a). The first 25 days of the observed light curves are well represented by the calculated LTE model light curve. The rise to the maximum as well as the maximum phase is in good agreement with the observed SN Ia light curves. The model light curve rises to a second maximum at around 40 days, which is as bright as the first maximum. This second maximum has not been observed in the light curves of SN 2002bo and SN 1999ee. Here, the differences between model and observed light curves are very significant. The LTE model light curve in the H band is shown in figure 6.13(b). Again, the first phase up to day 20 is in good agreement with the observed SN Ia light curves. The model light curve has a bright maximum at day 35, which is not present in the observed light curves. Here, the difference between the model and the observed SN Ia light curves is almost 1.5 mag.

In figure 6.14, the LTE model light curve in the K band and the observed light curve of SN 2002bo are shown. No data is available for SN 1999ee for this band. Again, the model light curve represents the observed light curve for the first phase quit adequate. At day 25 after the explosion, the model light curve increases its brightness, which is not observed in

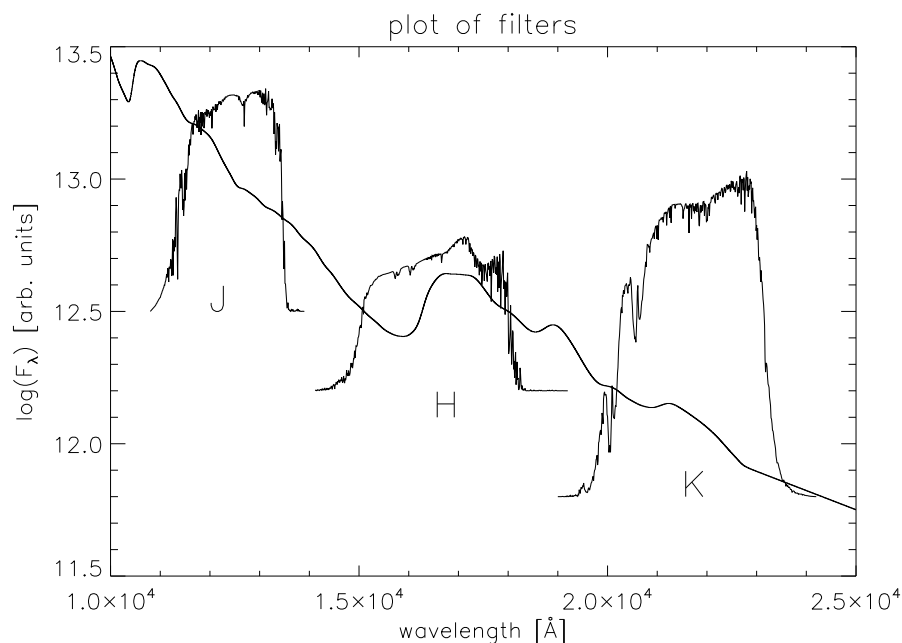


Figure 6.12: An LTE spectrum of the W7 deflagration model in the infrared at day 20 after the explosion. The filter functions of the J, H and K band are shown.

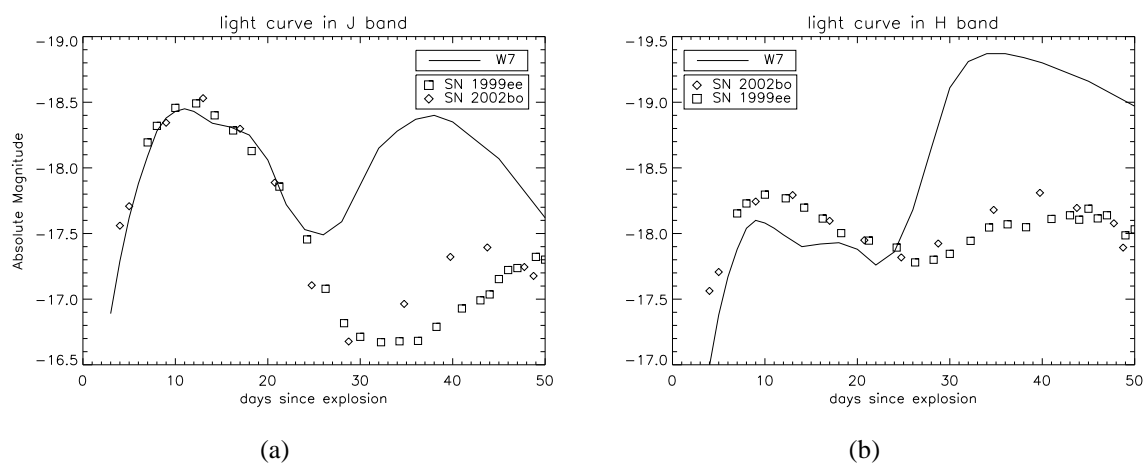


Figure 6.13: LTE light curves of the W7 model in the infrared. (a) Model light curve in the J band. The maximum at 15 days is also in the model light curve. However, in the model light curve the brightness increases after 25 days after the explosion. (b) Model light curve in the H band. Huge difference between model and observed light curve starting at 25 days after the explosion.

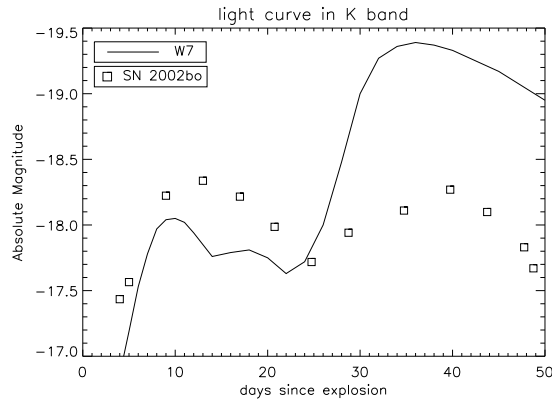


Figure 6.14: LTE light curve of the W7 model in the K band. Only observations of SN 2002bo are available, again the differences starting around day 25 arise.

the light curve of SN 2002bo. Almost 1.5 mag is the difference between model and observed light curve at day 35.

In the I, J, H and K band, the first 20 days of the model light curves are representing the observed light curves quite accurately. However, the model light curves show significant differences compared to the observed SN Ia light curves during the later phase beginning at around 20 days after the explosion. All calculated model light curves are significantly too bright during this phase. This indicates that in the whole wavelength range of the near-infrared, from  $0.8\mu\text{m}$  to  $2.3\mu\text{m}$ , the obtained model spectra are too bright. Therefore, the differences of the I band model light curve are not only a single problem of this certain band. In the whole near-infrared, the model light curves are not representing the observed light curves correctly during the later phase after the maximums.

### 6.3.5 Simple line scattering

The LTE model curves in the U, B and V band are in quite good agreement with the observed light curves. However, the model light curves in the R band and the infrared bands have larger differences compared to the observed SN Ia light curves. One possible explanation is that the assumption of an atmosphere being in LTE is obviously not correct. Therefore, the effects of scattering in the radiative transfer on the model light curves is tested. The source function for the radiative transfer equation including scattering for a two level atom can be written as

$$S_{\lambda} = (1 - \varepsilon_{\lambda})J_{\lambda} + \varepsilon B_{\lambda}. \quad (6.1)$$

The factor  $\varepsilon_{\lambda}$  is the scattering factor. For  $\varepsilon_{\nu} = 1$  only the thermal pool is active and no scattering is assumed. The source function is then given by  $S_{\lambda} = B_{\lambda}$ . This factor  $\varepsilon_{\nu}$  will vary over the whole wavelength range. For the calculation with PHOENIX it is possible to set a wavelength independent factor  $\varepsilon$ . This factor sets  $\varepsilon_{\lambda} = \varepsilon = \text{constant}$  for the line scattering over the whole wavelength range. Meaning that scattering is taken into account for the solution of the radiative transfer equation. To test the influences of scattering on the computed model light curves, this factor is now varied. For this purpose, the model light

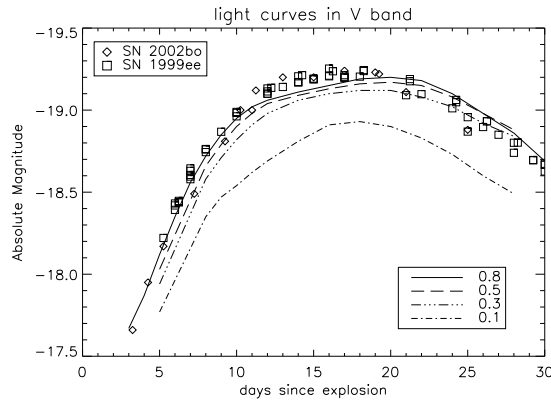


Figure 6.15: LTE light curves of the W7 explosion model calculated with different values of  $\epsilon$  in the V band.

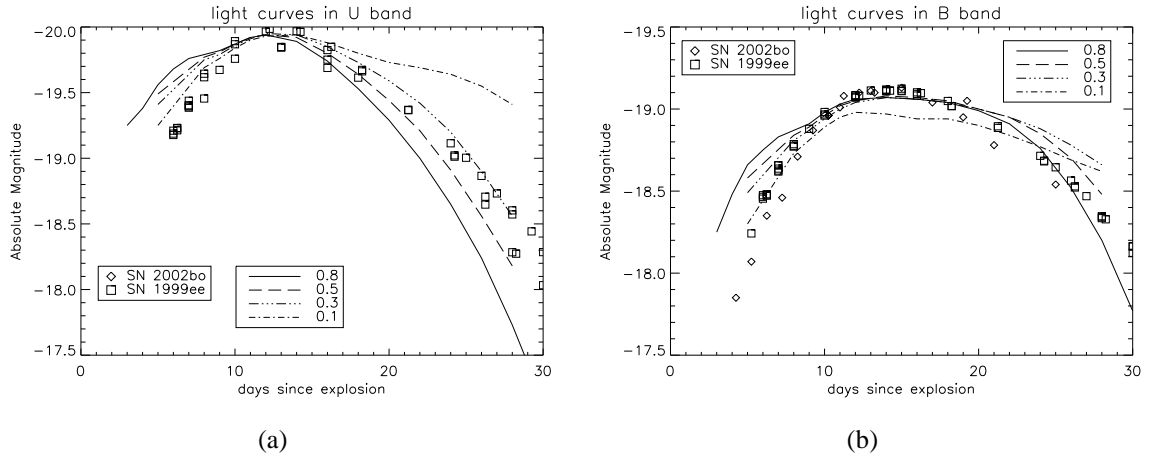


Figure 6.16: LTE light curves of the W7 explosion model calculated with different  $\epsilon$ . (a) Light curves of the U band. (b) A plot of the light curves with different  $\epsilon$  in the B band.

curves of the W7 deflagration model are calculated for an atmosphere that is in LTE but with different values for the scattering factor  $\epsilon$ . So far, the used value of the scattering factor for the computation of all model light curves was  $\epsilon = 0.8$ .

In figure 6.15, a plot of model light curves in the V band calculated with different values of  $\epsilon$  is shown. The differences between the model light curves computed with  $\epsilon = 0.8$ ,  $\epsilon = 0.5$  and  $\epsilon = 0.3$  are small. The lower the factor  $\epsilon$  is, the fainter becomes the brightness in model light curve. For  $\epsilon = 0.1$  the computed model light curve is fainter than the other ones. As can be seen, the shape of all model light curves still represent the shape of the observed SN Ia light curves.

In figure 6.16(a), the U band model light curves calculated with different values of  $\epsilon$  are shown. The model light curve calculated with  $\epsilon = 0.3$  seems to be the best fit to the observed SN Ia light curves. It does not show the steep decline after the maximum as seen in the  $\epsilon = 0.8$  model light curve. For the rise of the light curve, the model light curve calculated with  $\epsilon = 0.1$  is the best fit to the observed light curves. As can be seen from the figure, the model

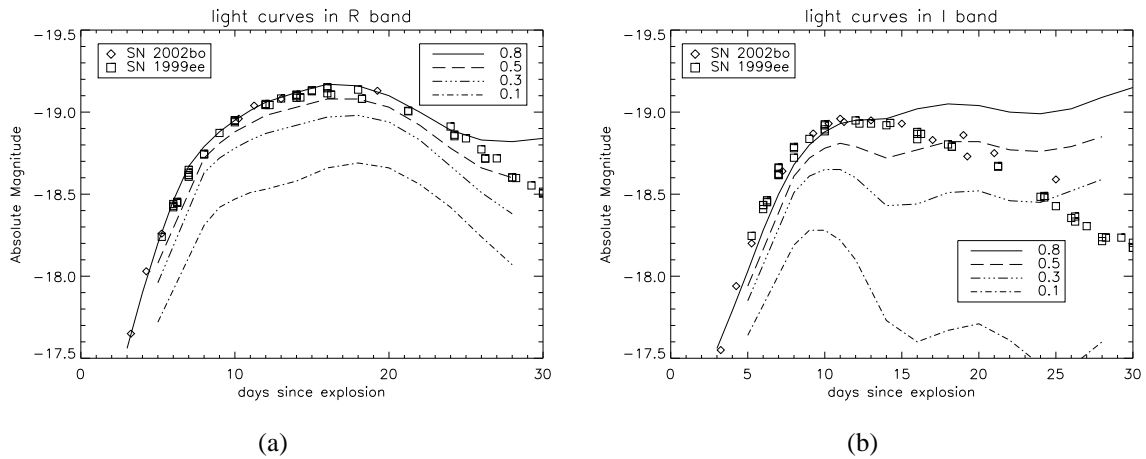


Figure 6.17: LTE light curves of the W7 explosion model calculated with different  $\varepsilon$ . (a) In the R band, a smaller  $\varepsilon$  leads to fainter light curves. (b) Huge differences in the light curves with different  $\varepsilon$  can be seen in the I band.

light curve for  $\varepsilon = 0.1$  is not in good agreement with the observed light curves during the later phase after the maximum. Interesting is that the peak absolute magnitude is almost the same for all model light curves. The B band model light curves are plotted in figure 6.16(b). The maximum peak has about the same brightness for  $\varepsilon = 0.3$ ,  $\varepsilon = 0.5$  and  $\varepsilon = 0.8$ . The light curve with  $\varepsilon = 0.1$  is too faint during the maximum phase and does not represent the observed light curves during the later phase. For the first days, the model light curve with  $\varepsilon = 0.1$  is the best fit.

In figure 6.17(a), the model light curves of the R band are shown. The influence of a different value of  $\varepsilon$  on the model light curves is significant. The model light curves with lower  $\varepsilon$  do not show the second rise at day 30. Therefore, for the modeling of SN Ia light curves in the R band, the scattering factor should be  $\varepsilon = 0.5$ , because it is the best fit to the observed SN Ia light curves. The model light curve calculated with  $\varepsilon = 0.1$  is again too faint. In the infrared I band, the influences of the chosen value for  $\varepsilon$  on the model light curves is even more significant, as can be seen from figure 6.17(b). With a decreasing  $\varepsilon$  the brightness of the model light curves also decreases. For a value of  $\varepsilon = 0.8$ , the light curve does not show a decline after the maximum at 12 days after the explosion. The model light curves of  $\varepsilon = 0.5$  and  $\varepsilon = 0.3$  do not show a decline either. Here, the brightness after the maximum stays almost constant. For  $\varepsilon = 0.1$  the light curve declines after the maximum but has a second maximum at 20 days, which has not been seen in the observed light curves of SN 2002bo and SN 1999ee. The model light curve of the  $\varepsilon = 0.1$  calculation is also very faint. For the I band, it cannot be said, which value of  $\varepsilon$  produces the best fitting model light curve to the observed ones. All computed model light curves show significant differences to the observed SN Ia light curves.

In this section, different values of the scattering factor  $\varepsilon$  were used to obtain LTE model light curves of the W7 model for different bands. It can be determined that scattering definitely has an effect on the calculation of model light curves. For the U, B, V and R band a smaller value of  $\varepsilon$  than used so far can improve the fit of the model light curves to the observed ones. A value between  $\varepsilon = 0.5$  and  $\varepsilon = 0.3$  seems to give the best fits to the observed

light curves. It can also be determined that a value of  $\varepsilon = 0.1$  is definitely too small as the computed model light curves are too faint to reproduce the observed light curves. In fact, the scattering should be treated in a more sophisticated way. The assumption of an SN Ia atmosphere that is not in LTE is the next step for the computation of model light curves of SNe Ia that fit the observed light curves more accurately.

## 6.4 Light curves of NLTE models

The LTE light curves in the V Band and most other bands are in quite good agreement with observed SN Ia light curves. However, in the near-infrared for the bands I, J, H and K, the model light curves need improvements especially for the later phase to fit the observations more accurately. So far, the SN Ia model atmosphere is considered to be in LTE during the whole evolution time. As the results presented in the section above have shown, scattering is important for the solution of the radiative transfer. Therefore, in this section the model light curves are calculated with the assumption of an atmosphere, which is not in LTE. The computation of model light curves with SN Ia model atmospheres, which are in NLTE, is difficult, because this needs a huge amount of computation time. At first, model light curves in NLTE are computed with an LTE temperature structure. Later, more realistic NLTE model light curves with a temperature structure that adapts to NLTE conditions are computed to investigate the NLTE effects on the model light curves.

### 6.4.1 NLTE light curves with LTE atmosphere structure

The first approach to compute NLTE model light curves is to consider the atmosphere to be in NLTE, but use a fixed LTE temperature structure. For this computation of NLTE model light curves, the radiative equilibrium LTE temperature structure of the W7 deflagration model is used. This temperature structure is kept constant and 20 iterations are performed to converge the NLTE, which is mainly the occupation numbers of the species that are considered for the NLTE calculation. The following species are considered for the calculation in NLTE: H I, He I, He II, C I-III, O I-III, Ne I, Na I, Mg I-III, Si I-III, S I-III, Ca II, Ti II, Fe I-III and Co II. These are the species that are most abundant in an SN Ia atmosphere and mainly contribute to the spectrum. The advantage of this approach to an NLTE model light curve is that no temperature iterations have to be performed. This reduces the computation time significantly, although about 200,000 wavelength points are calculated instead of 2,400 in case of LTE.

In figure 6.18, the SN Ia model light curve in the V band of an NLTE calculation with LTE temperature structure is shown. As can be seen from the figure, the NLTE light curve is fainter than the LTE light curve. During the maximum phase there is about 0.4 mag difference between both light curves. After the maximum the NLTE model light curve approaches the LTE light curve and represents the observed light curves as good as the LTE light curve. Overall, the NLTE model light curve in the V band does not represent the observed light curves very accurately. With the assumption of an atmosphere in LTE, a better fit is obtained, although NLTE is more physically accurate.

The NLTE model light curve of the U band is shown in figure 6.19(a). The NLTE light

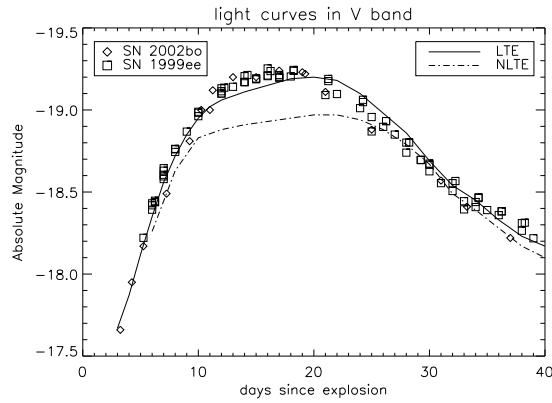


Figure 6.18: Model light curves of the W7 explosion model in the V band. The NLTE model atmosphere has an LTE temperature structure.

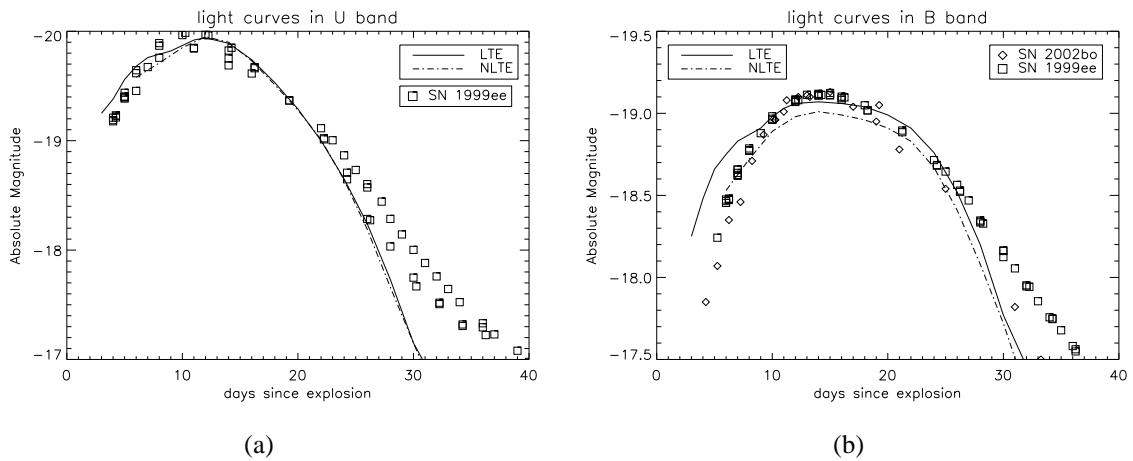


Figure 6.19: Model light curves of the W7 model. The NLTE model atmosphere has an LTE temperature structure. (a) The light curves of the U band. (b) The light curves of the B band.

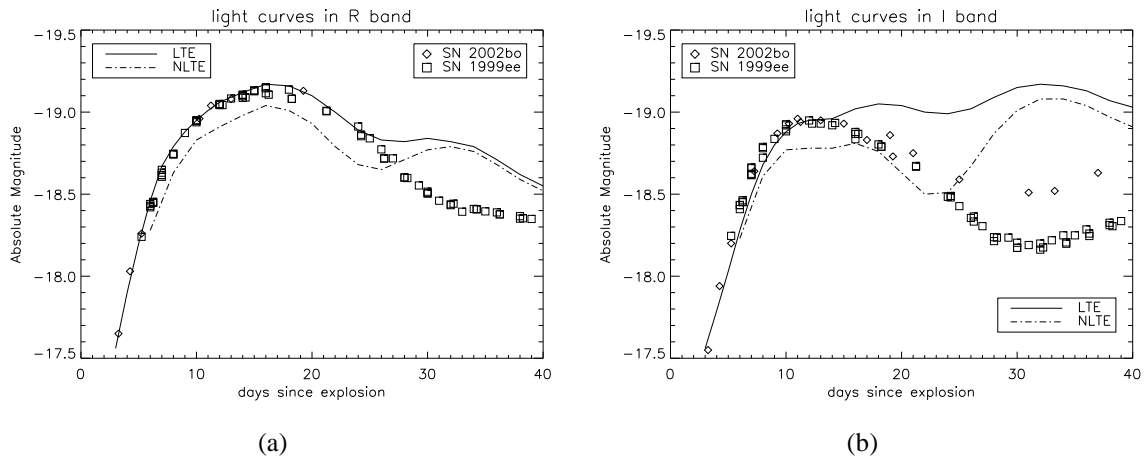


Figure 6.20: NLTE and LTE model light curves of the W7 model. The NLTE model atmosphere has an LTE temperature structure. (a) The R band light curves. (b) In the I band the NLTE light curve is an improvement.

curve shows almost no deviations from the LTE light curve. This also means that the assumption of NLTE does not improve the fit to the observed light curve. During the later phase the steep decline is also present in the NLTE model light curves. Therefore, the assumption of NLTE does not change the light curve in the U band, if the LTE temperature structure has been used. In figure 6.19(b), the NLTE model light curve in the B band is shown. The NLTE model light curve is slightly fainter than the LTE light curve. The shape of the NLTE light curve seems to be the same as for the LTE light curve. Hence, the NLTE model light curve is also an accurate fit to the observed light curves.

In figure 6.20(a) the NLTE model light curve of the R band is shown. The brightness of the NLTE light curve is fainter than the LTE light curve. It also has almost the same shape. For the phase after 25 days after the explosion, the NLTE model light curve rises again. Here, the assumption of NLTE does not improve the fit to the observed light curves of SN 1999ee and SN 2002bo. The infrared NLTE light curve of the I band is shown in figure 6.20(b). During the maximum phase, the NLTE light curve is fainter than the LTE light curve. A distinctive maximum is missing in the NLTE model light curve. For the phase between day 15 and day 25, the NLTE model light curve represents the observed SN Ia light curves very accurately. Here, a significant improvement compared to the LTE model light curve can be seen. However, after day 25 the NLTE model light curve starts to rise and becomes too bright. This is the same problem that already emerged in the LTE light curve.

The use of NLTE for the modeling of SN Ia light curves by the use of an LTE temperature structure changes the computed results. The NLTE model light curve in the I band has improved the fit to the observed light curves significantly. For the U and B band there are almost no differences compared to the LTE model light curves. In the V and R band, the NLTE model light curves are fainter than the LTE light curves. The presented NLTE light curves show only the effects that emerge if the LTE temperature structure is used for the calculation. It needs to be checked, what the differences in the model light curves occur, when the temperature structure of the SN Ia atmosphere can adapt to the NLTE conditions.

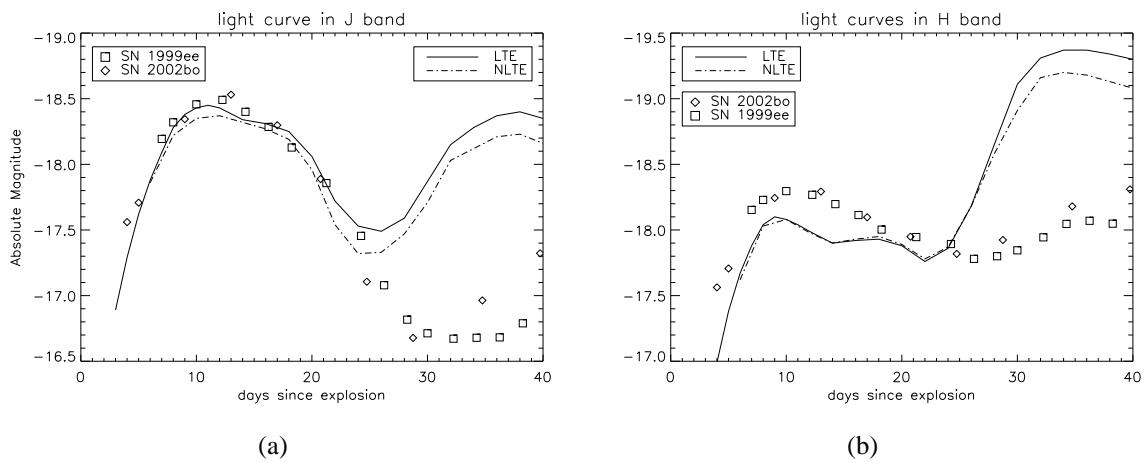


Figure 6.21: NLTE and LTE model light curves of the W7 model. The NLTE model atmosphere has an LTE temperature structure. (a) The J band light curves. (b) The H band light curves.

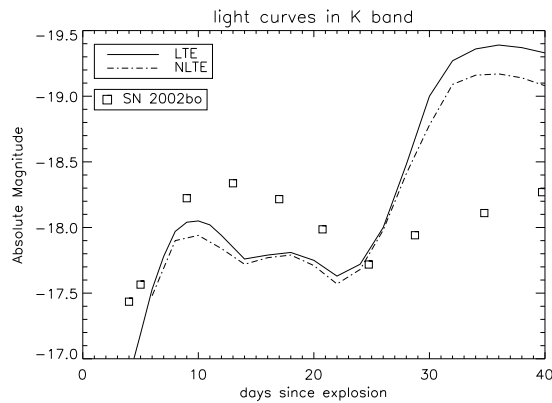


Figure 6.22: NLTE and LTE model light curves of the W7 explosion model in the K band. The NLTE model atmosphere has an LTE temperature structure.

### Near-infrared NLTE light curves

The NLTE model light curves of the near-infrared range have also been calculated. In figure 6.21(a), the light curves in the J band are shown. The NLTE light curve is fainter throughout the evolution compared to the LTE light curve. Therefore, the assumption of NLTE lead to no further improvement in the fit to the observed light curves. The H band NLTE model light curve is show in figure 6.21(b). Up to day 30 there are almost no differences between the LTE and the NLTE light curve. Later the NLTE light curve is a bit fainter than the LTE light curve. However, this is no significant improvement towards a better fit. Small differences of the NLTE model light curve and the LTE model light curves have been achieved as can be seen in figure 6.22. The NLTE model light curve also does not represent the observed light curve of SN 2002bo accurately. The second rise in the LTE light curve is also present in the NLTE light curve.

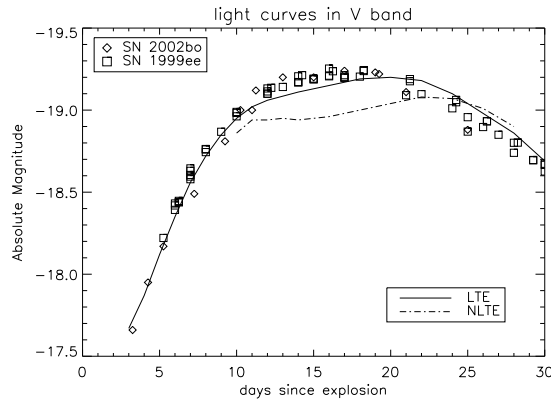


Figure 6.23: NLTE and LTE model light curves of the W7 explosion model in the V band.

### 6.4.2 NLTE atmosphere structures

Here, a more realistic NLTE calculation of the SN Ia model atmosphere evolution is performed. The temperature structure is now changing and adapts to the new conditions of NLTE. The calculation of an NLTE model light curve takes a huge amount of computation time. Considerably more wavelength points are needed for the calculation of the solution of the radiative transfer. And further, for all the species considered in NLTE, the rate equations have to be solved. Note that a time step in the NLTE calculation is not a real time step. The rate equation changes the energy of the atmosphere, but this is not included in the hydrodynamical solver. However, it is adequate as the goal is to obtain a temperature structure, where the atmosphere is in radiative equilibrium.

In a first try to calculate a more realistic NLTE light curve, numerous species up to calcium are considered to be in NLTE. These are the species H I, He I, He II, C I-III, O I-III, Ne I, Na I, Mg I-III, Si I-III, S I-III and Ca II. Higher species are neglected because they have more levels, which would increase the computation time significantly. Nevertheless, the computation of an NLTE light curve needs significantly more time than LTE. For this computation of NLTE model light curves, about 200,000 wavelength points need to be calculated, compared to about 2,400 wavelength points for a pure LTE light curve calculation. To obtain an NLTE model light curve in a reasonable time, the calculation has been started at day 10 after the explosion. The main focus is to check if the infrared light curves during the later phase can be further improved.

In figure 6.23, the NLTE and LTE light curves of the W7 deflagration model in the V band are shown. The maximum phase is not well represented by the NLTE model light curve. The LTE light curve fits the observed light curves better. At day 20 the NLTE and LTE light curves are almost the same. Compared to the NLTE light curve obtained with the LTE temperature structure, there are only small differences to the NLTE calculation where the temperature structure adapts to the NLTE conditions.

The NLTE and LTE model light curves shown in figure 6.24(a) are the ones for the U band. The peak brightness of the NLTE light curve is the same as for the LTE light curve. During the decline after the maximum, the NLTE light curve is brighter than the LTE light curve. At day 25 the decline seems to become too steep, like in the LTE model light curve.

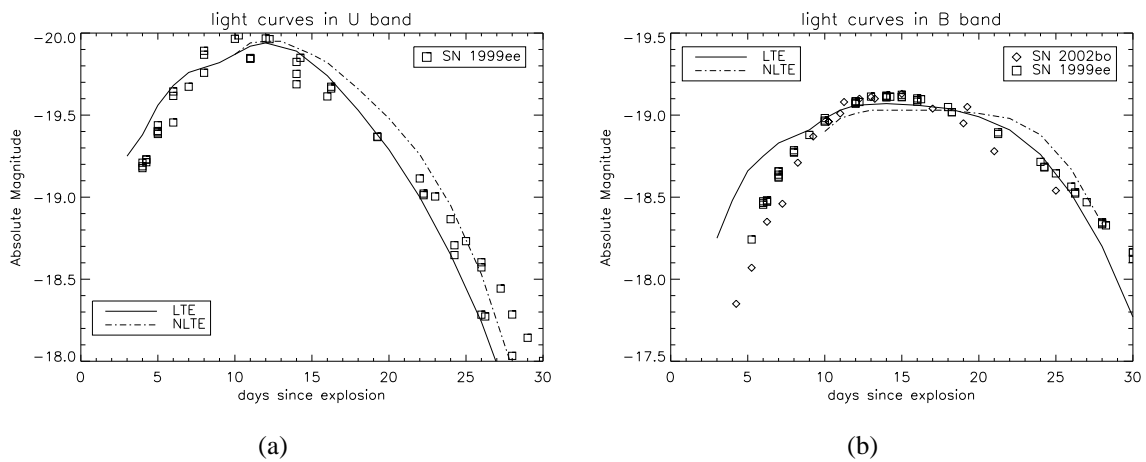


Figure 6.24: NLTE and LTE model light curves of the W7 model. (a) The U band light curves. (b) The B band light curves.

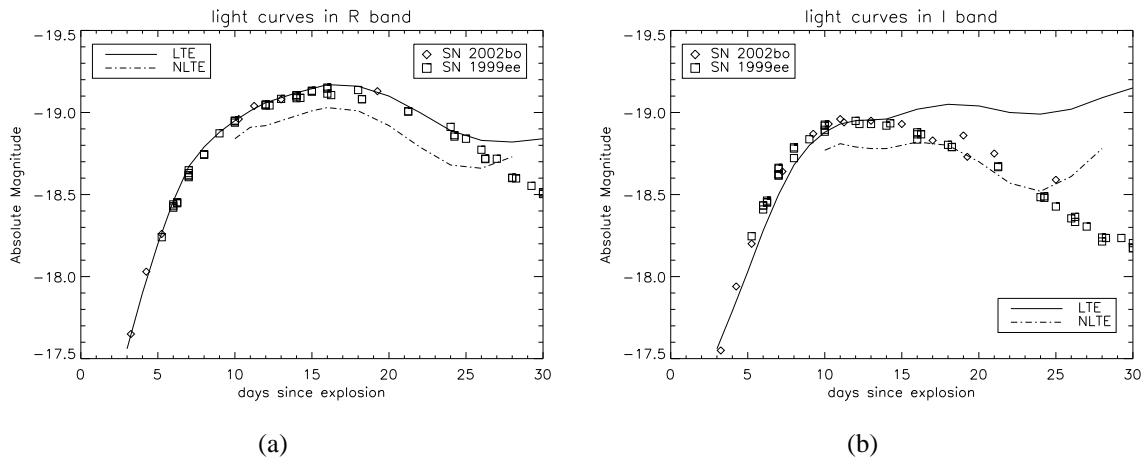


Figure 6.25: NLTE and LTE model light curve of the W7 model. (a) The R band light curves. (b) In the I band the NLTE light curve is an improvement.

Compared to the NLTE U band light curve with an LTE temperature structure, there are some deviations from the LTE light curve. In figure 6.24(b), the B band light curves for the W7 model in NLTE and LTE are shown. Here, the LTE and the NLTE model light curves have only small differences. The maximum phase is well represented by the NLTE light curve compared to the observed light curves. A few differences exist compared to the NLTE light curve with the LTE temperature structure.

The NLTE and LTE model light curves in the R band are shown in figure 6.25(a). The NLTE light curve has the same shape as the LTE light curve, but the NLTE light curve is fainter. At day 25 the NLTE starts to rise again. The effect that the NLTE light curve is fainter than the LTE light curve has also been observed with the NLTE light curve, which was calculated with the LTE temperature structure. In figure 6.25(b), the I band model light curves of NLTE and LTE are shown. During the maximum phase, the NLTE light curve is fainter than the LTE light curve. Between day 15 and day 25 the NLTE model light curve

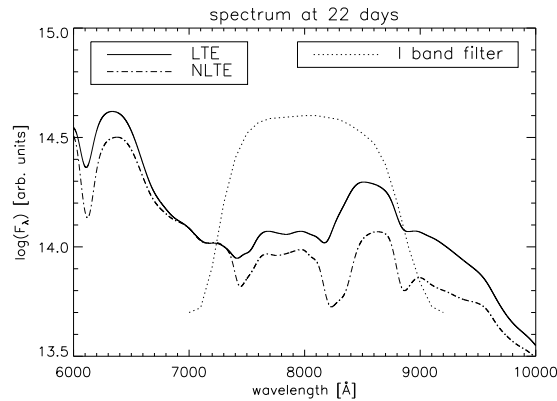


Figure 6.26: The LTE and NLTE spectra at day 22 after the explosion. The Ca II feature located at about 8500Å shows differences.

represents the observed light curves quite accurately. Here, the use of NLTE improves the fit to the observed light curves. This improvement has also been obtained with the NLTE model light curve calculated with the LTE temperature structure. It can also be seen, at day 25 the NLTE model light curve starts to rise again. Although the consideration of NLTE improves the model light curve in the I band, the problem with a rise in brightness after the maximum remains. The NLTE and LTE model spectra of day 22 after the explosion in the wavelength range of the Ca II feature in the I band is shown in figure 6.26. The differences of the Ca II feature located at 8500Å between both light curves are significant. Here, it can be seen why this leads to the better fit of the NLTE model light curve to the observed one in the I band.

The NLTE light curve with an NLTE temperature structure shows the same improvements as the NLTE light curves, where the LTE temperature structure has been used. It seems that reasonable results can be obtained for the NLTE model light curve calculation if the LTE temperature structure is used. Concerning the computation time, this might be an adequate approach.

The only improvement of the NLTE light curves has been reached in the I band. However, it still is very much improvable for the later phase beginning around day 25 after the explosion. The ionization of Fe is important for the infrared light curves and might be causing the second maximum in the I band light curve (Kasen 2006). Therefore, the species Fe I, Fe II and Fe III are important to treat them in NLTE. A computation of the evolution of the SN Ia atmosphere has been calculated with only this species considered in NLTE. The temperature structure also adapts to the NLTE conditions. As they have a large number of levels, the computation time increases dramatically. The overall computation time of the model light curve with the species Fe I-III considered in NLTE was about two months.

The NLTE model light curve in the optical V band is shown in figure 6.27(a). The Fe ions in NLTE do not change the model light curves significantly. There are only small deviations from the LTE light curve. The I band NLTE model light curve is shown in figure 6.27(b). Again, the Fe ions considered in NLTE have almost no influence on the model light curve. A small deviation from the LTE model light curve occurs around day 25. However, the consideration of Fe I-III in NLTE is not necessary, as it seems to have almost no influence on the model light curves during the phase, which has been calculated.

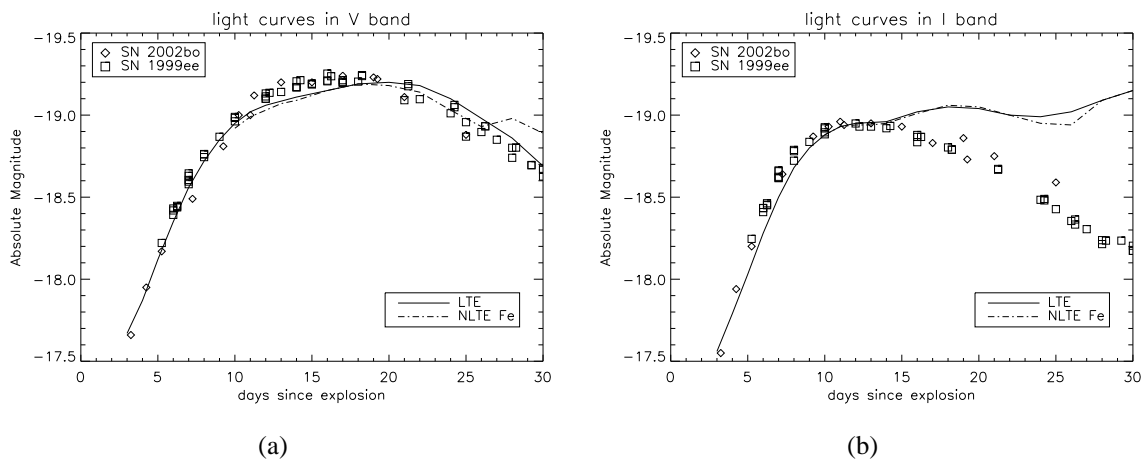


Figure 6.27: Light curves with Fe I-III in NLTE of the W7 explosion model. (a) The V band there arise no significant differences. (b) I the I band there.

## 6.5 Spectral evolution

The SN Ia model light curves have been simulated by the calculation of model spectra at different points in time of the evolution of the SN Ia atmosphere. Here, these spectra are presented. The spectral evolution of an SN Ia event is also of interest. As the SN Ia atmosphere evolves, the luminosity changes and different lines and features in the spectrum emerge and disappear. The spectral evolution of an SN Ia atmosphere in LTE and NLTE is presented in the following.

### 6.5.1 LTE spectral evolution

The calculated model spectra of the W7 deflagration model, where the atmosphere is considered in LTE are used. The spectra have been obtained with the temperature structure that has been obtained with the hydrodynamical solver.

The spectral evolution of the SN Ia atmosphere in LTE is shown in figure 6.28. In the ultraviolet wavelength range the flux drops dramatically throughout the whole evolution. In the blue wavelength range the spectrum of day 20 is brighter than at day 3, and the flux then drops again to day 50. In the optical wavelength range, the flux increases between day 3 and day 20. Going on towards day 50, the flux decreases. In the near-infrared, the flux increases between day 3 and day 20. For day 50 and day 20 the flux is almost the same. One can also see that different features are observed in the spectra of different days after the explosion.

### 6.5.2 NLTE spectral evolution

A look on the NLTE spectral evolution is now presented. The NLTE model spectra, where the LTE temperature structure has been used, are considered here. The NLTE spectral evolution is shown in figure 6.29. The overall changes are similar like in the LTE spectral evolution. In the ultraviolet the flux decreases significantly from day 10 to day 30. In the optical wavelength range, there are almost no differences in the luminosities between day 10

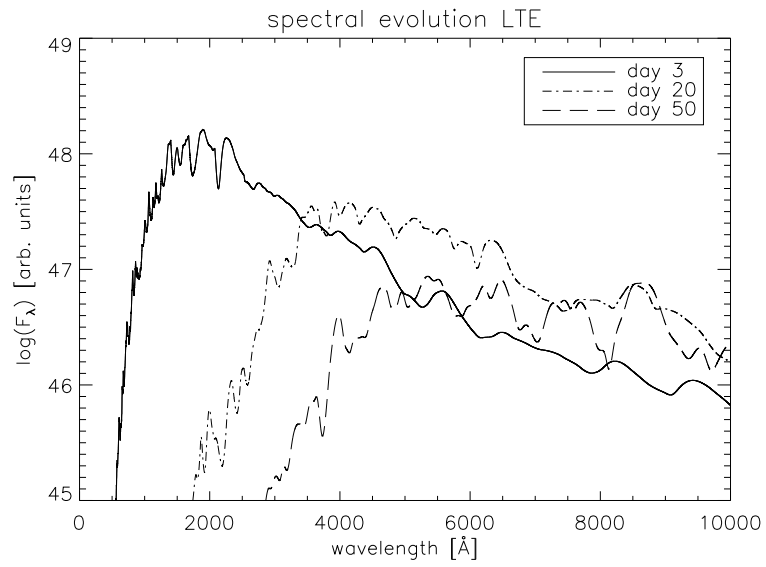


Figure 6.28: The LTE spectral evolution of a few days.

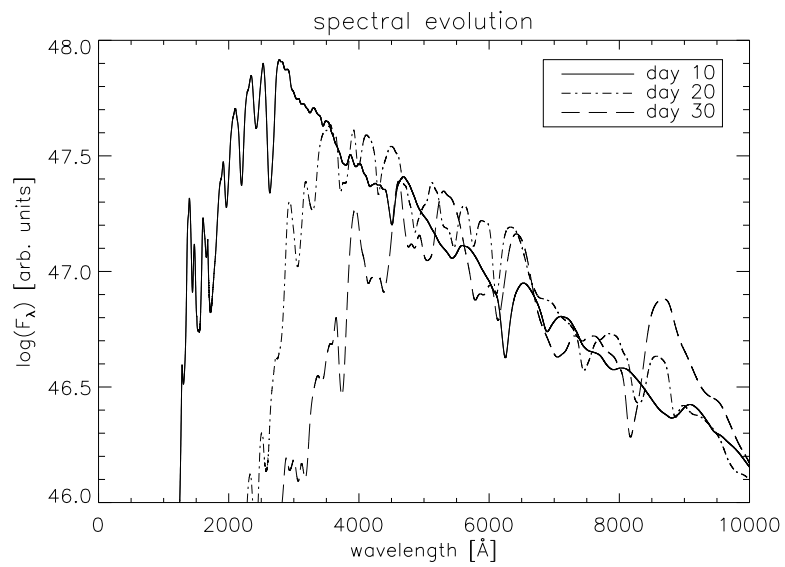


Figure 6.29: The NLTE spectral evolution of a few days.

and day 20. The flux decreases to day 30. In the infrared wavelength range, the flux stays almost the same for all three model spectra. One can also see that the feature seen in the model spectra change during the evolution of the atmosphere. The Ca II feature at 8500 Å is very strong at day 30. Here, the flux is larger than for day 10 or day 20.

The differences to the modeling of spectra that has been performed before with PHOENIX is that now the temperature structure has been obtained with the hydrodynamical solver instead of the temperature correction procedure. Therefore, the fits to observed SN Ia spectra can be improved by using the atmosphere structure obtained with the hydrodynamical solver, because a more accurate atmosphere structure for the correct time after the explosion can now be used. Model spectra of the early phase as well as late time spectra can be computed. The modeling of detailed NLTE spectra of SN Ia atmosphere with the use of the new hydrodynamical solver is a point of interest for future work.

## 6.6 Conclusions

The new hydrodynamical solver has been used to calculate model light curves of SN Ia events. First, model light curves have been obtained, where the atmosphere is considered to be in LTE. For the optical V band the fit to observed light curves are quite accurate. For the U, V and R band, the computed LTE model light curves are in reasonable agreement with the observations of SN 1999ee and SN 2002bo. In the infrared I band the model light curves after the maximum phase are too bright compared to the observed light curves. These differences also occur for the J, H and K band model light curves.

Different dynamical models have been used to calculate model light curves of SNe Ia. The W7 deflagration model and the delayed detonation model DD 25 have light curves that agree with the observed light curves for the optical bands. The W7 deflagration model seems to be the best fit to the observed light curves. In the infrared all model light curves are again too bright. The delayed detonation model DD16 can be ruled out as the correct explosion model, because all model light curves are too faint and do not show the shape of the observed light curves.

The assumption of an atmosphere which is not in LTE is necessary as scattering is important and has an influence on the model light curves. The NLTE light curves calculated with the LTE temperature structures showed differences from the LTE light curves. In the near-infrared I band, the assumption of NLTE reproduces a better fit of the model light curve to the observed light curves. In the near-infrared the differences to observed light curves are significant during the later phase. Further investigations with NLTE light curves have to be performed in the future.

At day 20 after the explosion, the temperatures even of the outer layers are higher than 4000 K. However, at day 40 the temperatures of the outer layers have dropped below 3000 K. Molecules can form under these conditions in the SN Ia atmosphere. This has an effect on the infrared spectra and light curves. Furthermore, the atmosphere becomes thinner and eventually transparent in the later phase. Hence, for future work, molecular lines need to be included in the model light curve calculations to check their influences on the SN Ia model light curves especially in the near-infrared.

# Chapter 7

## Conclusions and outlook

The first main topic of this work was the time dependent radiative transfer. The spherical symmetric special relativistic radiative transfer equation can now be solved including the time dependence. The implementation has been presented in detail in chapter 4. Two discretization schemes of the time dependence derivative have been applied to implement the time dependent SSRTE. Both discretization schemes have been successfully applied to calculate time dependent radiative transfer. Calculations with different time step sizes give the same results for the time dependent radiative transfer equation. Test calculations have been performed with the new time dependent radiative transfer. The atmosphere structure used for the tests is time independent. A comparison of the radiative time scale to a simple analytic radiative time scale shows a similar result. A perturbation that originates at the inner boundary of a model atmosphere is moving via the time dependent radiative transfer through the whole atmosphere. The model atmosphere with a brighter inner light bulb inside adapts to this condition, but it takes time until the additional radiation emerges at the surface. With a sinusoidally varying light bulb inside of the atmosphere, the luminosity of the whole atmosphere varies as a sinus eventually. It is now possible to compute the radiative transfer in model atmospheres including time dependence and all other relativistic effects.

A further time dependence implementation has been performed for the material in the model atmosphere. A new hydrodynamical solver has been implemented into the general purpose stellar atmosphere code PHOENIX. The hydrodynamical solver keeps track of the energy changes in the model atmosphere. It is especially designed to calculate the time evolution of an SN Ia model atmosphere during the free expansion phase. The SN Ia atmosphere is assumed to undergo a homologous expansion, and thus the energy change due to this adiabatic expansion is considered in the hydrodynamical solver. A procedure to obtain the energy deposition by  $\gamma$ -ray emissions due to the radioactive decay of  $^{56}\text{Ni}$  and  $^{56}\text{Co}$  is also implemented in the hydrodynamical solver. The hydrodynamical solver also updates the abundances of  $^{56}\text{Ni}$ ,  $^{56}\text{Co}$  and  $^{56}\text{Fe}$ . The material of the atmosphere interacts with the radiation field. This is also taken into account as an energy change of the atmosphere. An adaptive time step procedure determines the optimal time step size to reduce the overall computation time needed for a whole evolution calculation.

All parts of the hydrodynamical solver have been tested. The pure homologous expansion of the SN Ia atmosphere leads to a cooling of the atmosphere, and a decreasing luminosity is observed. A check of the entropy shows, that it does not change during a pure adiabatic expansion process. When the atmosphere is heated by the  $\gamma$ -ray emission of radioactive elements, the observed luminosity increases. Only the temperature of the parts of the atmo-

sphere where the energy is deposited is increasing. The transport of this energy is achieved by the radiative transfer. A temperature structure obtained with the energy transport part of the hydrodynamical solver is the same within an accuracy of 1% as one obtained with the PHOENIX temperature correction. If the temperature of the innermost layer has been changed, the rest of the atmosphere adapts to this new condition pushing the atmosphere back to radiative equilibrium. A first realistic test, where all contributions to the SN Ia atmosphere are considered in the hydrodynamical solver, shows that the temperature structure adapts to the new conditions and moves to a radiative equilibrium state.

The hydrodynamical solver has been applied to calculate SNe Ia model light curves. First calculations of model light curves where the atmosphere is considered to be in LTE have been presented. For that the W7 deflagration model has been used. The LTE model light curve of the V band represents the observed light curves of SN 1999ee and SN 2002bo quite accurately. In the U band, the decline in the model light curve is too steep. This is also the case for the B band model light curve. The R band model light curve is representing the observed light curves quite accurate for the first phase. However, during the later phase, the model light curve starts to rise again, and the brightness becomes too bright. In the infrared I band, the model light curve represents the rise and the maximum of the observed light curves. For the later phase after the maximum, the model light curve rises further, while in the light curves of SN 1999ee and SN 2002bo a decline is observed. These deviations in the near-infrared have been further investigated. It turned out that the too bright later phase of the near-infrared light curves can also be seen in the J, H and K band. The first phase up to day 25 is well represented in the model light curves. However, during the later phase the model light curves are too bright.

Different explosion models have been used to calculate SN Ia model light curves. A deflagration model W7 and two delayed detonation models DD 16 and DD 25 are the explosion models used in this work. One result is that model DD 16 can be ruled out as the correct explosion model. The luminosities in the DD 16 model light curves are too faint in all bands during the whole evolution of the SN Ia atmosphere. The best fit to the observed light curves has been obtained with the W7 deflagration model. The delayed detonation model DD 25 is also in good agreement with the observed light curves. The model light curves of DD 25 are brighter than the ones of the W7 deflagration model. The use of a different explosion model did not lead to an improvement of the model light curves in the near-infrared I band.

The amount of energy, which is put into the SN Ia atmosphere by the  $\gamma$ -ray emission due to radioactive decay has been changed in order to achieve a better fit to the observed light curves. A model light curve where the energy deposition is 20% higher than in the original amount has a higher brightness in the U, B, V and R band. With less energy put into the atmosphere, tested here with 80% of the original amount, the model light curves are fainter. In the infrared I band, the model light curves with different energy input do not change significantly. Therefore, with a change of the amount of energy input no better fit to the observed light curves has been achieved.

The influence of scattering for the solution of the radiative transfer used for the calculation of SN Ia model light curves has been investigated. A parameter that stands for the influence of line scattering in the solution of the radiative transfer equation has been changed. The result is that the consideration of scattering is important for the calculation of SN Ia model

---

light curves. A different scattering factor can improve the model light curves. For the near-infrared model light curves, no better fits have been achieved. The deviations during the later phase after maximum are present for all calculated factors.

A way where scattering is treated more correctly is the assumption of an NLTE atmosphere. At first, simple NLTE calculations have been performed. The NLTE model light curves have been calculated with using the LTE temperature structure. Here, significant improvements in the I band light curve have been achieved. A decline after the maximum is now present in the NLTE light curve. Later, the NLTE model light curve starts to rise again. NLTE model light curve calculations where the temperature structure adapts to the new conditions have also been performed. The result was that the resulting model light curves are quite similar to the ones with assuming an LTE temperature structure. SN Ia model light curves with the species Fe I-III in NLTE have been calculated. It seems that these species have no significant influences on the modeling of SN Ia light curves in the calculated time evolution phase.

The aim of this work was to show in principle that the new implementation of a hydrodynamical solver works and achieves reasonable results for the calculation of SN Ia model light curves. Now, more detailed studies of SN Ia model light curves can be performed. For instance, more different explosion models can be used to calculate the model light curves in order to determine the correct explosion mechanism for an SN Ia event. For this studies it is also interesting to take a look at the effects in the model light curves by using explosion models with a different mass of  $^{56}\text{Ni}$ , because the nickel mass has a direct influence of the maximum absolute magnitude. With variations of different parameters, it could be tried to reproduce an individual SN Ia light curve. Peculiar events of SN Ia can also be studied. It is also possible to search for indications of the physics that lie behind the Phillips relation.

For further improvements of the modeling of SN Ia light curves it is inevitable to perform more detailed NLTE calculations. The main obstacle is the huge amount of computation time that is needed for an NLTE model light curve calculation. It seems to be necessary to wait for faster computers, but it is also possible to run single long term calculations. However, one advantage seems to be that LTE temperature structure can be used to obtain reasonable NLTE model light curves. So detailed studies of the NLTE effects of different species at different points in time during the evolution can be performed.

The hydrodynamical solver can be also be improved as the implemented one is very simple. For instance, the assumption of homologous expansion is a reasonable but not correct assumption for SNe Ia atmospheres. Therefore, with a more realistic hydrodynamical solver it might be possible to obtain better resulting model light curves. As the emission of  $\gamma$ -rays is the main influence on the brightness, the energy deposition may have to be implemented with a more complex procedure. The assumption of gray radiative transfer for the  $\gamma$ -rays may not be accurate enough. The hydrodynamical solver can also be extended. Other energy changes or processes can be included to make it applicable to other kinds of atmospheres. For instance, the evolution of SNe II or variable stars can then be calculated.

A further topic of future work is also the modeling of SN Ia spectra with the hydrodynamical solver. Spectra can now be calculated for the correct evolution phase after the explosion. This will improve the fits to observed spectra especially for the early or later phase in the SN Ia atmosphere evolution. Further, with NLTE calculations it might be possible to obtain

much better fits.

A detailed study of the near-infrared model light curves and spectra is necessary to improve the model light curves in this wavelength range. In this work, the modeling of SN Ia light curves in the near-infrared for the later phase has not achieved reasonable fits to observed light curves. Other groups that calculated SN Ia model light curves with different approaches had also difficulties to obtain accurate fits for the near-infrared light curves (Pinto & Eastman 2000; Blinnikov & Sorokina 2004). A detailed study of the near-infrared model light curves has already been performed by Kasen (2006). One reason for these deviations from observed model light curves may be caused by incomplete atomic line data. Wrong infrared atomic lines in the data can also cause deviations in the model light curves. This has to be investigated. Furthermore, a study of the influences of abundance changes in the atmosphere to the model light curves and spectra can be performed to improve the near infrared model light curves. In the later phase of the light curve, the temperatures of the outer layers of the atmosphere become lower. For instance, at day 40 after the explosion, the temperatures are less than 3000 K. Molecules can form under these conditions, and molecular lines influence the spectra and light curves in the infrared. For future work, the molecular lines need to be included in the model light curve calculations and their effects on the model spectra need to be studied. As the envelope expands further, the atmosphere becomes thinner and eventually transparent. The atmosphere becomes also more transparent to the  $\gamma$ -rays. Therefore, non-thermal rates influence the matter in the atmosphere. This needs to be considered for the modeling of light time spectra and light curves.

Calculations of explosion models show that it is necessary to treat SN Ia as 3D objects. So a major step to calculate more accurate model spectra and light curves is to compute 3D radiative transfer. The PHOENIX 3D radiative transfer is in development and is nearly done. For the modeling of 3D SN Ia light curves, the hydrodynamical solver has to be implemented in 3D too. The time dependent radiative transfer can also be implemented into the 3D radiative transfer.

# Appendix A

## Alternative hydrodynamical solver

A first unsuccessful approach has been performed in order to implement an alternative hydrodynamical solver that has the purpose to calculate SN Ia model light curves. Here, this approach is presented in some detail. For a description with more details see Jack et al. (2009). The main idea is to keep track of the conservation of energy of the gas and radiation together. The change in the energy density of a radiating material is given by equation (96.15) in Mihalas & Mihalas (1984)

$$\frac{D}{Dt}E = -\frac{\partial}{\partial M_r}(L_r + P_r) + \varepsilon, \quad (\text{A.1})$$

where  $E$  is the total energy density. All quantities are considered in the comoving frame.  $P_r$  is not the pressure, but rather mechanical power on the sphere of a radius  $r$ . Equation A.1 is only valid to first order in  $v/c$ , and thus lacks the full special relativistic accuracy of PHOENIX. This is adequate for the velocities found in supernovae. The total energy density of a radiating fluid consists of the sum of the energy density of the material, the energy density of the radiation field, the kinetic energy density of the material, and the gravitational energy density:

$$E = E_{gas} + \frac{E_0}{\rho} + E_{kin} + E_{grav}. \quad (\text{A.2})$$

For supernovae in the free expansion phase, the gravitational energy density  $E_{grav}$  is negligible since the potential is small in absolute value with the standard choice of zero at infinity. Also, homologous expansion is a reasonably good assumption for supernovae. With the assumption of homology, the velocity of a given matter element is then constant as is the kinetic energy density. Thus, the kinetic energy term  $\frac{DE_{kin}}{Dt}$  can be neglected. So for the approach, only the energy densities of the radiation field and the material have to be considered. For the material, this includes effects such as an energy deposition due to radioactive decay of  $^{56}\text{Ni}$  and  $^{56}\text{Co}$  in an SN Ia envelope.

The other possible cause of a change in the energy density is the structure term. This term is given by (Cooperstein et al. 1986)

$$\frac{\partial}{\partial M_r}(P_r + L_r) = \frac{\partial}{\partial M_r} \{4\pi r^2 [u(p + P_0) + F_0]\}, \quad (\text{A.3})$$

where  $p$  is the pressure of the material and  $P_0$  the radiation pressure,  $u$  the velocity of the expanding gas, the radiative flux is represented by  $F_0$ , and the mass inside of the radius  $r$  of a

layer is given by  $M_r$ . The radiation pressure is a result of the solution of the detailed radiative transfer equation and given by

$$P_0 = \frac{4\pi}{c}K, \quad (\text{A.4})$$

with  $K$  the second moment of the radiation field.

The change of the energy density is given by the two quantities

$$L_r = 4\pi r^2 F_0 \quad (\text{A.5})$$

and

$$P_r = 4\pi r^2 u (p + P_0). \quad (\text{A.6})$$

If the atmosphere is in radiative equilibrium, the structure term is zero and the energy density stays constant if there is no additional energy source and the atmosphere is not expanding.

All the quantities required for the structure term can be derived from thermodynamics or the solution of the radiative transfer problem. The energy density of the material  $E_{gas}$  and the energy density of the radiation field  $\frac{E_0}{\rho}$  are needed. For the latter, the radiative transfer equation for the radiation field has to be solved to obtain the radiative energy. The radiative transfer code PHOENIX is used to solve the time-independent radiative transfer equation. The energy of the radiation field is given by

$$E_0 = \frac{4\pi}{c}J, \quad (\text{A.7})$$

where  $J$  is the mean intensity and  $c$  the speed of light.

The energy density of the material is given by

$$E_{gas} = \frac{3}{2} \frac{p}{\rho} = \frac{3}{2} \frac{R}{m_u} T, \quad (\text{A.8})$$

with the mean molecular weigh  $m_u$  and the universal gas constant  $R$ . The gas pressure is represented by  $p$  and the density by  $\rho$ .  $T$  stands for the temperature of the gas. The sum of the radiation and material energy density is then the total energy density

$$E_{total} = E_{gas} + \frac{E_0}{\rho}. \quad (\text{A.9})$$

The change in this total energy density is given by equation A.1. So the equation to calculate the new energy density  $E_{new}$  is given by

$$E_{new} = E_{old} - \frac{\partial}{\partial M_r} (L_r + P_r) \Delta t + \epsilon \Delta t. \quad (\text{A.10})$$

All the needed equations to calculate a simple light curve have been presented. One problem for the calculation is that only the change in the *total* energy density for the next time step can be determined. However, the total energy change is divided into a change in the gas energy density and the energy density of the radiation field. To obtain the correct

distribution of the gas and radiative energy, one has to iterate for each time step by solving the radiative transfer equation to compute the correct new temperature at the next time step.

To get the correct new temperature the following iteration scheme is applied. The error in the energy density,  $E_{err}$  is given by

$$E_{err} = \frac{E_{current} - E_{target}}{E_{target}}. \quad (\text{A.11})$$

Here,  $E_{target}$  is the desired new total energy density, which is known from equation A.10, and  $E_{current}$  is the total energy density obtained by equation A.9 with the current temperature guess and the radiative transfer solution. Tests have shown that the error is almost linearly proportional to the temperature  $T$ . Therefore, a new temperature guess can be calculated for the next iteration step. The new temperature guess  $T_{new}$  is obtained by

$$T_{new} = \frac{E_{err}T_{old} - E_{err_{old}}T_{cur}}{E_{err} - E_{err_{old}}}, \quad (\text{A.12})$$

where  $T_{cur}$  and  $E_{err}$  are the current temperature guess and energy error. The variables  $T_{old}$  and  $E_{err_{old}}$  are the temperature and energy error of the temperature iteration step before. With the new temperature guess we solve the radiative transfer equation again and check whether the total energy density is the desired one. It takes approximately four or five iteration steps to obtain the correct new temperature for a typical time step. The energy density is correct within an accuracy of  $10^{-5}$ .

## A.1 Test calculations

This alternative hydrodynamical solver has been tested with numerous test calculations. It has been tested with the use of gray time independent radiative transfer. For the test scenarios, the atmosphere is divided into 100 layers. Each part of the solver has been tested for its own.

As a first test, the time evolution code has been applied to a static atmosphere. The test atmosphere is not expanding and no energy sources are present. Inside the test atmosphere a ‘‘lightbulb’’ radiating with a constant luminosity to simulate the internal energy flow from a star is used. An approximate temperature structure for  $t = 0$ s has been assumed and then the atmosphere evolves towards radiative equilibrium. The atmosphere structure changed until it reaches steady state and the luminosity is constant in both space and time. The resulting final temperature structure is identical to the structure for radiative equilibrium computed directly with the PHOENIX temperature correction procedure.

The luminosity of three different static models is shown figure A.1(a). The atmosphere model on its way towards radiative equilibrium can be observed. All calculations were started from the same initial temperature structure. After a certain time, the radiative relaxation time scale, each atmosphere has the (constant) luminosity of the lightbulb throughout the configuration.

The next test is to look at time varying atmospheres. As an example an atmosphere with a sinusoidally varying lightbulb inside is considered. The luminosity in different layers is shown in figure A.1(b). The luminosity in each layer is sinusoidal. It takes some time for

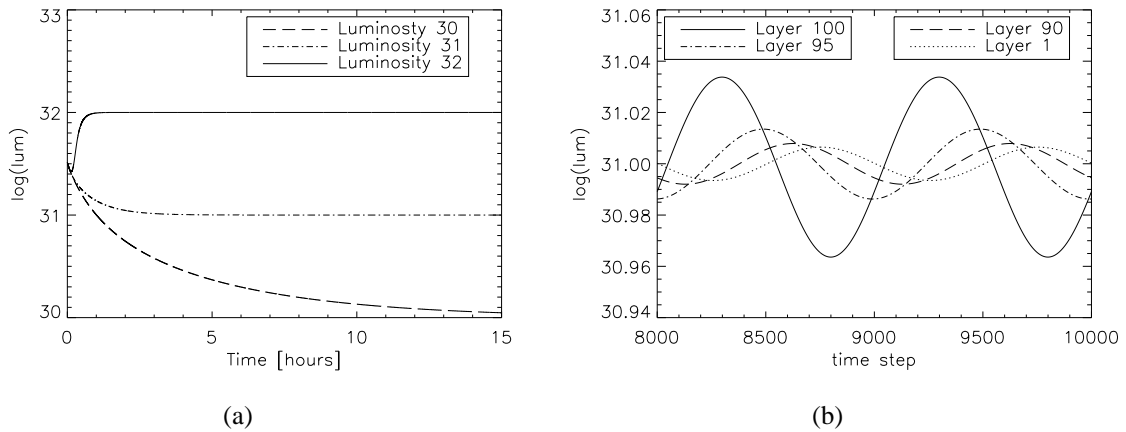


Figure A.1: Test calculations. (a) Three different light curves for the evolution to a stationary state. The three models have different luminosities produced by different inner “lightbulbs”. (b) The result for a sinusoidal varying lightbulb. Shown here is the luminosity in different layers. The phase shift between the lightbulb and the emergent flux is roughly  $\pi$ .

the radiation to reach the outside boundary of the atmosphere and this results in a phase shift compared to the lightbulb. The phase shift between the lightbulb and the emergent flux is roughly  $\pi$ .

For the next test, an atmosphere with an internal energy source is considered. The initial structure is the radiative equilibrium structure of the static model with the lightbulb with a luminosity of  $10^{31}$  erg/s. A constant energy deposition rate in each layer of the model atmosphere is then assumed. The luminosity is expected to increase over time and towards the outside. Figure A.2(a) shows a plot of the light curve of this test atmosphere. The luminosity increases in time because of the energy deposition.

Figure A.2(b) shows a plot of the light curve of supernova test atmosphere that is simply expanding. No energy deposition or energy transport is considered here. As can be seen, the observed luminosity is decreasing, because the atmosphere is cooling down adiabatically.

Now a setup more closely resembling a real supernova light curve is tested. Therefore, an initial atmosphere structure is taken and an energy source (radioactive decay) is added in each layer. The energy source exponentially decreases to simulate declining activity of the radioactive species. Figure A.3 shows the plot of the light curve of this test, resulting in a light curve with a supernova-like shape. A rising part of the light curve at the beginning because of the energy deposition is seen. After the maximum, the luminosity decreases due to the ongoing expansion and decreasing energy deposition. Of course this light curve is far from correct because the assumption of a gray atmosphere is a bad assumption for an SN Ia. But the tests show that the code behaves as expected.

This alternative approach to a hydrodynamical solver shows for all test cases the expected behavior. But it has not been further pursuit, as there emerged problems in the implementation and the use of the detailed radiative transfer. Further, numerous temperature iterations have to be performed in order to obtain the results for the next time step. As each iteration step includes a full solution of the radiative transfer, this turned out to cost too much computation time. Therefore, the approach presented in chapter 5 in this work is more efficient.

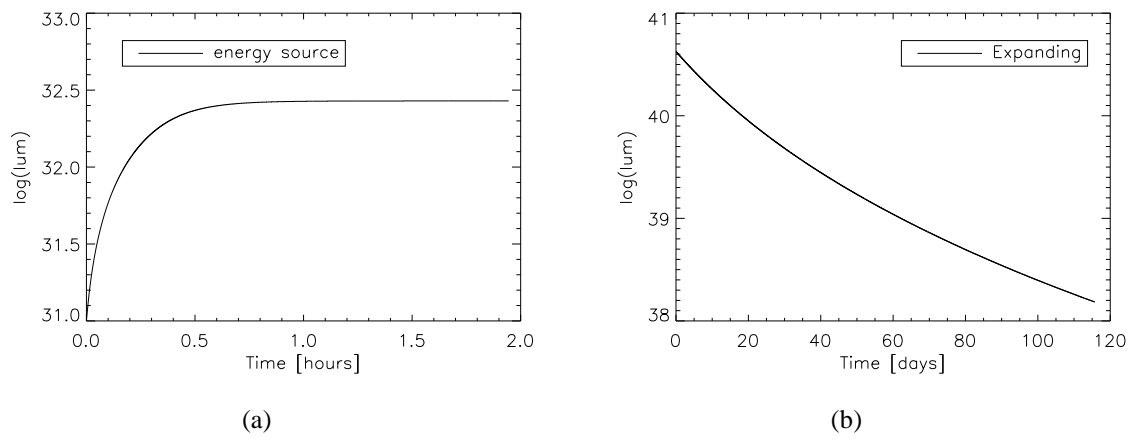


Figure A.2: Test calculations. (a) The light curve of a lightbulb with an additional energy source. An energy source in each layer causes an increasing luminosity of the model atmosphere. (b) Light curve of an atmosphere that is just expanding.

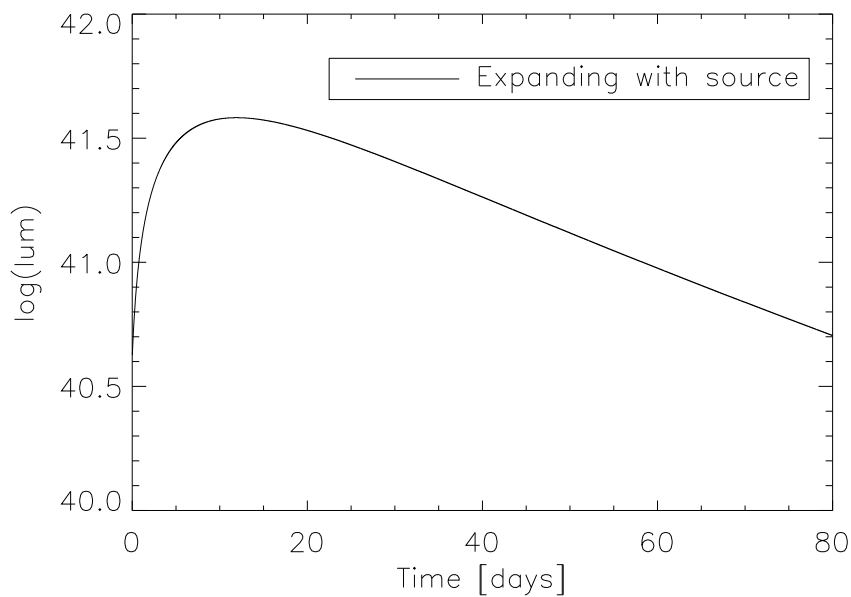


Figure A.3: Light curve of an atmosphere that is expanding and has an energy source. It has the typical shape of a light curve of a SN Ia. The luminosity rises due to the energy deposition. After the maximum we see the decline resulting from the expansion.



# Bibliography

- Allen, S. W., Rapetti, D. A., Schmidt, R. W., et al. 2008, MNRAS, 383, 879
- Allen, S. W., Schmidt, R. W., Ebeling, H., Fabian, A. C., & van Speybroeck, L. 2004, MNRAS, 353, 457
- APED. 2009, <http://cxc.harvard.edu/atomdb/>
- Arnett, W. D. 1969, Ap&SS, 5, 180
- Arnett, W. D. & Livne, E. 1994a, ApJ, 427, 315
- Arnett, W. D. & Livne, E. 1994b, ApJ, 427, 330
- Arnett, W. D., Truran, J. W., & Woosley, S. E. 1971, ApJ, 165, 87
- Barbon, R., Ciatti, F., & Rosino, L. 1979, A&A, 72, 287
- Barkat, Z. & Wheeler, J. C. 1990, ApJ, 355, 602
- Baron, E., Bongard, S., Branch, D., & Hauschildt, P. H. 2006, ApJ, 645, 480
- Baron, E. & Hauschildt, P. H. 1998, ApJ, 495, 370
- Baron, E., Lentz, E. J., & Hauschildt, P. H. 2003, ApJ, 588, L29
- Benetti, S., Meikle, P., Stehle, M., et al. 2004, MNRAS, 348, 261
- Blinnikov, S. & Sorokina, E. 2004, Ap&SS, 290, 13
- Blondin, S. 2009, P Cygni Profile, <http://www.eso.org/~sblondin/graphics/index.html>
- Bode, M. F. & Evans, A. 1989, Classical novae, ed. M. F. Bode & A. Evans
- Bongard, S., Baron, E., Smadja, G., Branch, D., & Hauschildt, P. H. 2006, ApJ, 647, 513
- Branch, D. 1998, ARA&A, 36, 17
- Branch, D., Fisher, A., & Nugent, P. 1993, AJ, 106, 2383
- Branch, D., Livio, M., Yungelson, L. R., Boffi, F. R., & Baron, E. 1995, PASP, 107, 1019
- Brau, J. 2009, Astronomy 122, <http://physics.uoregon.edu/~jimbrau/astr122/>
- Buchler, J.-R. & Mazurek, T. J. 1975, Memoires of the Societe Royale des Sciences de Liege, 8, 435

- Cannon, C. J. 1973, *ApJ*, 185, 621
- Colgate, S. A. & McKee, C. 1969, *ApJ*, 157, 623
- Cooperstein, J., van den Horn, L. J., & Baron, E. 1986, 309, 653
- Crotts, A., Garnavich, P., Priedhorsky, W., et al. 2005, *ArXiv Astrophysics e-prints*
- Dere, K. P., Landi, E., Mason, H. E., Monsignori Fossi, B. C., & Young, P. R. 1997, *A&AS*, 125, 149
- Dere, K. P., Landi, E., Young, P. R., & Del Zanna, G. 2001, *ApJS*, 134, 331
- Doggett, J. B. & Branch, D. 1985, *AJ*, 90, 2303
- Filippenko, A. V. 1997, *ARA&A*, 35, 309
- Filippenko, A. V., Richmond, M. W., Branch, D., et al. 1992, *AJ*, 104, 1543
- Ford, C. H., Herbst, W., Richmond, M. W., et al. 1993, *AJ*, 106, 1101
- Garcia-Senz, D. & Woosley, S. E. 1995, *ApJ*, 454, 895
- Goobar, A. & Perlmutter, S. 1995, *ApJ*, 450, 14
- Gutierrez, J., Garcia-Berro, E., Iben, I. J., et al. 1996, *ApJ*, 459, 701
- Hamuy, M., Phillips, M. M., Suntzeff, N. B., et al. 2003, *Nature*, 424, 651
- Hamuy, M., Phillips, M. M., Suntzeff, N. B., et al. 1996, *AJ*, 112, 2438
- Hamuy, M., Walker, A. R., Suntzeff, N. B., et al. 1992, *PASP*, 104, 533
- Hamuy, M. et al. 2002, *AJ*, 124, 417
- Han, Z. & Podsiadlowski, P. 2004, *MNRAS*, 350, 1301
- Han, Z. & Podsiadlowski, P. 2006, *MNRAS*
- Hauschildt, P. H. 1992, *Journal of Quantitative Spectroscopy and Radiative Transfer*, 47, 433
- Hauschildt, P. H., Barman, T. S., Baron, E., & Allard, F. 2003, in *ASP Conf. Ser. 288: Stellar Atmosphere Modeling*, ed. I. Hubeny, D. Mihalas, & K. Werner, 227–+
- Hauschildt, P. H. & Baron, E. 1999, *Journal of Computational and Applied Mathematics*, 109, 41
- Hauschildt, P. H. & Baron, E. 2004, *A&A*, 417, 317
- Hauschildt, P. H., Baron, E., & Allard, F. 1997, *ApJ*, 483, 390
- Hauschildt, P. H., Baron, E., Nugent, P., & Branch, D. 1996, in *ASP Conf. Ser. 96: Hydrogen Deficient Stars*, ed. C. S. Jeffery & U. Heber, 175–+

- Hauschildt, P. H., Lowenthal, D. K., & Baron, E. 2001, *ApJS*, 134, 323
- Hillebrandt, W. & Niemeyer, J. C. 2000, *ARA&A*, 38, 191
- Hoefflich, P. & Khokhlov, A. 1996, *ApJ*, 457, 500
- Höflich, P., Gerardy, C. L., Fesen, R. A., & Sakai, S. 2002, *ApJ*, 568, 791
- Höflich, P. & Stein, J. 2002, *ApJ*, 568, 779
- Hoyle, F. & Fowler, W. A. 1960, *ApJ*, 132, 565
- Iben, Jr., I. 1978, *ApJ*, 219, 213
- Iben, Jr., I. 1982, *ApJ*, 253, 248
- Iben, Jr., I. & Tutukov, A. V. 1984, *ApJS*, 54, 335
- Iwamoto, K., Brachwitz, F., Nomoto, K., et al. 1999, *ApJS*, 125, 439
- Jack, D., Hauschildt, P. H., & Baron, E. 2009, *A&A*, 502, 1043
- Jeffery, D. J. 1998, *ArXiv Astrophysics e-prints*
- Kasen, D. 2006, *ApJ*, 649, 939
- Kasen, D. 2009, *Supernova Spectra Page*, <http://panisse.lbl.gov/~dnkasen/tutorial/>
- Khokhlov, A., Mueller, E., & Hoefflich, P. 1993, *A&A*, 270, 223
- Khokhlov, A. M. 1991a, *A&A*, 245, 114
- Khokhlov, A. M. 1991b, *A&A*, 245, L25
- Khokhlov, A. M. 1995, *ApJ*, 449, 695
- Khokhlov, A. M., Oran, E. S., & Wheeler, J. C. 1997, *ApJ*, 478, 678
- Kraft, R. P. 1964, *ApJ*, 139, 457
- Krisciunas, K., Phillips, M. M., Suntzeff, N. B., et al. 2004a, *AJ*, 127, 1664
- Krisciunas, K., Suntzeff, N. B., Phillips, M. M., et al. 2004b, *AJ*, 128, 3034
- Kurucz, R. L. & Bell, B. 1995, *Atomic line list*, Kurucz CD-ROM No. 23
- Kurucz, R. L. & Bell, B. 2006, *Atomic line list*, <http://kurucz.harvard.edu/atoms.html>
- Leibundgut, B. 2001, *ARA&A*, 39, 67
- Lentz, E. J., Baron, E., Branch, D., & Hauschildt, P. H. 1999a, *Bulletin of the American Astronomical Society*, 31, 1424
- Lentz, E. J., Baron, E., Branch, D., & Hauschildt, P. H. 2001a, *ApJ*, 557, 266

- Lentz, E. J., Baron, E., Branch, D., & Hauschildt, P. H. 2001b, *ApJ*, 547, 402
- Lentz, E. J., Baron, E., Branch, D., Hauschildt, P. H., & Nugent, P. E. 1999b, *Bulletin of the American Astronomical Society*, 31, 976
- Lentz, E. J., Baron, E., Branch, D., Hauschildt, P. H., & Nugent, P. E. 2000, *ApJ*, 530, 966
- Lentz, E. J., Baron, E., Hauschildt, P. H., & Branch, D. 2002, *ApJ*, 580, 374
- Lira, P., Suntzeff, N. B., Phillips, M. M., et al. 1998, *AJ*, 115, 234
- Livio, M. 2000, in *Type Ia Supernovae, Theory and Cosmology*. Edited by J. C. Niemeyer and J. W. Truran. Published by Cambridge University Press, 2000., p.33, ed. J. C. Niemeyer & J. W. Truran, 33–+
- Livio, M. & Riess, A. G. 2003, *ApJ*, 594, L93
- Livio, M. & Truran, J. W. 1992, *ApJ*, 389, 695
- Meakin, C. A., Seitenzahl, I., Townsley, D., et al. 2009, *ApJ*, 693, 1188
- Meikle, W. P. S. 2000, *MNRAS*, 314, 782
- Meikle, W. P. S., Cumming, R. J., Geballe, T. R., et al. 1996, *MNRAS*, 281, 263
- Mihalas, D. 1970, *Stellar Atmospheres* (W. H. Freeman and Company)
- Mihalas, D. 1978, *Stellar Atmospheres*, 2nd Edition (W. H. Freeman and Company)
- Mihalas, D. 1980, *ApJ*, 237, 574
- Mihalas, D. & Mihalas, B. 1984, *Foundations of Radiation Hydrodynamics* (Oxford University)
- Minkowski, R. 1941, *PASP*, 53, 224
- Mochkovitch, R. 1996, *A&A*, 311, 152
- Niemeyer, J. C. & Hillebrandt, W. 1995, *ApJ*, 452, 769
- Niemeyer, J. C. & Kerstein, A. R. 1997, *New Astronomy*, 2, 239
- Niemeyer, J. C. & Woosley, S. E. 1997, *ApJ*, 475, 740
- Nomoto, K. & Sugimoto, D. 1977, *PASJ*, 29, 765
- Nomoto, K., Sugimoto, D., & Neo, S. 1976, *Ap&SS*, 39, L37
- Nomoto, K., Thielemann, F.-K., & Yokoi, K. 1984, *ApJ*, 286, 644
- Nugent, P., Baron, E., Branch, D., Fisher, A., & Hauschildt, P. H. 1997, *ApJ*, 485, 812
- Nugent, P., Baron, E., Hauschildt, P. H., & Branch, D. 1995, *ApJ*, 441, L33

- Nugent, P., Kim, A., & Perlmutter, S. 2002, *PASP*, 114, 803
- Paczynski, B. 1973, *A&A*, 26, 291
- Patat, F., Barbon, R., Cappellaro, E., & Turatto, M. 1994, *A&A*, 282, 731
- Percival, W. J., Cole, S., Eisenstein, D. J., et al. 2007, *MNRAS*, 381, 1053
- Perlmutter, S., Aldering, G., Goldhaber, G., et al. 1999, *ApJ*, 517, 565
- Perlmutter, S., Gabi, S., Goldhaber, G., et al. 1997, *ApJ*, 483, 565
- Perlmutter, S., Pennypacker, C. R., Goldhaber, G., et al. 1995, *ApJ*, 440, L41
- Phillips, M. M. 1993, *ApJ*, 413, L105
- Pignata, G., Benetti, S., Mazzali, P. A., et al. 2008, *MNRAS*, 388, 971
- Pinto, P. A. & Eastman, R. G. 2000, *ApJ*, 530, 744
- Plewa, T. 2007, *ApJ*, 657, 942
- Plewa, T., Calder, A. C., & Lamb, D. Q. 2004, *ApJ*, 612, L37
- Pskovskii, I. P. 1977, *Soviet Astronomy*, 21, 675
- Reinecke, M., Hillebrandt, W., & Niemeyer, J. C. 1999, *A&A*, 347, 739
- Richardson, D., Thomas, R., Casebeer, D., Branch, D., & Baron, E. 2002, in *Bulletin of the American Astronomical Society*, Vol. 34, *Bulletin of the American Astronomical Society*, 1205–+
- Richardson, D., Thomas, R. C., Casebeer, D., et al. 2001, in *Bulletin of the American Astronomical Society*, Vol. 33, *Bulletin of the American Astronomical Society*, 1428–+
- Riess, A. G., Filippenko, A. V., Challis, P., et al. 1998, *AJ*, 116, 1009
- Röpke, F. K., Hillebrandt, W., Niemeyer, J. C., & Woosley, S. E. 2006, *A&A*, 448, 1
- Rutten, R. 2003, *Radiative Transfer in Stellar Atmospheres*, 8th edition edn. (Utrecht University lecture notes)
- Saffer, R. A., Livio, M., & Yungelson, L. R. 1998, *ApJ*, 502, 394
- Schmidt, B. P., Suntzeff, N. B., Phillips, M. M., et al. 1998, *ApJ*, 507, 46
- Segretain, L., Chabrier, G., & Mochkovitch, R. 1997, *ApJ*, 481, 355
- Shara, M. M. 1989, *PASP*, 101, 5
- Spergel, D. N., Bean, R., Doré, O., et al. 2007, *ApJS*, 170, 377
- Spergel, D. N., Verde, L., Peiris, H. V., et al. 2003, *ApJS*, 148, 175

- Stritzinger, M. et al. 2002, *AJ*, 124, 2100
- The Planck Collaboration. 2006, *ArXiv Astrophysics e-prints*
- Townsley, D. M., Calder, A. C., Asida, S. M., et al. 2007, *ApJ*, 668, 1118
- Truran, J. W., Arnett, W. D., & Cameron, A. G. W. 1967, *Canadian Journal of Physics*, 45, 2315
- Turatto, M., Benetti, S., Cappellaro, E., et al. 1996, *MNRAS*, 283, 1
- Turatto, M., Piemonte, A., Benetti, S., et al. 1998, *AJ*, 116, 2431
- Wilson, O. C. 1939, *ApJ*, 90, 634
- Woosley, S. E., Kasen, D., Blinnikov, S., & Sorokina, E. 2007, *ApJ*, 662, 487
- Woosley, S. E., Taam, R. E., & Weaver, T. A. 1986, *ApJ*, 301, 601
- Woosley, S. E. & Weaver, T. A. 1994, *ApJ*, 423, 371
- Woosley, S. E., Wunsch, S., & Kuhlen, M. 2004, *ApJ*, 607, 921
- Wunsch, S. & Woosley, S. E. 2004, *ApJ*, 616, 1102
- Zwicky, F. 1938, *PASP*, 50, 215
- Zwicky, F. 1940, *Reviews of Modern Physics*, 12, 66

# Danksagung

Ich bedanke mich in erster Linie bei meinen Eltern, die mich stets unterstützt haben und mir so ein sorgenfreies Studium ermöglicht haben.

Bei Peter Hauschildt bedanke ich mich für die Vergabe des spannenden Themas meiner Arbeit und die stets sehr gute Betreuung.

Weiterer Dank gilt Eddie Baron, der mir immer Tipps und Hilfestellungen zu meinen Problemen gegeben hat. Insbesondere bedanke ich mich auch für die gute Betreuung bei meinem Besuch in Oklahoma.

Bei allen Mitglieder der PHOENIX-Arbeitsgruppe und natürlich allen Mitarbeitern der Sternwarte bedanke ich mich für die gute Atmosphäre, sowohl wenn ich Hilfe brauchte als auch beim Plausch zwischendurch.

Bedanken möchte ich mich insbesondere auch bei Knop und Andy dafür, dass sie meine Arbeit Korrektur gelesen haben und mir mit ihren Anmerkungen und Kritik weitergeholfen haben.

Bei den Bewohnern des Beamtenwohnhauses bedanke ich mich dafür, dass sie mich immer noch mein mittägliches Brot bei Ihnen verspeisen lassen.

Zu guter Letzt bedanke ich mich bei allen, die wissentlich und unwissentlich zu meiner Arbeit beigetragen haben und die ich vergessen habe hier zu erwähnen.